BRNO UNIVERSITY OF TECHNOLOGY
VYSOKÉ UČENÍ TECHNICKÉ V BRNĚ

FACULTY OF ELECTRICAL ENGINEERING AND COMMUNICATION
DEPARTMENT OF RADIO ELECTRONICS

FAKULTA ELEKTROTECHNIKY A KOMUNIKAČNÍCH TECHNOLOGIÍ
ÚSTAV RADIOELEKTRONIKY

MILLIMETER WAVE BAND WIRELESS CHANNEL MEASUREMENT TECHNIQUES IN AUTOMOTIVE APPLICATIONS

DOCTORAL THESIS
DIZERTAČNÍ PRÁCE

AUTHOR
AUTOR PRÁCE

Ing. JOSEF VYCHODIL

Brno 2021

BRNO UNIVERSITY OF TECHNOLOGY
VYSOKÉ UČENÍ TECHNICKÉ V BRNĚ

FACULTY OF ELECTRICAL ENGINEERING AND COMMUNICATION
FAKULTA ELEKTROTECHNIKY A KOMUNIKAČNÍCH TECHNOLOGIÍ

DEPARTMENT OF RADIO ELECTRONICS
ÚSTAV RADIOELEKTRONIKY

MILLIMETER WAVE BAND WIRELESS CHANNEL MEASUREMENT TECHNIQUES IN AUTOMOTIVE APPLICATIONS
METODY MĚŘENÍ PŘENOSOVÝCH KANÁLŮ V PÁSMU MILIMETROVÝCH VLN V OBLASTI AUTOMOBILOVÝCH APLIKACÍ

DOCTORAL THESIS
DIZERTAČNÍ PRÁCE

AUTHOR — Ing. Josef Vychodil
AUTOR PRÁCE

ADVISOR — Dr. Techn. Vojtěch Derbek
VEDOUCÍ PRÁCE

BRNO 2021

ABSTRACT

This doctoral thesis deals with the millimeter wave band wireless channel measurement techniques in automotive applications. After a brief introduction into the topic and the summary of the current channel measurement techniques, the goals — the development and assembly of a measurement system, capable of capturing all of the millimeter wave band channel features and practical measurements with this system, are set. The next part is the core of the dissertation — the developed channel sounder is presented and a detailed description of used methods, principles, hardware and data processing is given. A significant part of the thesis is dedicated to the mitigation of the unwanted effects caused by the non-linear components in the measurement chain. The last chapters show the results of practical measurements of various scenarios — the intra-car channels, vehicle to vehicle channels as well as vehicle to infrastructure channels.

KEYWORDS

millimeter wave band, channel impulse response, channel sounding, m-sequences, Golay sequences, non-linearities

ABSTRAKT

Tato disertační práce se zabývá metodami měření přenosových kanálů v pásmu milimetrových vln se zaměřením na automobilové aplikace. Po stručném úvodu do problematiky a shrnutí současných metod měření přenosových kanálů jsou vytyčeny cíle práce — návrh a sestavení měřícího systému, schopného zachytit všechny rysy a detaily rychle se měnícího únikového přenosového kanálu a praktická měření s tímto systémem. Následuje jádro disertace — představení vyvinutého systému a detailní popis použitých metod, principů, hardwaru i způsob zpracování naměřených dat. Podstatná část práce je věnována eliminaci nechtěných jevů, způsobených nelineárními prvky v systému. Poslední kapitoly obsahují výsledky praktických měření různorodých scénářů — kanály pro komunikaci uvnitř vozidla, mezi vozidly i mezi vozidly a infrastrukturou.

KLÍČOVÁ SLOVA

milimetrové vlny, impulsní odezva kanálu, měření impulsní odezvy kanálu, m-sekvence, Golay sekvence, nelinearity

VYCHODIL, Josef *Millimeter wave band wireless channel measurement techniques in automotive applications*: doctoral thesis. Brno: Brno University of Technology, Faculty of Electrical Engineering and Communication, Department of Radio Electronics, 2021. 98 p. Supervised by Dr. Techn. Vojtěch Derbek

DECLARATION

I declare that I have written my doctoral thesis on the theme of "Millimeter wave band wireless channel measurement techniques in automotive applications" independently, under the guidance of the doctoral thesis supervisor and using the technical literature and other sources of information which are all quoted in the thesis and detailed in the list of literature at the end of the thesis.

As the author of the doctoral thesis I furthermore declare that, as regards the creation of this doctoral thesis, I have not infringed any copyright. In particular, I have not unlawfully encroached on anyone's personal and/or ownership rights and I am fully aware of the consequences in the case of breaking Regulation § 11 and the following of the Copyright Act No 121/2000 Sb., and of the rights related to intellectual property right and changes in some Acts (Intellectual Property Act) and formulated in later regulations, inclusive of the possible consequences resulting from the provisions of Criminal Act No 40/2009 Sb., Section 2, Head VI, Part 4.

Brno ....

(author's signature)

ACKNOWLEDGEMENT

I would like to thank my supervisor Dr. Techn. Vojtěch Derbek for his support and encouragement during my study and work. I would also like to thank prof. Ing. Aleš Prokeš., Ph.D. and doc. Ing. Jiří Blumenstein Ph.D., who were great to cooperate with within several projects.

Brno ....

(author's signature)

CONTENTS

LIST OF FIGURES

LIST OF TABLES

INTRODUCTION

The growing demand for fast, reliable and low latency wireless communication lead to enormous improvements in the modulation, encoding and other physical layer techniques in the last few decades. However, even using those techniques, it is impossible to fulfil the extreme requirements — for example data rates in the order of tens of gigabits per second and latency less than one millisecond — for the next generation wireless systems within the limited bandwidth of the conventional sub-6 GHz band.

There are several frequency bands, with huge available bandwidth, which can be utilized for those next generation systems. One of the most promising is the Millimeter Wave Band (MMW), namely 30–300 GHz, which is relatively unused nowadays and ready for future systems deployment.

Besides "classical", for example fixed (WiFi) or mobile (Long Term Evolution (LTE)) communication systems, there is a whole new emerging field, which will take an advantage of those new systems — the self-driving car industry. To ensure the safety and reliability of this transportation, a robust communication between the nodes (either the vehicles or some infrastructure structures) is needed. Additionally, to provide comfort and entertainment to the crew during the journey, a broadband connectivity inside the vehicle is of high advantage.

In order to make development of those systems possible, one of the most important topics to understand is the knowledge of the environment's electromagnetic wave propagation characteristics. This thesis addresses the problem of obtaining these parameters.

The work is organized as follows. Chapter 1 briefly introduces the channel measurement techniques and Chapter 2 sets the goals. Chapter 3 is the core of the thesis — it describes thoroughly the developed measurement system, including the hardware, methods and data processing, and also its features and parameters. Chapters 4, 5 and 6 show the first experiments with the developed channel sounding system — measurement of the intra-car channel. Chapter 7 explains several improvements, such as separating the transmit and receive part of the system, thus enabling more flexible measurements. It also gives a basic example of Vehicle to Vehicle (V2V) channel measurements. Chapters 8 and 9 show measurements of V2V and Vehicle to Infrastructure (V2I) channels, respectively. Chapter 10 summarizes the thesis and its results.

1 STATE OF THE ART

1.1 Channel measurement methods

Knowledge of the propagation channel characteristics, such as the path loss, delay and Doppler spreads or the coherence bandwidth, are of crucial importance for all modern localization, radar or communication systems. Utilizing several GHz of bandwidth, this is even more pronounced with the Ultra Wide Band (UWB) or MMW systems. When these parameters become precise, more advanced data processing methods and modulation techniques can be used to transfer data, which leads to higher data rates and lower Bit Error Ratios (BERs) as well as better localization accuracy. The enormous instantaneous bandwidths of several GHz in the MMW applications promise high data throughput and precise spatial localization.

The parameters of the radio channel may be obtained through a process called channel sounding. There are several techniques and methods that can be utilized to perform those measurements. Basically, the channel sounding methods can be divided into those working in the time domain and those operating in the frequency domain.

1.1.1 Channel sounding in the time domain

The most obvious and straightforward method of performing a channel measurement in the time domain is to transmit an ideal (e.g. Dirac) pulses and receive the response by a sampling device, for example the oscilloscope. This is of course unfeasible to be done in reality — there is a number of practical limitations. However, one can transmit band limited pulses which approach the ideal Dirac pulse in several properties.

In [1, 2], our team has presented a time domain channel sounding by transmitting Gaussian pulses (or its derivatives) and then recovering the Channel Impulse Response (CIR) by deconvolving the received signal utilizing the CLEAN algorithm. However this approach is challenging for the power amplifiers and provides low Signal to Noise Ratio (SNR).

Utilizing pulse sequences rather than single pulse provides substantial improvement in various system parameters — it for example relaxes the requirements for the power amplifier by reducing the Peak to Average Power Ratio (PAPR) and also improves the SNR by exploiting the correlation gain. For example, authors of [3, 4, 5, 6] presented numerous practical channel measurements by transmitting and receiving wideband pulse sequences.

Several papers deal with the design of the time domain channel sounder for the 60 GHz band; usually utilizing custom hardware design or even custom silicon chips, whose development is very time consuming. For example, authors of [7] propose a sounding system with a bandwidth of 100 MHz without the need of a cabled connection between the transmitter and receiver, thus enabling flexible measurements. Purely hardware designs of channel sounders often use the so-called sliding correlator technique for data processing, as was shown, for example in [8]. Other papers, e.g. [9] or [10], describe various multiple input multiple output (MIMO) time domain channel sounding systems with a bandwidth of several GHz and a reasonable dynamic range of 30–50 dB.

To summarize, channel sounders operating in the time domain usually provide fast measurements speeds (e.g. several tens of thousands measurements per seconds), flexibility (separated transmit and receive parts of the system), but on the other hand suffer from poor dynamic range.

1.1.2 Channel sounding in the frequency domain

Measurements in the frequency domain are conventionally carried out using a Vector Network Analyzers (VNAs), which perform stepped frequency sweeping as it was shown, for example, in [11, 12, 13, 14, 15]. It is easily conducted by utilizing off-the-shelf laboratory instruments and offers excellent dynamic range usually greater than 60 dB. On the other hand — a complete sweep over the frequency range of interest using VNA usually takes several tens of seconds, depending on the number of frequency steps and requested dynamic range. During this time, the channel must remain static. For this reason, the VNA method cannot be used to measure either slowly changing channels (caused e.g. by people or vehicle movement) or for measuring fast changing channels (caused e.g. by vibrations). Another great disadvantage of this technique is the fact that the transmitter and receiver is physically one device, which limits the use to static indoor, small range outdoor or intra car channels, but forbid deployment in the V2V or V2I environments.

Another approach, which could be considered as a frequency domain method, is utilizing a multi-tone waveform as an excitation signal. For example, in [16], authors presented a flexible channel sounding system of this type. An Arbitrary Waveform Generator (AWG) is used as a transmitter, which offers several advantages such as flat frequency spectrum, controllable crest factor or high SNR through processing gain. However, even with a modern AWG, the system bandwidth is in this case limited to 500 MHz.

1.2 Interpreting the channel measurements results

Depending on which of the methods mentioned in previous paragraphs was used, some sort of post processing of the obtained data is needed to obtain useful results.

When the direct time domain RF pulse approach is used, then the recorded data is instantly an approximation of the CIR, which happens to be a standard convenient way of how to deterministically represent a single channel realization characteristics. It shows the channel output when the input is a Dirac impulse. The general way to model a CIR of a time invariant multipath wireless channel is to express it as a sum of attenuated, delayed and phase shifted replicas of the Dirac delta function:

$$h(t) = \sum_{n=0}^{L-1} \rho_n e^{j\Phi_n} \delta(t - \tau_n), \tag{1.1}$$

where L is the number of multipath components, δ is the Dirac delta function and τ_n, ρ_n and Φ_n is the path delay, gain and phase shift of n-th component, respectively.

Measurements in the time domain using pulse sequences usually requires post processing by means of correlating the received signal with the transmitted replica, e.g. matched filtering in order to obtain the CIR estimation.

The measurements in the frequency domain using VNA provides the Channel Transfer Function (CTF) $H(f)$ in terms of the s parameter, which represents the channel gain and phase shift as a function of frequency. We can exchange without any loss of information between the $H(f)$ and the $h(t)$ representation utilizing Fast Fourier Transform (FFT) or more precisely Inverse Fast Fourier Transform (IFFT):

$$\begin{aligned} H(f) &= \int_{-\infty}^{\infty} h(t) e^{-j2\pi ft} dt \\ &= \sum_{n=0}^{L-1} \rho_n e^{j\Phi_n} e^{-j2\pi f\tau_n}. \end{aligned} \tag{1.2}$$

The post processing of the measured VNA data usually consists of two steps — multiplying $H(f)$ by a windowing function (e.g. Hann) to mitigate the leakage effects and then applying the IFFT to get the CIR $h(t)$.

The CIR is of interest for several reasons. First of all, it contains all the information needed to extract any of the channel parameters, for example the path loss, propagation delay, power delay profile, delay spread or coherence bandwidth. When the evolution of the CIR in time is captured, it contains an additional information about the channel such as Doppler spread or if slow fading or shadowing occurs. One can also determine e.g. the transmitter and receiver relative velocities as well as distances and velocities of any objects involved in the particular channel layout. When various channel realisations (with their evolution in time) are captured in different places and scenarios, a statistical model can be created based upon that data.

That model then can be used to generate arbitrary large number of different CIRs (corresponding to the given environment) to help the development and evaluation of the device or system under development.

1.3 Other MMW time domain channel sounding systems

After carefully considering all of the above mentioned channel sounding system designs, evaluating their pros and cons and taking into account all of the requirements (which are specified and explained in Chapter 2), a time domain system based on pulse sequences was chosen as a system design for this thesis.

Table 1.1 [17] lists other similar time domain channel sounding systems working in the MMW and their basic parameters.

Reference	Institution	Sounder type	Measurement parameters
[18]	NYU-1	Sliding correlation	1 GHz bandwidth up to 30500 snapshots/s
[19]	UT Austin	Sliding correlation	1.5 GHz bandwidth stationary measurements
[20]	Virgina Tech	Sliding correlation	0.8 GHz bandwidth stationary measurements
[21]	ESTG	Sliding correlation	2 GHz bandwidth 2000 snapshots/s
[22]	University of VIGO	Sliding correlation	0.5 GHz bandwidth stationary measurements
[23]	Ilmenau-01	M-sequence direct correlation	7 GHz bandwidth 200 snapshots/s
This work	Brno University of Technology	Golay sequence direct correlation	8 GHz bandwidth up to 700000 snapshots/s

Tab. 1.1: Channel sounder systems list.

2 AIMS OF THE DISSERTATION

Based on previous chapters, it is obvious that the current available methods for channel measurements are not capable to capture all of the millimeter wave band channel features. The combination of huge bandwidth, fast channel variations and great dynamic range makes it very challenging.

The *primary* goal of this thesis is therefore to design and build a channel sounding system, which will be optimized for measuring those complicated channels. The requirements for this system are following:

- It will be predominately made of off-the-shelf components because various instruments are already available at the author's university.
- The transmitting and receiving parts should be separated to enable various measurement scenarios.
- The band of the interest will be the MMW, e.g. ~55–65 GHz because it is (at least partially) available for unlicensed use.
- The captured bandwidth should be at least in order of several GHz to enable close multipath components separation.
- The measurement rate should reach several thousand or tens of thousands measurements per second in order to unambiguously measure channels with Doppler spread up to several kHz.
- The dynamic range of the system shall top off about 40–50 dB so even weak multipath components can be identified. It also eases measurements of some scenarios where the received power varies rapidly, e.g. cars approaching towards each other.

The *secondary* goal is to perform actual measurements with the developed system. The scenarios could be following:

- Measurements of the channel inside a single vehicle (intra-car channel).
- Measurements of the V2V channel.
- Measurements of the V2I channel.

The steps, which will ultimately lead to achieve those goals, could be as follows:

- Develop a basic concept of the channel sounding system with transmitting and receiving parts sharing the same time reference and physical place. This will enable at least the intra-car channel measurements and will reveal where to focus on the improvements in terms of e.g. the dynamic range.
- Upgrade the system by splitting the transmit and receive parts. This will enable all measurement scenarios, including the V2V and V2I channels, but on the other hand, brings challenges like synchronization and triggering issues.

3 MILLIMETER WAVE BAND TIME DOMAIN CHANNEL SOUNDER

This chapter is based on the following published paper:

J. Vychodil, M. Pospíšil, A. Prokeš, and J. Blumenstein, "Millimetre wave band time domain channel sounder," *IET Communications*, vol. 13, no. 3, pp. 331–338, January 2019.

Author of this thesis contribution

All of the work, presented in this chapter, including the measurement setup architecture, data processing concept, system performance and probing signal analysis, and IQ imbalance compensation, was done entirely by the author of this thesis with little help and consultation with the co-authors.

3.1 System description

A simplified block diagram of the proposed channel sounding system is depicted in Fig. 3.1. An Anritsu Signal Quality Analyzer MP1800A serves as a baseband binary sequence generator at data rates up to $f_{\text{chip}} = 12.5$ Gbits/s with maximum RF output power of 13 dBm. A Tektronix Digital Sampling Oscilloscope MSO72004C is utilized as a receiver. It provides 4 channels, 16 GHz bandwidth, 50 GS/s real time acquisition rate and 31.25 MS of data storage per channel. The Signal Quality Analyzer also provides 10 MHz reference and a gating (triggering) signal to the oscilloscope. The Power Amplifier (PA) and Low Noise Amplifier (LNA) (not depicted) are the QuinStar QPW-50662330 and QLW-50754530-I2 respectively. A PC can be used to control the instruments, interchange data and to provide additional features (e.g. real-time and continuous channel sounding), but is not necessary for the data acquisition.

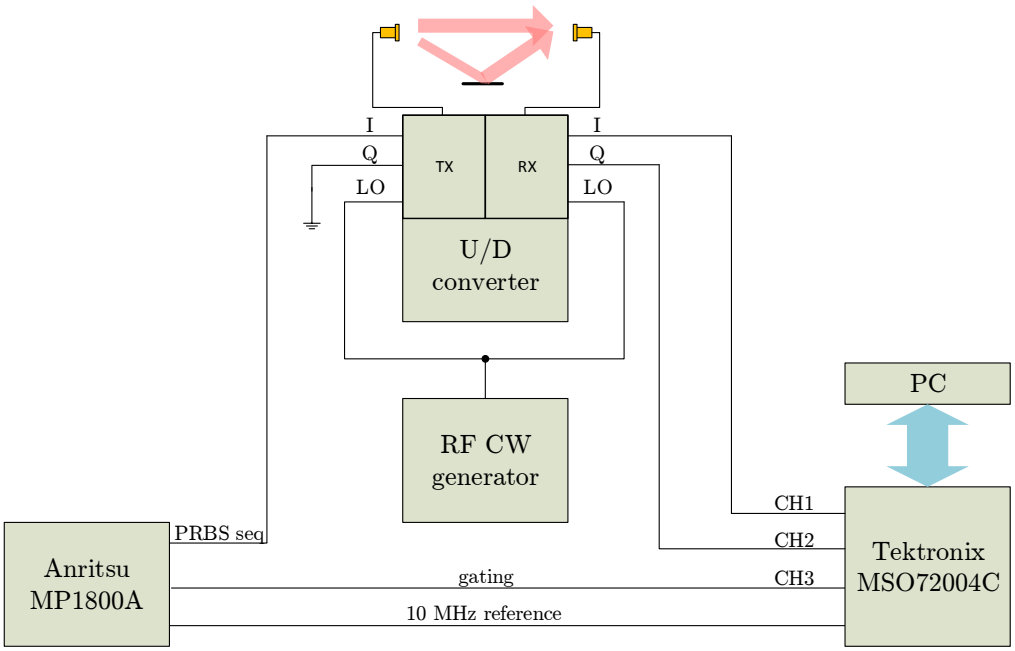

Fig. 3.1: Proposed MMW channel sounder architecture.

The Sivers IMA FC1003V/01 [24] up-down converter is used for frequency shifts between the baseband and the radio frequency. It is a direct conversion transceiver (sometimes called homodyne or zero-IF) with IF input bandwidth up to 5 GHz. The transmitted baseband signal is filtered by a low pass filter with cut off frequency of 5 GHz and then fed into the I branch of the up converter. The Q branch is terminated by a 50 Ω termination load. In an ideal case this results in an Amplitude Modulation (AM) with a symmetrical spectrum around the carrier frequency $f_c =$

59.6 GHz. The RF signal then propagates through the channel, which is the object of the measurement. For the channel sounding, typically an open ended WR15 waveguide is used, as it is very simple and it offers an acceptable radiation pattern [25]. The received signal is then down converted and the output signal — complex, in the form of I and Q components — is passed to the oscilloscope for sampling and further processing. To achieve perfect coherency the Local Oscillator (LO) signal is generated in an Agilent RF generator 83752A then it is split in the Wilkinson power divider and fed into the up-down converter LO inputs. Alternatively, the Sivers IMA FC1005V/00 [26] up-down converter can be used. This converter contains two PLL synthesizers, but due to their large group delay variation (1 ns/GHz), they have to be disconnected and replaced by a power splitter and a more stable RF generator, e.g. the aforementioned Agilent 83752A.

In our case, a seamless repeating binary sequence is used as the excitation signal. The length of the binary sequence is N chips. The number of chips determines the time period of the sequence, which corresponds to the maximum observable CIR time span given by

$$T = \frac{N}{f_{\text{chip}}} = N \cdot \Delta t, \tag{3.1}$$

where $\Delta t = \frac{1}{f_{\text{chip}}}$ is the time duration of one chip. The parameter T is related to the maximum observable propagation distance by

$$D_{\max} = c \cdot T = c \cdot \frac{N}{f_{\text{chip}}} = c \cdot N \cdot \Delta t, \tag{3.2}$$

where $c \approx 3 \times 10^8\,\mathrm{m\,s^{-1}}$ is the speed of light. Considering $N \approx 2^{11} = 2048$ and $f_{\text{chip}} = 12.5$ GHz, the maximum propagation distance is $D_{\max} \approx 49$ m, which is sufficient for most of the short-range MMW channels.

Correlation gain, which can be viewed as simple averaging of N equivalent samples with additive white Gaussian noise, is given by [27]

$$G_{\text{corr}} = 10 \cdot \log N, \tag{3.3}$$

when considering the probing sequence as perfect or almost perfect. This property is discussed in Sec. 3.2.2. For example, if $N = 2048$, the correlation gain is $G_{\text{corr}} = 33.11$ dB.

The main advantage of the proposed channel measurement system is the CIR measurement time. The time to measure one single CIR equals the time length of the sequence given by Eq. (3.1). Considering $N = 2048$, this leads to $T = 0.164\,\mu\mathrm{s}$. The reciprocal value, $f_{\text{meas}} = \frac{1}{T}$ denotes the maximum CIR measurements per second. For $N = 2048$, this is theoretically 6.1 million measurements per second. The oscilloscope provides 31.25 MS of fast acquisition memory per channel, which equals

to 0.625 ms at a sampling rate of 50 GS/s, so only 3816 CIRs can be captured at once. Nevertheless, using advanced triggering modes, the f_{meas} can be decreased to an arbitrary value. It is also possible to continuously stream the real time acquired data to a PC at the rate $f_{\text{meas}} \approx 100$ Hz. In static channel measurement scenarios, averaging of the data can be utilized to further improve the SNR.

3.2 Definitions

Several terms, which will be used in this chapter, are defined in this section.

3.2.1 Cross-correlation function

The cross-correlation between two complex valued functions $a(t)$ and $b(t)$ can be defined as

$$R_{ab}(\tau_1) = \int_{-\infty}^{\infty} a(t)b^*(t-\tau_1)\mathrm{d}t, \tag{3.4}$$

where * denotes complex conjugation. When considering $a(t)$ and $b(t)$ periodic with period T, the cross-correlation can be defined as

$$R_{ab}(\tau_1) = \frac{1}{T}\int_{0}^{T} a(t)b^*(t-\tau_1)\mathrm{d}t = \overline{a(t)b^*(t-\tau_1)}, \tag{3.5}$$

where $\overline{}$ means time (t) average over one period (T) of the signal. The cross-correlation is often performed utilizing the Fourier transform for faster calculation as

$$\hat{R}_{ab}(f_1) = \hat{a}(f_1)[\hat{b}(f_1)]^*, \tag{3.6}$$

where $\hat{}$ denotes the Fourier transform, i.e. $\hat{a}(f_1) = \mathcal{F}\{a(\tau_1)\}$.

3.2.2 Autocorrelation function

The autocorrelation function of the signal $a(t)$ can be obtained from Eq. 3.4 by letting $b(t) = a(t)$. If the signal $a(t)$ is periodic with period T, the autocorrelation function can be obtained in the same way from Eq. 3.5. Because this work is focused on periodic binary (e.g. real valued) sequences, it will be more convenient to examine the discrete time periodic (circular) autocorrelation function

$$R_{aa}[\tau_1] = \frac{1}{N}\sum_{n=0}^{N-1} a[n]a[n-\tau_1], \tag{3.7}$$

where N is the number of chips of sequence $a[n]$ and the indexes are computed via the modulo N operation, e.g. $a[n] \equiv a[n \bmod N]$. The ideal shape of $R_{aa}[\tau_1]$,

suitable for the purposes of channel sounding, is the unit impulse,

$$R_{aa}[\tau_1] = \begin{cases} 1 & \text{if } \tau_1 = 0 \\ 0 & \text{elsewhere.} \end{cases} \tag{3.8}$$

Signals with this property are called perfect. If a signal with this property is transformed into continuous time digital signal with chip period Δt, the corresponding $R_{aa}(\tau_1)$ is a triangle shaped signal with its base spanning from $-\Delta t$ to Δt and height 1. Given a band limited function $s(t)$ with bandwidth $B \ll \frac{1}{\Delta t}$, it can be approximated

$$\int_{-\Delta t}^{\Delta t} s(\tau_1) R_{aa}(\tau_1) \mathrm{d}\tau_1 \approx \Delta t \cdot s(0). \tag{3.9}$$

3.2.3 Higher order autocorrelation function

If we consider the signal $a(t)$ as real and $b(t) = a(t)$, we can write Eq. 3.4 as

$$R_{aa}(\tau_1) = \int_{-\infty}^{\infty} a(t) a(t - \tau_1) \mathrm{d}t. \tag{3.10}$$

This (first order) autocorrelation function (of a real valued signal) can be extended to the i-th order autocorrelation function as

$$R_{a\ldots a}(\tau_1, \ldots, \tau_i) = \int_{-\infty}^{\infty} a(t) a(t - \tau_1) \ldots a(t - \tau_i) \mathrm{d}t. \tag{3.11}$$

Please note that the i-th order autocorrelation function is symmetric, meaning that its value is the same for any permutation of input parameters, for example $R_{aaa}(\tau_1, \tau_2) = R_{aaa}(\tau_2, \tau_1)$ or $R_{aaaa}(\tau_1, \tau_2, \tau_3) = R_{aaaa}(\tau_1, \tau_3, \tau_2) = R_{aaaa}(\tau_2, \tau_1, \tau_3) = R_{aaaa}(\tau_2, \tau_3, \tau_1) = R_{aaaa}(\tau_3, \tau_1, \tau_2) = R_{aaaa}(\tau_3, \tau_2, \tau_1)$ and so on. Similarly as in Eq. 3.5, it is possible to write a higher order autocorrelation function of a periodic signal as

$$\begin{aligned} R_{a\ldots a}(\tau_1, \ldots, \tau_i) &= \frac{1}{T} \int_0^T a(t) a(t - \tau_1) \ldots a(t - \tau_i) \mathrm{d}t \\ &= \overline{a(t) a(t - \tau_1) \ldots a(t - \tau_i)}. \end{aligned} \tag{3.12}$$

Similarly, as in Eq. 3.7, it is possible to write a discrete time higher order autocorrelation function as

$$R_{a\ldots a}[\tau_1, \ldots, \tau_i] = \frac{1}{N} \sum_{n=0}^{N-1} a[n] a[n - \tau_1] \ldots a[n - \tau_i]. \tag{3.13}$$

Considering $R_{a...a}[\tau_1, \ldots, \tau_i]$ i-dimensional unit impulse, e.g.

$$R_{a...a}[\tau_1, \ldots, \tau_i] = \begin{cases} 1 & \text{if } \tau_1 = \cdots = \tau_i = 0 \\ 0 & \text{elsewhere,} \end{cases} \tag{3.14}$$

for the corresponding $R_{a...a}(\tau_1, \ldots, \tau_i)$ given band limited function $s(t_1, \ldots, t_i)$ with bandwidth $B \ll \frac{1}{\Delta t}$, it can be approximated

$$\begin{aligned} &\int_{-\Delta t}^{\Delta t} \cdots \int_{-\Delta t}^{\Delta t} s(t_1, \ldots, t_i) \\ &R_{a...a}(\tau_1, \ldots, \tau_i)\mathrm{d}\tau_1 \ldots \mathrm{d}\tau_i \approx (\Delta t)^i \cdot s(0, \ldots, 0) \end{aligned} \tag{3.15}$$

as a generalization of Eq. 3.9.

The higher order autocorrelation function can also be computed utilizing the Fourier transform as [28]

$$\hat{R}_{a...a}(f_1, \ldots, f_i) = \hat{a}(f_1)\hat{a}(f_2) \ldots \hat{a}(f_i)[\hat{a}(f_1 + f_2 + \cdots + f_i)]^*, \tag{3.16}$$

where $\hat{}$ denotes the i-dimensional Fourier transform, i.e. $\hat{a}(f_1, \ldots, f_i) = \mathcal{F}\{a(\tau_1, \ldots, \tau_i)\}$.

It will be shown later in this thesis that the higher order autocorrelation function can be used to characterize the measurement output when the channel (or the system) under test exhibits non-linear behavior.

3.2.4 Ambiguity function

The (narrowband) ambiguity function of signal $a(t)$, often used in radar signal processing, can be defined as [29]

$$\chi(\tau_1, f) = \int_{-\infty}^{\infty} a(t)a^*(t - \tau_1)e^{i2\pi ft}dt, \tag{3.17}$$

where i is the imaginary unit and f is the Doppler frequency shift. It basically shows the change of the shape of the autocorrelation function caused by the relative movement of the transmitter and receiver (the Doppler effect). Due to relatively low transmitter and receiver relative speeds (maximum tens or hundreds of $\mathrm{m\,s^{-1}}$), huge bandwidth and very short measurement times in our scenario, the Doppler effect affecting single measurement is negligible. The slice at $f = 0$ of the ambiguity function is the autocorrelation function, i.e.

$$\chi(\tau_1, 0) = R_{aa}(\tau_1). \tag{3.18}$$

3.3 Basic principle of operation

The measured channel can be modeled as a linear time invariant system whose input-output relationship can be expressed as

$$y(t) = \int_{-\infty}^{\infty} g_1(\tau_1)u(t-\tau_1)\mathrm{d}\tau_1, \tag{3.19}$$

where $u(t)$ is the input of the system, $y(t)$ is its output and $g_1(\tau_1)$ is the channel impulse response.

There are many types of excitation signals which can be utilized in order to perform channel sounding. One can use, for example, frequency sweeps (chirps), binary sequences or some more complicated signals, e.g. Orthogonal Frequency Division Multiplex (OFDM)-like signals or Zadoff-Chu sequences [30]. This work focuses on the use of the binary sequences signal group because they are easily generated and modulated to the desired frequency band using inexpensive hardware.

In the scope of this work, the two types of binary signals are examined — the Maximum Length Sequences (MLSs), sometimes called m-sequences and Golay complementary pairs. As was stated earlier, the signal $u(t)$ is a seamless repeating sequence with the number of chips N, period of T and duration of one chip Δt. Since it is assumed that the $g_1(\tau_1)$ is causal and has a finite length of T, i.e.

$$g_1(\tau_1) = 0 \text{ for } \tau_1 > T \text{ and } \tau_1 < 0, \tag{3.20}$$

and the input signal $u(t)$ is periodic with period T, Eq. 3.19 can be rewritten as

$$y(t) = \int_{0}^{T} g_1(\tau_1)u(t-\tau_1)\mathrm{d}\tau_1. \tag{3.21}$$

The m-sequence cross-correlation method is a widely used approach for measuring impulse responses of linear systems. For example, it is used in many time domain channel sounders, like it was shown in [9] or [5]. M-sequences have several properties which makes them appropriate for channel sounding. They are easily generated by the Linear Feedback Shift Register (LFSR) and have an almost perfect circular autocorrelation function

$$R_{uu}[\tau_1] = \begin{cases} 1 & \text{if } \tau_1 = 0 \\ -\frac{1}{N} & \text{elsewhere.} \end{cases} \tag{3.22}$$

An example of a circular autocorrelation function of a short m-sequence is depicted in Fig. 3.2.

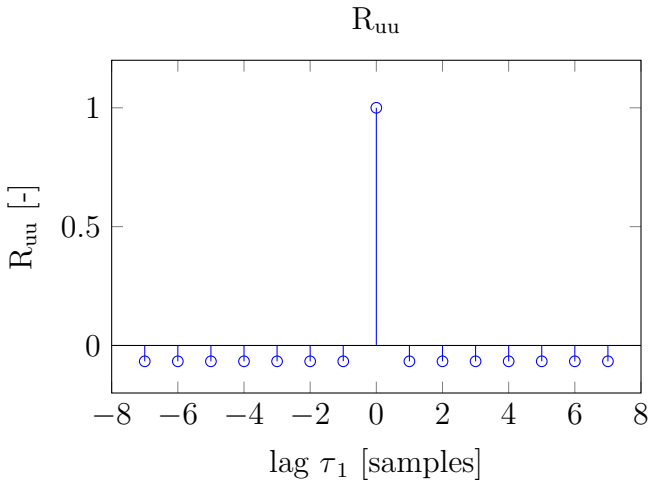

Fig. 3.2: Circular autocorrelation function of a m-sequence.

The cross-correlation between the output $y(t)$ and input $u(t)$ can be expressed using Eq. 3.5 as [31]

$$R_{yu}(\tau) = \overline{u(t-\tau)y(t)}, \tag{3.23}$$

where $\overline{\quad}$ means time (t) average over one period (T) of the signal. When considering the system described by Eq. 3.21, the cross-correlation becomes

$$\begin{aligned} R_{yu}(\tau) =& \overline{u(t-\tau)y(t)} \\ =& \overline{u(t-\tau)\int_0^T g_1(\tau_1)u(t-\tau_1)\mathrm{d}\tau_1} \\ =& \int_0^T g_1(\tau_1)\overline{u(t-\tau)u(t-\tau_1)}\mathrm{d}\tau_1 \\ =& \int_0^T g_1(\tau_1)\overline{u(t)u(t-\tau_1+\tau)}\mathrm{d}\tau_1 \\ =& \int_0^T g_1(\tau_1)R_{uu}(\tau_1-\tau)\mathrm{d}\tau_1, \end{aligned} \tag{3.24}$$

where $R_{uu}(\tau)$ is the autocorrelation function of the input sequence $u(t)$. Using Eq. 3.9 or 3.15, Eq. 3.24 then becomes

$$R_{yu}(\tau) \approx \Delta t \cdot g_1(\tau), \tag{3.25}$$

which is an estimate of the measured CIR.

3.4 Operation in the presence of non-linearities

Real-world (and not only) electronic devices like amplifiers, mixers, etc., used in the measurement chain, exhibit at least weak non-linear behavior. When the measured system is non-linear, the resulting estimate of the channel impulse response contains artefacts, which are not part of the linear impulse response. An example of a measurement result using the proposed system and the m-sequence is shown in Fig. 3.3 (a). The measurement is done only in the baseband, e.g. the up-down converter is not used and the output of the generator is connected directly into one channel of the oscilloscope using a coaxial cable. Several thousands of measurements are averaged to improve the SNR in order to provide a better demonstration. It is possible to see the direct path located at roughly 15 ns and also some spurious peaks located at 8 ns and 110 ns, which are caused by the non-linearities. Please note that there are other components besides the main path which are caused by the low pass filter behavior of the coaxial cable and by the reflections. However, those components are fundamentally linear and thus can be easily removed by means of calibration or normalization.

The metric used in the scope of this thesis for comparing the performance of different systems or sequences is the Spurious-Free Dynamic Range (SFDR). It is the ratio of the strongest wanted component and the strongest spurious or noise component. The SFDR is also shown graphically in Fig. 3.3.

When the system is weakly non-linear, its input-output relation can be expressed using the Volterra series expansion, which is a generalization of the system impulse response and the Taylor series, as

$$\begin{aligned} y(t) &= \int_0^T g_1(\tau_1)u(t-\tau_1)\mathrm{d}\tau_1 \\ &+ \int_0^T\int_0^T g_2(\tau_1,\tau_2)u(t-\tau_1)u(t-\tau_2)\mathrm{d}\tau_1\mathrm{d}\tau_2 \\ &+ \int_0^T\int_0^T\int_0^T g_3(\tau_1,\tau_2,\tau_3)u(t-\tau_1)u(t-\tau_2)u(t-\tau_3)\mathrm{d}\tau_1\mathrm{d}\tau_2\mathrm{d}\tau_3 \\ &+ \dots \\ &+ \int_0^T \dots \int_0^T g_i(\tau_1,\dots,\tau_i)u(t-\tau_1)\dots u(t-\tau_i)\mathrm{d}\tau_1\dots\mathrm{d}\tau_i \end{aligned} \tag{3.26}$$

or in shorter form as

$$y(t) = \sum_{i=1}^{\infty} \int_0^T \dots \int_0^T g_i(\tau_1,\dots,\tau_i)u(t-\tau_1)\dots u(t-\tau_i)\mathrm{d}\tau_1\dots\mathrm{d}\tau_i, \tag{3.27}$$

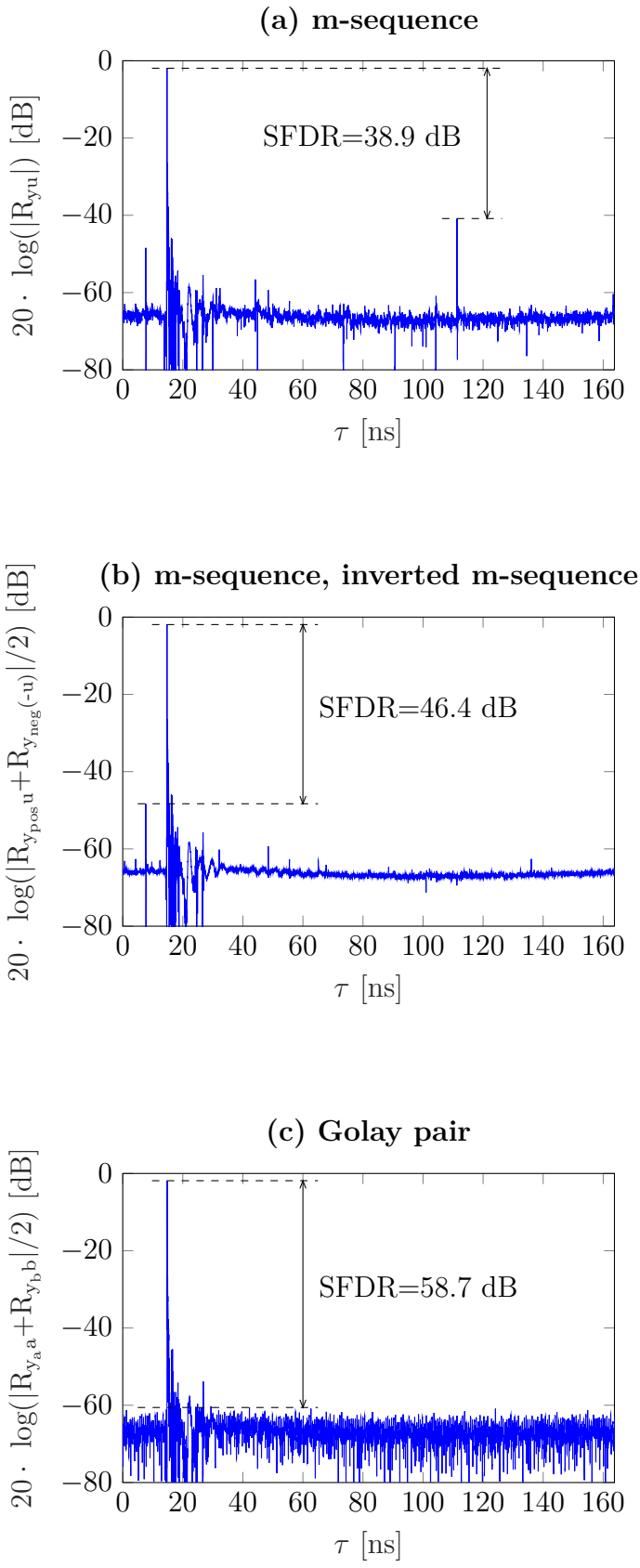

Fig. 3.3: Example of baseband back-to-back measurement using different sequences. (a) m-sequence; (b) m-sequence, inverted m-sequence; (c) Golay pair.

where $u(t)$ is the input to the system, $y(t)$ is the output of the system and $g_i(\tau_1, \ldots, \tau_i)$ is the i-th order Volterra kernel, which can be viewed as a higher order impulse response of the system. Please note that if the system is linear, only the first order Volterra kernel $g_1(\tau_1)$ (first term of Eq. 3.26) is non zero. The equation then reduces to an ordinary convolution, where $g_1(\tau_1)$ is the linear impulse response, e.g. the equation becomes Eq. 3.19.

To provide an example, consider one of the simplest non-linear systems, the so-called Wiener model. This model consists of a cascade of a linear memory block which can be characterized by its impulse response $h(\tau)$ and a static (memory-less) non-linearity which can be modeled by a (possibly truncated) polynomial, e.g.

$$y(t) = c_1 z(t) + c_2 z^2(t) + c_3 z^3(t), \tag{3.28}$$

when considering non-linearities only up to the third order. The i-th order Volterra kernel of this system is then [32]

$$g_i(\tau_1, \ldots, \tau_i) = c_i h(\tau_1) \ldots h(\tau_i). \tag{3.29}$$

This model is mentioned here only to provide a better insight into how the Volterra kernels can appear in practice. The principles described in this thesis apply to the general Volterra model, defined above in Eq. 3.27.

The cross-correlation between the the output $y(t)$ and input $u(t)$ using Equations 3.12, 3.27 and 3.23 can be rewritten as [33]

$$\begin{aligned} R_{yu}(\tau) =& \overline{u(t-\tau)y(t)} \\ =& \overline{u(t-\tau) \sum_{i=1}^{\infty} \int_0^T \ldots \int_0^T g_i(\tau_1, \ldots, \tau_i) \cdot u(t-\tau_1) \ldots u(t-\tau_i) \mathrm{d}\tau_1 \ldots \mathrm{d}\tau_i} \\ =& \sum_{i=1}^{\infty} \int_0^T \ldots \int_0^T g_i(\tau_1, \ldots, \tau_i) \cdot \overline{u(t-\tau)u(t-\tau_1) \ldots u(t-\tau_i)} \mathrm{d}\tau_1 \ldots \mathrm{d}\tau_i \\ =& \sum_{i=1}^{\infty} \int_0^T \ldots \int_0^T g_i(\tau_1, \ldots, \tau_i) \cdot R_{u \ldots u}(\tau_1 - \tau, \ldots, \tau_i - \tau) \mathrm{d}\tau_1 \ldots \mathrm{d}\tau_i. \end{aligned} \tag{3.30}$$

Now, let's introduce one of the properties of the m-sequences, the so-called shift and add property [34]. It arises from the method of how they are generated using the LFSR. When we take any m-sequence and multiply it by the same but shifted sequence, we obtain the same sequence, but with a different time shift. For example, with the sequence $u[n]$ having a length of 15 chips

$$\begin{aligned} u[n] =& [\circ\,\circ\,\circ\,\circ\,\bullet\,\circ\,\bullet\,\circ\,\circ\,\bullet\,\bullet\,\circ\,\bullet\,\bullet\,\bullet] \\ \cdot u[n-1] =& [\bullet\,\circ\,\circ\,\circ\,\circ\,\bullet\,\circ\,\bullet\,\circ\,\circ\,\bullet\,\bullet\,\circ\,\bullet\,\bullet] \\ \hline = u[n-4] =& [\circ\,\bullet\,\bullet\,\bullet\,\circ\,\circ\,\circ\,\circ\,\bullet\,\circ\,\bullet\,\circ\,\circ\,\bullet\,\bullet], \end{aligned} \tag{3.31}$$

where the -1 and 1 numbers are for better illustration represented by ○ and ● symbols, respectively. It can be clearly seen that the original sequence multiplied by the same sequence but shifted by one chip to the right equals the same sequence but shifted by 4 chips to the right. The shifts are unique for every m-sequence and can be determined from the feedback connections of the generating LFSR (or from the generating polynomial) of the m-sequence. Based on this property, it is now obvious that the second and higher order autocorrelation function of the m-sequence can be expressed as

$$R_{u\ldots u}[\tau_1,\ldots,\tau_i] = \begin{cases} 1 & \text{under certain values of } \tau_1,\ldots,\tau_i \\ -\frac{1}{N} & \text{otherwise.} \end{cases} \tag{3.32}$$

For better illustration, the second order autocorrelation function of the very same m-sequence, which was used in previous examples, is depicted in Fig. 3.4. Its slices of third order autocorrelation function are depicted in Fig. 3.5.

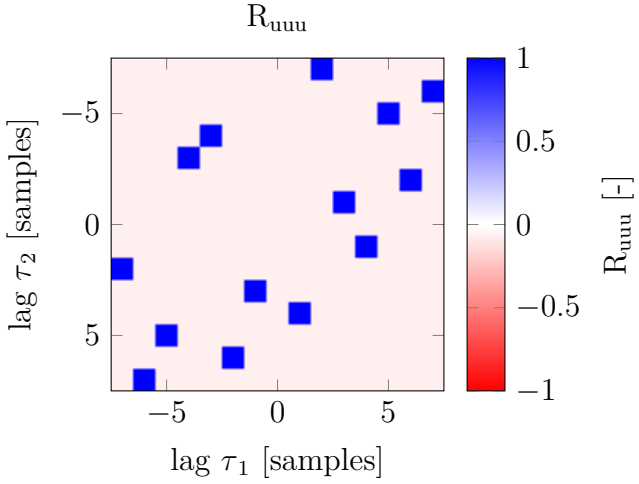

Fig. 3.4: Second order circular autocorrelation function of m-sequence.

Based on those observations, Eq. 3.30 then can be approximated, using Eq. 3.15 and taking into account only the first, second and third order Volterra kernels, which is a basic commonly used approximation, as

$$\begin{aligned} R_{yu}(\tau) \approx & \Delta t g_1(\tau) + F_3(\tau) \\ & + 2! \sum_{j=1}^{m_2} (\Delta t)^2 g_2(\tau - k_{21}^{(j)}\Delta t, \tau - k_{22}^{(j)}\Delta t) \\ & + 3! \sum_{j=1}^{m_3} (\Delta t)^3 g_3(\tau - k_{31}^{(j)}\Delta t, \tau - k_{32}^{(j)}\Delta t, \tau - k_{33}^{(j)}\Delta t), \end{aligned} \tag{3.33}$$

where the integers $k_{ir}^{(j)} (1 \leq r \leq i)$ are the unique shift coefficients of the m-sequence which can be derived from the generating polynomial of the sequence or can be

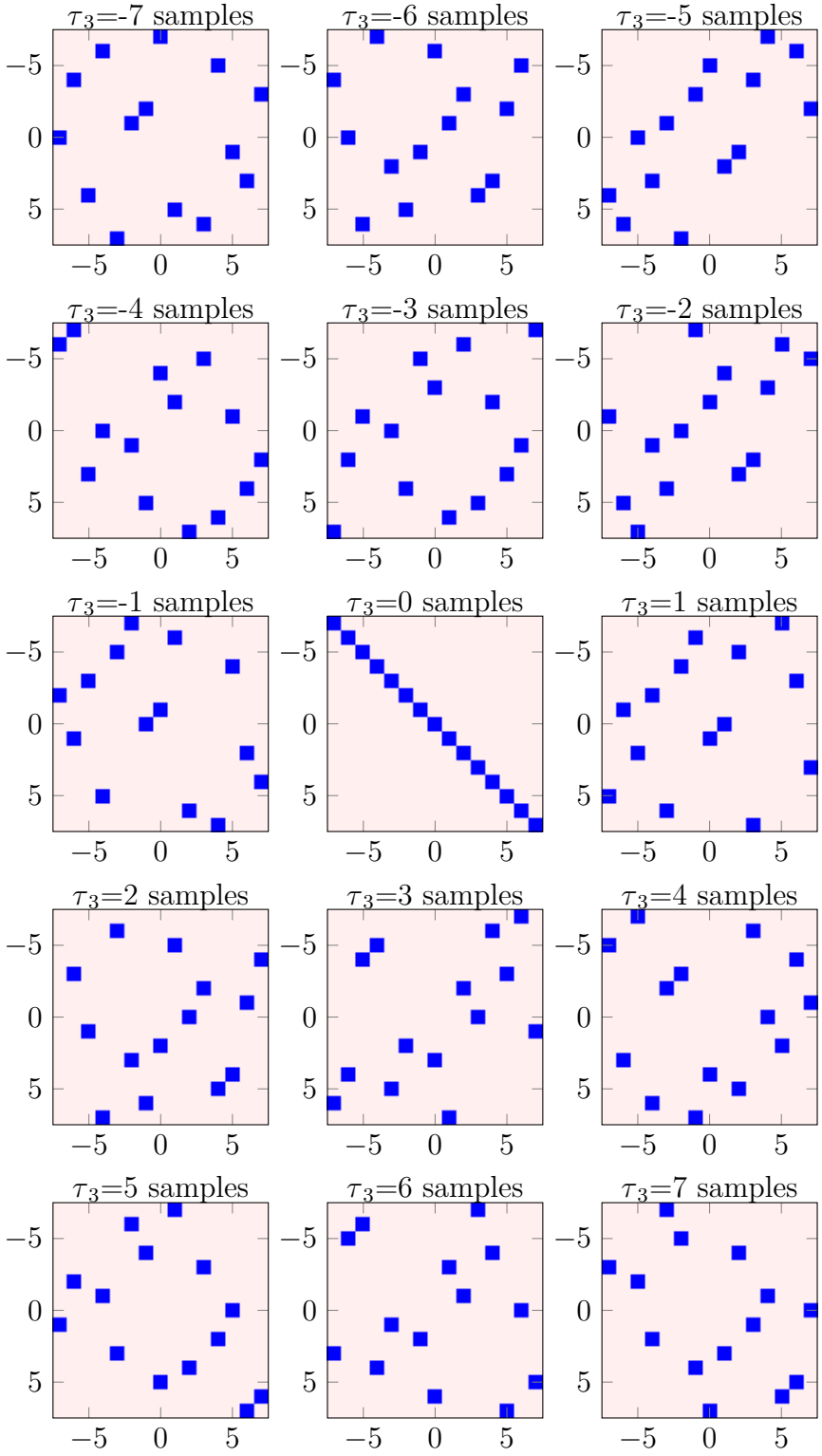

Fig. 3.5: Third order circular autocorrelation function of m-sequence.

observed on the high order autocorrelation functions drawings, m_i is the count of the sets of numbers $k_{ir}^{(j)}$. The constants 2! and 3! emerges from the symmetry of the

higher order autocorrelation functions. We can observe that the cross-correlation now contains the first order kernel (linear impulse response) and also shifted cross sections of higher order kernels. The term $F_3(\tau)$ is the sum of the third order Volterra kernels which have one or more parameters the same and equals to

$$F_3(\tau) = (\Delta t)^3 g_3(\tau,\tau,\tau) + 3(\Delta t)^3 \sum_{q=1}^{m_1} g_3(\tau, q, q). \tag{3.34}$$

3.4.1 Unobservable and overlapped kernels

As can be seen, there are several parts of the Volterra kernels that are not directly observable or are overlapped with other kernels.

In the concrete, we cannot observe any second order Volterra kernel which has an equal parameter, e.g. $g_2(q,q)$. This is because when the binary m-sequence is multiplied by the same m-sequence, the result is a constant 1, e.g. $u(t) \cdot u(t) = 1$ [35]. This can be generalized for all even order kernels but in the scope of this work, only kernels up to third order are considered.

From Eq. 3.34 we can see that any third order Volterra kernel, which have one or more parameters the same, overlaps with the first order kernel. The explanation is as follows: $u(t) \cdot u(t) \cdot u(t) = u(t)$ or more generally $u(t) \cdot u(t-\tau) \cdot u(t-\tau) = u(t)$. This property can also be generalized for all odd order kernels.

3.4.2 Mitigating the effects of even order kernels

It is possible to easily mitigate the effects of even order distortion by exploiting the property that

$$R_{(-u)\ldots(-u)}(\tau_1,\ldots,\tau_i) = \begin{cases} R_{u\ldots u}(\tau_1,\ldots,\tau_i) & \text{for odd } i \\ -R_{u\ldots u}(\tau_1,\ldots,\tau_i) & \text{for even } i. \end{cases} \tag{3.35}$$

The system is first probed by $u(t)$ and then by $-u(t)$. Outputs of the measurements (y_{pos} and y_{neg}, respectively) are then cross-correlated with their corresponding inputs and averaged to obtain an estimate of $g_1(\tau)$ which is not affected by even order distortion, e.g.

$$g_1(\tau) \approx \frac{1}{2\Delta t}(R_{y_{pos}u} + R_{y_{neg}(-u)}). \tag{3.36}$$

An example of such measurement is shown in Fig. 3.3 (b). The measurement setup is the same as in Fig. 3.3 (a). It can be clearly seen that the spurious peak located at 110 ns and some others have completely vanished. However, there are some others, for example that located at 8 ns, which remained because they were caused by odd order non-linear distortion. Nevertheless, the SFDR improved by 7.5 dB.

3.4.3 Golay complementary sequences as an input signal

Another great candidate for channel probing signal are the Golay complementary sequences pairs [36]. They are easily constructed by recursive algorithms and have a perfect (both aperiodic and periodic) autocorrelation function. A deeper description of Golay complementary sequences is beyond the scope of this thesis, but to illustrate consider $a[n]$ and $b[n]$ complementary sequences of length 16 chips. Their circular autocorrelation functions are depicted in Fig. 3.6. An average (sum divided by two)

Fig. 3.6: Circular autocorrelation functions of complementary pairs.

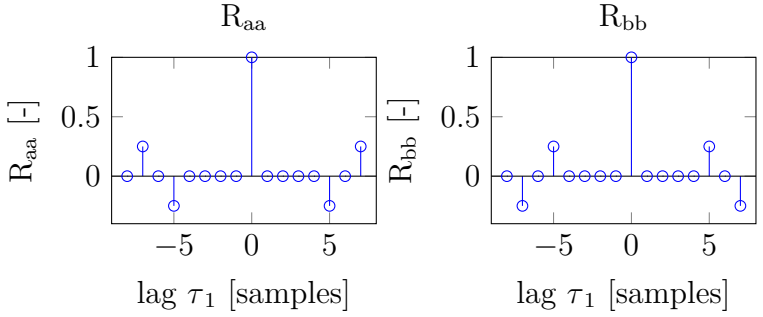

of those autocorrelation functions is perfect, e.g.

$$(R_{aa}[\tau_1] + R_{bb}[\tau_1])/2 = \begin{cases} 1 & \text{if } \tau_1 = 0 \\ 0 & \text{elsewhere.} \end{cases} \tag{3.37}$$

Averages of higher order autocorrelation functions of Golay complementary sequences have also interesting properties. For illustration, the second order autocorrelation function is depicted in Fig. 3.7 and the third order autocorrelation function in Fig. 3.8.

As can be seen, the maximal value of those functions is lower than if m-sequences are used and it even gets lower for longer Golay complementary sequences. Some of the terms are negative and some are positive which can cause that some artefacts, caused by the non-linearities will cancel out. Also, those functions are more noise-like than in the case of m-sequences. That will cause that the artefacts will not appear as spurious peaks as in case of m-sequences, but will be spread over time and will increase the overall noise floor instead.

An example measurement using Golay complementary sequences is depicted in Fig. 3.3 (c). There are practically no spurious peaks, but the overall noise floor is slightly higher as was explained in the previous paragraph. The SFDR has further improved by 12.3 dB. Nevertheless, the amplitude of the estimated impulse response is of course still affected by the non-linearities.

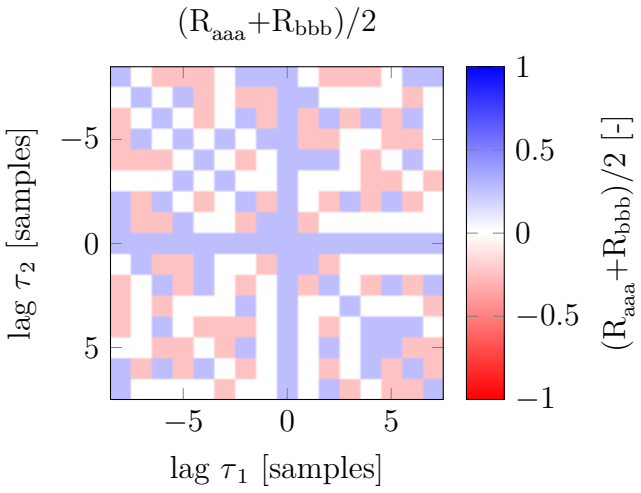

Fig. 3.7: Second order circular autocorrelation function of complementary Golay sequences.

3.4.4 Non-inverted and inverted Golay complementary sequences as an input signal

It is also possible to apply the approach from Sec. 3.4.2 to the Golay complementary sequences. In this case, the system is probed by four sequences: $a(t)$, $-a(t)$, $b(t)$ and $-b(t)$. Outputs of the measurements are then cross-correlated with their corresponding inputs and averaged to obtain an estimate of $g_1(\tau)$, which is not affected by even order distortion, e.g.

$$g_1(\tau) \approx \frac{1}{4\Delta t}(R_{y_{apos}a} + R_{y_{aneg}(-a)} + R_{y_{bpos}b} + R_{y_{bneg}(-b)}). \tag{3.38}$$

3.5 Probing the system with multiple sequences

When the system is probed with only one periodic sequence (for example with the m-sequence, as was shown earlier in Sec. 3), the process of obtaining the CIR at some time instant is straightforward. The sequence is seamlessly repeated at the transmitter and at the receiving side, it is possible to take a snapshot with a length of the sequence T at any time. The estimate of the CIR is then obtained by computing the (circular) cross-correlation between the transmitted and received signal (Eq. 3.25).

However, as was proven earlier, it is often more advantageous to probe the system with two or more sequences. This scenario is depicted in Fig. 3.9. In this example, four sequences $(a, -a, b, -b)$ are used. Every sequence is transmitted twice because the channel introduces some delay and in order to obtain a correct CIR estimate,

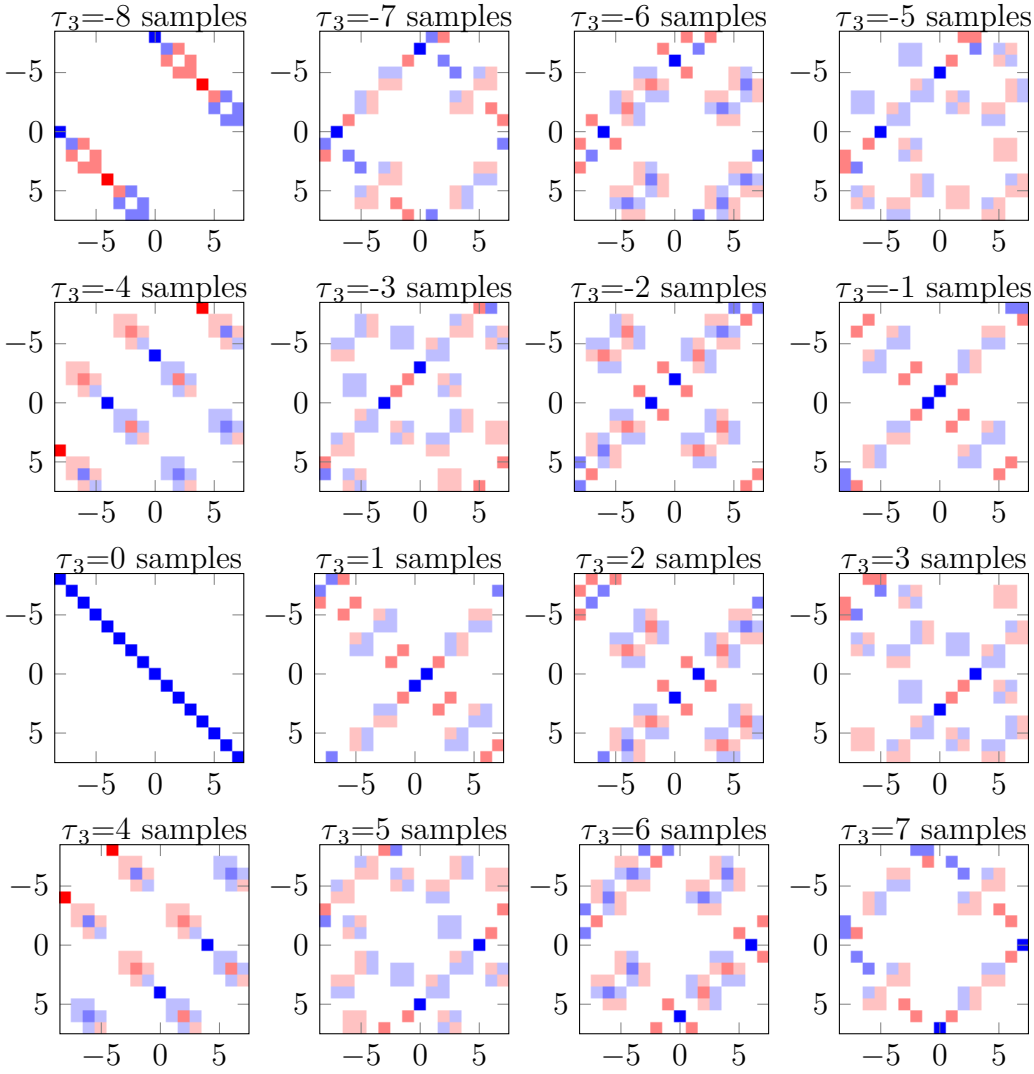

Fig. 3.8: Third order circular autocorrelation function of complementary Golay sequences.

it is needed that the receiving (correlation) window (of length T) contains only the corresponding sequence. This is illustrated in the example by a direct and delayed path. The signals from those paths are added at the receiver and the correlation windows are correctly aligned so that it contains only corresponding sequences.

This approach of course significantly extends the measurement time, during which the channel has to remain static. However, in our measurement scenarios, it is still possible to consider the channel static also for small multiples of T, thus it has a negligible effect on the CIR estimate.

It is also not necessary to repeat each sequence twice; it is possible to repeat only a fraction of the sequence as long as the length of the repeated section is larger than the maximal delay introduced by the channel. This approach is similar to the well

known Cyclic Prefix (CP) which is used commonly in OFDM systems over fading channels. Using this technique, it is possible to adjust the overall signal (set of sequences) length to an arbitrary value. For example, in some of our measurement scenarios, the transmitter and receiver cannot be connected by a reference and triggering cable, so the triggering at the receiving side was performed based on the 10 MHz reference signal, generated locally by a Rubidium or Global Positioning System (GPS) disciplined oscillator. The overall signal length was adjusted to be an exact multiple of the period of this reference signal.

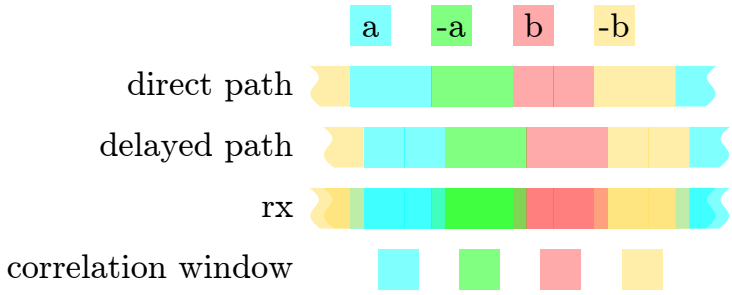

Fig. 3.9: Probing the system with multiple sequences.

3.6 SFDR of the system

3.6.1 SFDR of the baseband system

Results presented in this section were obtained by the back-to-back test of the baseband system, e.g. the output of the baseband binary sequence generator was connected directly to the oscilloscope by a coaxial cable.

The used baseband binary sequence generator offers variable output power from -19 dBm to 13 dBm. Probably due to the variable output amplifier stage, it has different signal purity at various output power levels. Four sets of sequences SFDR were measured and compared. Each sequence has approximately the same length (T), however, each set has a different count of sequences. Each sequence was transmitted twice for the reasons mentioned in the previous section. This, of course, results in different measurement times when using different sets of sequences. The sets with fewer sequences were repeated and averaged to improve the SNR and to provide an objective comparison in terms of measurement time. The used sets and their corresponding properties are summarized in Tab. 3.1. Measurement results are shown in Fig. 3.10. To give a better insight into the performance of individual sets, results where several thousands of measurements were averaged, are also depicted. This helps to differentiate whether the SFDR is limited by the spurs or by noise.

Set name	# of sequences	Meas. time	Averaging factor
m-seq.	1	T	8
m-seq., inv. m-seq.	2	4T	2
Golay pair	2	4T	2
Golay pair, inv. Golay pair	4	8T	1

Tab. 3.1: Sets of sequences used for measurements.

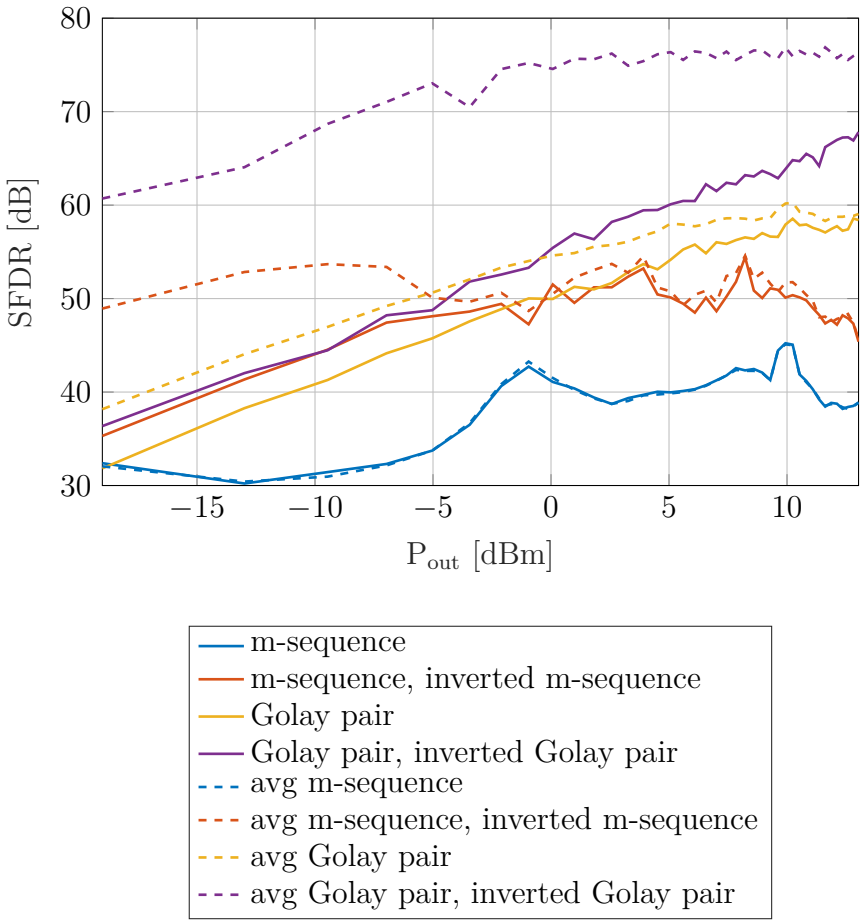

Fig. 3.10: SFDR of the baseband system.

It can be seen that the basic m-sequence has the lowest SFDR under all circumstances and that the SFDR is limited by spurious peaks at all power levels, thus cannot be improved by averaging.

The m-sequence and inverted m-sequence performs better. Its SFDR is limited by the noise of the system to the output power level approximately -5 dBm and then it is limited by the spurs.

As was stated in the previous sections, the Golay complementary pairs behave differently. It can be seen that SFDR can be slightly improved by averaging at all

power levels.

The combined approach of the Golay pairs and inverted Golay pairs, which completely mitigates the effects of the even order kernels and then exploits the Golay pairs' properties, shows superior performance under all circumstances.

3.6.2 SFDR of the system without PA and LNA

The results presented in this section were obtained by the back-to-back test of the system without amplifiers, e.g. the output of the up converter was connected directly to the input of the down converter by waveguides and coaxial cables.

Based on the results described in the previous section, the output level of the baseband generator was set to 10 dBm, where the basic m-sequence has the best performance. This signal was then attenuated to match the input power level of the up converter and fed into its input.

A similar measurement as in the previous section was performed; this time varying the power level of the LO (of both up and down convertor) from 5 dBm to 14 dBm. The results are depicted in Fig. 3.11.

The results are similar to the results carried out in the baseband. It can be seen that the up-down converter starts working at approximately 5 dBm of the LO input power. The SFDR (of all sets of sequences) increases until the power of approximately 9 dBm, where the up-down converter reaches saturation.

The SFDR of the two sets — m-sequence and m-sequence, inverted sequence — in the saturation is limited by the spurs and thus cannot be increased by averaging.

3.6.3 SFDR of the complete system (including PA and LNA)

The results presented in this section were obtained by the back-to-back test of the complete system which is depicted in Fig. 3.1. A variable attenuator was connected between the PA and LNA to simulate the path loss.

Based on the results described in the previous section, the LO power level was set to 9 dBm, where the basic m-sequence shows the best performance. The SFDR performance of all sets of sequences when varying the simulated path attenuation is depicted in Fig. 3.12.

It can be seen that the performance of the system is limited mainly by the noise of the LNA. For this reason, the SFDR of all sets of sequences is almost the same at attenuation levels from 60 dB to 45 dB. At 45 dB of attenuation, the SFDR of the basic m-sequence starts to decrease as a result of the LNA non-linearity. The m-sequence and inverted m-sequence performs better, however, at 40 dB of attenuation, the performance starts to degrade as well.

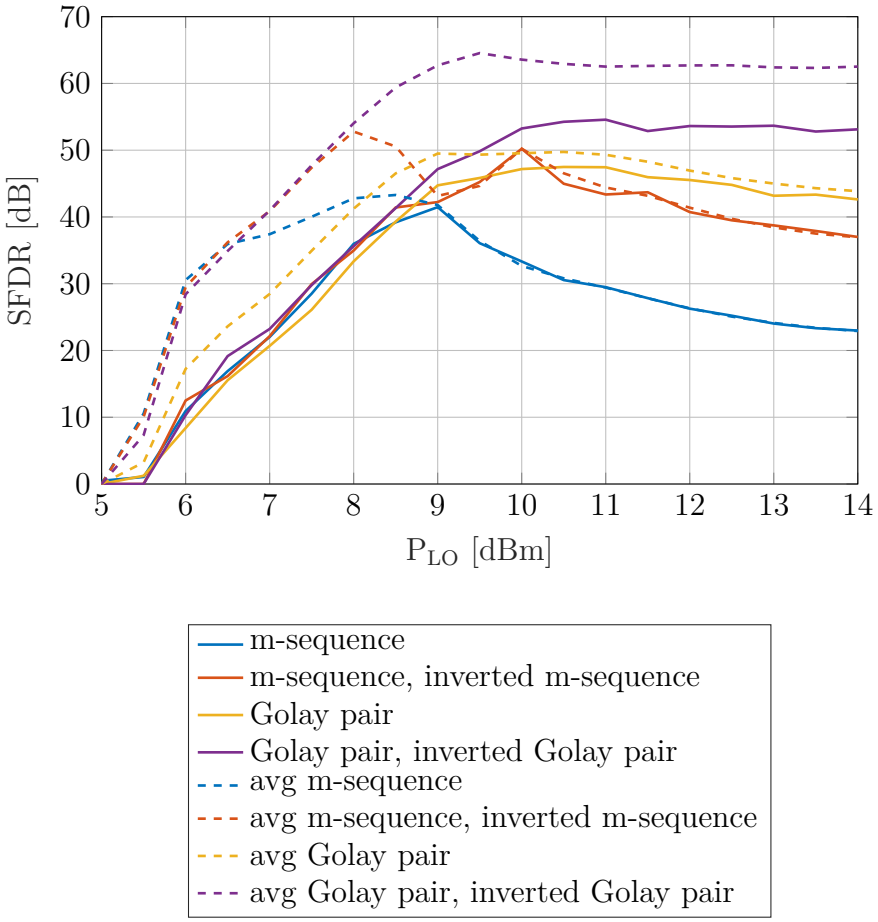

Fig. 3.11: SFDR of the system without PA and LNA.

The remaining two sets show increasing SFDR performance, however, at 35 dB of attenuation, the LNA reaches its 1 dB compression point, so it is inappropriate to increase the power level even more. This leads to maximal SFDR of approximately 40 dB. The averaged results also show that the SFDR can be greatly increased by averaging, however, this impractically extends the measurement time.

3.7 IQ imbalance

The Sivers IMA FC1003V/01 [24] up-down converter, which is utilized in the system, uses a direct conversion (homodyne) architecture. This architecture offers several benefits, such as easy integration, low cost and high selectivity. On the other hand, it suffers from IQ amplitude and phase imbalance. Due to the huge bandwidth of the system, those imbalances are also frequency selective. Detailed discussion on the IQ imbalances issue can be found for example in [37].

This section describes a technique for frequency selective IQ imbalance estima-

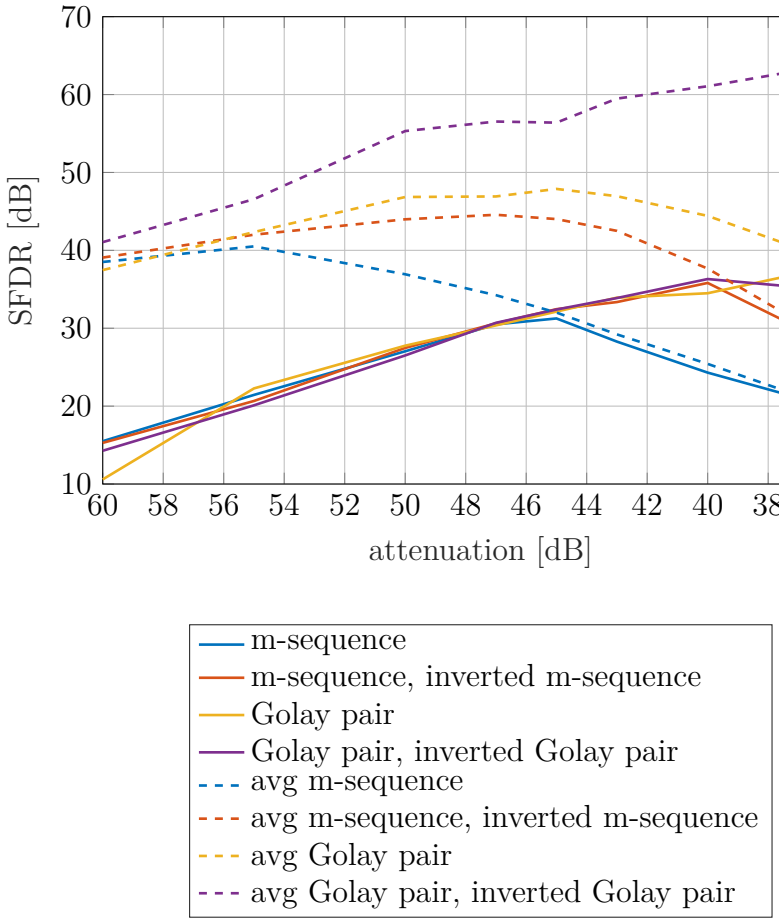

Fig. 3.12: SFDR of the complete system.

tion and compensation for the discussed channel sounder system. A similar system, including its (frequency flat) IQ imbalance calibration utilizing a delay line, was described in [9]. Approach described in this section can be done without any additional hardware (delay line) and compensates for frequency selective IQ imbalance.

As was stated earlier, only one of the IQ inputs is used in the up-converter at the transmitter side, thus the IQ imbalance is a concern only at the receiver side.

In scope of this section, we assume that the non-linear effects are mitigated by the techniques described in the previous section. Thus, we can consider $h(t) \approx g_1(t)$ and $H(f) \approx G_1(f)$. In this case, a single measured CTF, affected by the IQ imbalances, can be modeled as

$$H_i'(f) = H_i(f) + k(f) \cdot H_i(-f), \tag{3.39}$$

where $i = 1, 2, \ldots, N$ denotes the ith measurement in the set of N measurements, $H_i'(f)$ is the complex baseband representation of the CTF, $H_i(f)$ is the complex baseband representation of the CTF without the effects caused by IQ imbalance and $k(f)$ is the complex frequency dependent IQ imbalance coefficient.

Please note that the described channel sounder system operates in the time domain, e.g. the result of the measurement is the CIR. However, it is easy to transform between the time and frequency domain representation utilizing the FFT and IFFT, e.g.

$$H_i(f) = \mathrm{FFT}\{h_i(t)\} \tag{3.40}$$

and

$$h_i(t) = \mathrm{IFFT}\{H_i(f)\}. \tag{3.41}$$

As can be observed from Eq. 3.39, the IQ imbalance causes self-interference, which can be, depending on the phase shift between the transmitter and receiver, constructive or destructive.

To illustrate the situation, consider this scenario: the transmitter is connected directly to the receiver by a coaxial cable and attenuator (back-to-back) and one of the LOs has a small frequency offset of $\Delta f \approx 100$ mHz. Several hundreds of CIRs are then taken at $f_{meas} \approx 10$ Hz. The resulting CIRs are depicted in Fig. 3.13.

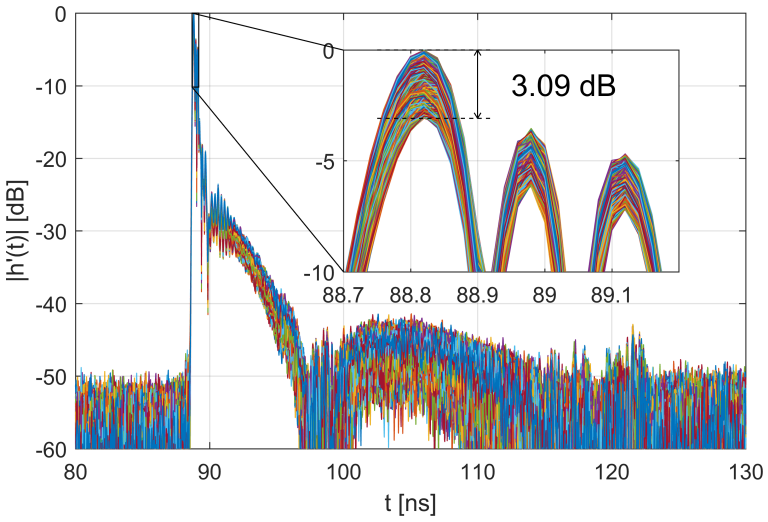

Fig. 3.13: Example of a back-to-back measurement without IQ imbalance correction.

As can be seen, there is one strong delayed path with decay, which corresponds to the behavior of a coaxial cable, however the amplitude of the strongest path varies by 3.09 dB within the observations, despite a completely static channel.

A trace of the strongest component of the CIR from Fig. 3.13, plotted in the complex plane, is depicted in Fig. 3.14, blue plot.

It can be clearly seen that the trace rotates around the origin according to the phase difference of the oscillators. However, it does not rotate around a perfect circle (green trace) but follows an elliptic curve, which is caused by the IQ imbalance. It also explains the amplitude fluctuation in Fig. 3.13 — ellipse does not have a constant distance from the origin, which is the amplitude of the component.

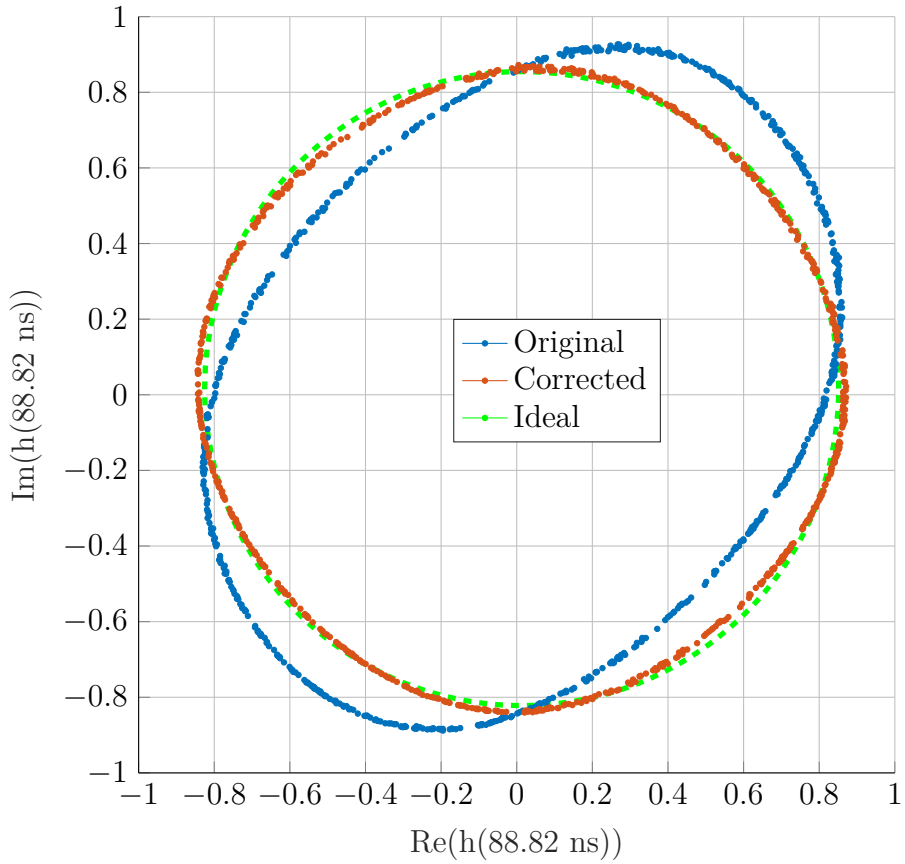

Fig. 3.14: Trace of the strongest component of the CIR in the complex plane. Blue: measured data, without IQ imbalance corrections, red: measured data, with IQ imbalance corrections, green: ideal (circle fit).

3.7.1 IQ imbalance compensation

According to Eq. 3.39, an estimate of the original CTF can be recovered by

$$\hat{H}_i(f) = H'_i(f) + k'(f) \cdot H'_i(-f), \tag{3.42}$$

where $k'(f)$ is the complex correction coefficient.

The dataset (transformed into the frequency domain), depicted in Fig. 3.13, can be considered as a calibration data in order to obtain the correction coefficients $k'(f)$ as

$$k'(f) = \arg\min_{k' \in \mathbb{C}} \sigma^2(|H'(f) + k'(f) \cdot H'(-f)|), \tag{3.43}$$

where $\sigma^2(x)$ stands for the variance of the vector x and $H'(f) = [H'_1(f)\ H'_2(f)\ \ldots\ H'_N(f)]^T$. Using Eq. 3.43 for every frequency bin f, such value of $k'(f)$ can be found that the resulting trace of $\hat{H}(f)$ in the complex plane fits a circle best in the least squares sense. The solution can be obtained iteratively by using MATLAB function FMINSEARCH.

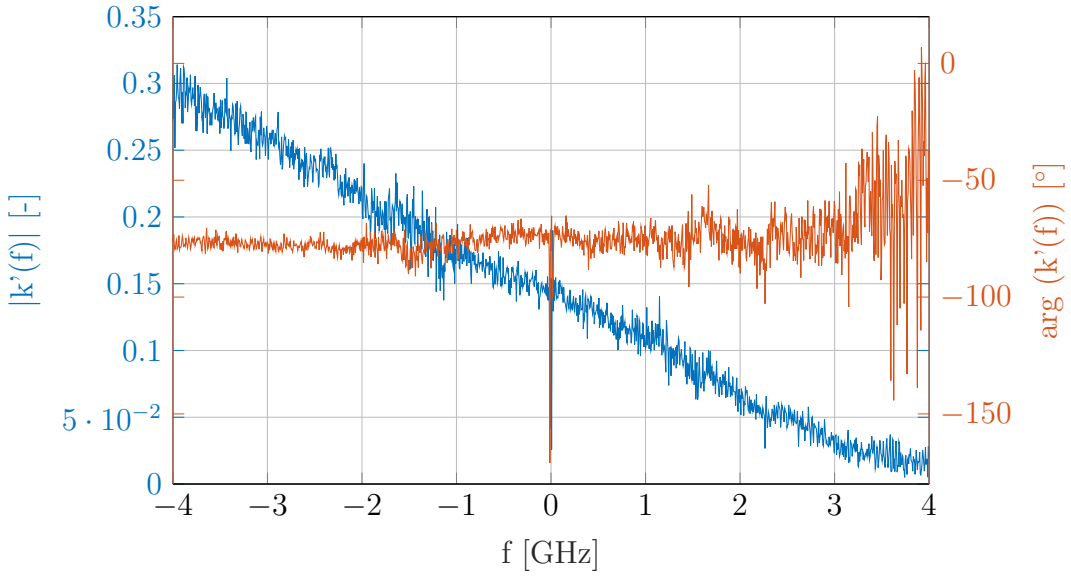

Fig. 3.15: Correction coefficient $k'(f)$, computed from data depicted in Fig. 3.13, in polar representation.

Correction coefficient $k'(f)$, computed from the data shown in Fig. 3.13, utilizing Eq. 3.43, is depicted in Fig. 3.15. It can be seen that the absolute maximal value is about 0.3 at low frequencies and then it tends to reduce for higher frequencies, while the argument is almost constant for the whole frequency range. Please note that the used up-down converters have DC-coupled inputs and outputs, so there is no relevant information at near zero frequencies, which causes the spikes around 0 Hz. Also, as the absolute value of the correction coefficient $k'(f)$ is almost zero at higher frequencies, its argument is getting noisy.

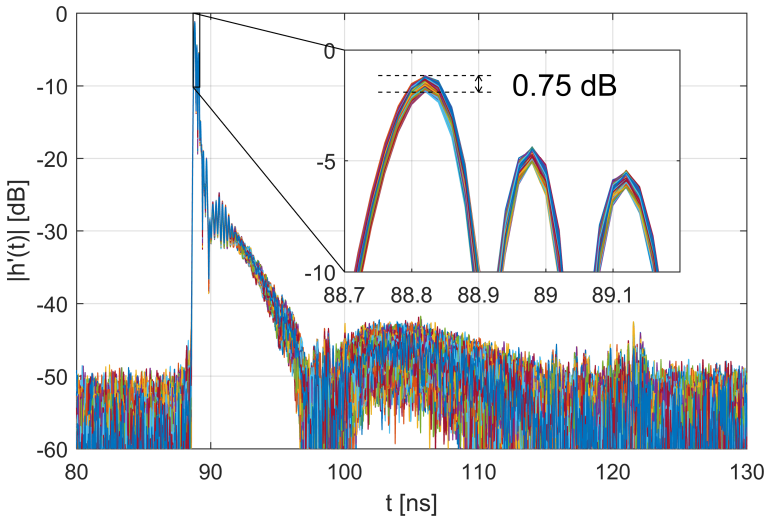

Fig. 3.16: Example of a back-to-back measurement with IQ imbalance correction.

Data from Fig. 3.13 with IQ imbalance corrections from Fig. 3.15 applied are depicted in Fig. 3.16. It can be seen that the amplitude fluctuation has reduced from 3.09 dB to 0.75 dB, e.g. by 2.34 dB. A trace of the strongest component of the IQ corrected CIR from Fig. 3.16, plotted in the complex plane, is depicted in Fig. 3.14, red plot. It can be seen that the shape approaches the ideal circle (green plot).

3.8 Conclusion

A millimeter wave band channel sounder operating in the time domain was presented in this chapter. A brief description of the instruments, principles and methods utilized in the system was given. The theoretical background when using the system in both linear and weakly non-linear environments and the data processing were described in detail. Several relevant properties of the m-sequences and Golay complementary sequences and their variations were discussed. Their performance in terms of SFDR was compared under various conditions. Broadband IQ imbalance compensation method was proposed and discussed.

4 TIME-DOMAIN NONSTATIONARY INTRA-CAR CHANNEL MEASUREMENT IN 60 GHZ BAND

This chapter is a postprint version of the following published paper:

A. Prokes, **J. Vychodil**, M. Pospisil, J. Blumenstein, T. Mikulasek, and A. Chandra, "Time-Domain Nonstationary Intra-Car Channel Measurement in 60 GHz Band," in *2016 International Conference on Advanced Technologies for Communications (ATC)*, 2016, pp. 1–6.

Author of this thesis contribution

This paper contains results from one of the first experiments with measurement setup described in Chapter 3. The measurements were done using m-sequences as a probing signal and basic setup with receiving and transmitting part at the same place, e.g. gating and timing was synchronized using physical connection. The author of this thesis developed the measurement system, helped with the realisation and conduction of the experiments and did basic data processing and contributed to the discussions about how to interpret measured data.

Time-Domain Nonstationary Intra-Car Channel Measurement in 60 GHz Band

Ales Prokes, Josef Vychodil, Martin Pospisil, Jiri Blumenstein, Tomas Mikulasek, Aniruddha Chandra
Department of Radio Electronics
Brno University of Technology
Brno, Czech Republic
prokes@feec.vutbr.cz

***Abstract*— The paper deals with a time varying intra-vehicle channel measurement in the 60 GHz millimeter wave (MMW) band using a unique time-domain channel sounder built from off-the-shelf components and standard measurement devices. The aim of the presented work is to describe the sounder architecture, the primary data processing technique, and preliminary results of measurements aimed at the effect of vehicle vibrations and twisting, and passengers moving in a car cabin. As the amplitude of the car cabin vibration and twisting had been supposed to be comparable with the MMW wavelength, some effect on the channel impulse response (CIR) and consequently on the delay-Doppler spread (DDS) was expected. Preliminary results confirm the correctness of this assumption and allow us to assess the effect of different above-mentioned phenomena. We tested the effect of driving the car on different types of road (bumpy road, flat road, highway, etc.). For comparison purposes we use DDS and statistics of CIR amplitudes calculated using the correlative technique applied to the pseudorandom binary sequence.**

Keywords—millimeter wave; channel measurement; channel sounder; channel impulse response; Doppler spread

I. INTRODUCTION

Recent societal trends show a continuously increasing demand for transport of people and goods. To make transport safer, more efficient, and cleaner, various traffic telematics services are currently under development. Besides the above requirements we have to consider the fact that traveling people spend a lot of time in public and private transportation. This time can be made more enjoyable by ensuring internet access or by installing some entertainment systems in vehicles. Hence in recent years there has been a growing demand for WPANs offering high data rates for short range intra-vehicle communication applications. Manufacturers of vehicles, aircraft, combat vehicles, etc. have a great interest in replacing wired communication links by wireless ones in order to save installation costs. These systems allow, for example, connecting the (rear) seat entertainment system without using cables, integrating the passenger mobile devices into the vehicle network or interconnecting a variety of car sensors with a central unit and actuators. There are many locations in the vehicle where the wired connection is impractical or even impossible (steering wheel, tires, and windshields). Moreover, as the number of intra-vehicle sensors and devices steadily increases, the wiring harness is becoming one of the heaviest components in a modern vehicle and as such is considered to have a significant impact on fuel consumption and ecology [1], [2].

There are several technologies such as Bluetooth or ZigBee available today that can be considered as candidates for intra-vehicle communication [2]. The Bluetooth provides sufficient bandwidth for multimedia but requires high transmitting power and connecting a large number of nodes is not straightforward. The ZigBee lacks throughput for multimedia applications and exhibits significant latency, which is unacceptable for certain intra vehicle scenarios. Due to the limitations of the above systems the other frequency bands such as ultra-wide band (UWB) defined by the IEEE 802.15.x recommendation (3.1 to 10.7 GHz) or millimeter wave (MMW) band (57 to 64 GHz) are being investigated for short-range communication purposes.

The intra-vehicle environment exhibits very specific propagation characteristics such as multipath propagation, shadowing, and non-stationary behavior. However, its investigation has been pursued predominantly for stationary case. Many works are based on the *frequency-domain* measurement using a vector network analyzer, which offers an excellent dynamic range (100–120 dB) but very long measurement times. With this approach, the complex transfer function (scattering parameter s_{21} referred to as the forward voltage gain) being measured is converted into a channel impulse response (CIR) using a windowed inverse fast Fourier transform. An averaged set of the squared CIRs then forms a power delay profile (PDP), which is the most frequently used characteristic for both small- and large-scale channel feature evaluation.

In [3] and [4] the UWB and the MMW intra-car channels are compared for different scenarios (different antenna configurations, empty and occupied car). The comparison is performed through the delay spread and the path-loss calculated from CIR or PDP. It is obvious that on the one hand the MMW band suffers from higher propagation and penetration losses (stronger shadowing effect) compared to the UWB but on the second hand the lower delay spread implies a lower complexity channel estimation and the usage of high-gain steerable antennas in a small physical form allows an easier MMW system implementation. The suitability of the MMW band for the intra-car communication based on signal- to-noise ratio (SNR) and interference evaluation is given in [5].

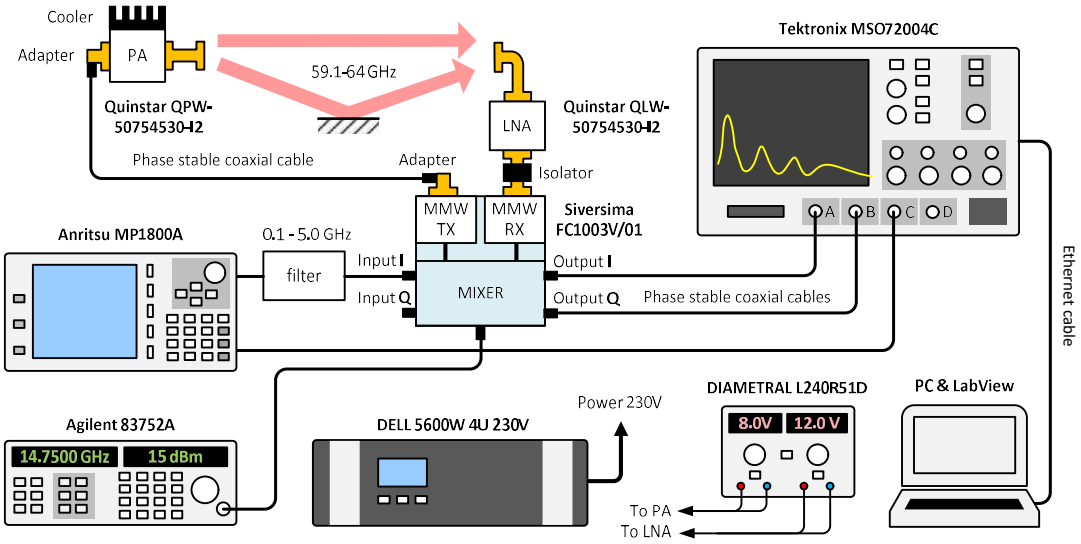

Fig. 1. Block diagram of time-domain channel sounder.

A *time-domain* intra-car channel measurement, which allows very fast measurement periods, but at the cost of low dynamic range (30 – 40 dB), has (according on our survey) been performed only for the UWB. Some experiments are performed via sounding the channel with narrow (picoseconds) Gaussian or common impulses. The CIR is then calculated from the received signal usually using the CLEAN deconvolution algorithm. While in [6] and [7] the authors deal with stationary channel characterization using the RMS delay spread, the cluster arrival rate, or the mean excess delay, in [8] a stochastic tapped delay line model for stationary but also for *moving* car scenario is created. Another time-domain measurement technique results from sounding the channel with a pseudo-random binary sequence (PRBS). A correlation principle used for the CIR calculation provides a relatively high correlation gain which is the biggest advantage over the narrow impulse channel sounding approach. The PRBS based channel sounder for multiple time-variant radio propagation channel measurement in different UWB bands and in the 59.5 – 66.5 GHz MMW band is introduced in [9]. It performs up to 100 measurements per second and offers 67 dB of instantaneous dynamic range and 7 GHz of bandwidth. Another UWB channel sounder using correlation technique can be found in [10]. However, intra-vehicle channel measurement using such a sounder has probably not been published yet.

The main contributions of the paper are

- introduction of a novel concept of time-domain PRBS based MMW channel sounder built from off-the-shelf components and standard measurement devices,
- presentation of original preliminary results of measurements aimed at the effect of vehicle vibrations and twisting due to driving the car on different types of roads, and passengers moving in the car cabin.

We analyzed the above effects through the *delay-Doppler spreading function* (DDSF) and through the statistical distribution of the CIR magnitudes.

The rest of the paper is organized as follows. Section 2 describes the measurement setup including the antenna radiation characteristic and the list of the fundamental parameters. Section 3 briefly informs about the techniques of signal processing used for both the CIR and the DDSF calculation. Then, in the most important section, Section 4, the DDSF evaluated for different scenarios and statistics of the CIR are given. A summary of the paper is given in the Conclusion.

II. Measurement Setup

The time-domain measurement testbed (see Fig. 1) is created using a Tektronix MSO72004C (20 GHz, 50 GS/s) Mixed Signal Oscilloscope, an Anritsu MP1800A Signal Quality Analyzer (working as a generator of PRBS), a SiversIma FC1003V/01 up/down converter changing the frequency from baseband to the MMW band in transmitter (TX) and back in receiver (RX), and an Agilent 83752A a frequency stable, low phase noise generator (carrier generator for up/down conversion). In order to compensate for large propagation loss in the MMW band the Quinstar QLW-50754530-I2 low noise amplifier and QPW-50662330-C1 power amplifier are used. To achieve good time synchronization between the MP1800A and MSO72004C both devices are supplied with a 10 MHz reference frequency generated by the oscilloscope. For the case of moving car channel measurement the sounder is placed in the car and supplied with uninterruptible power supply (DELL 5600W 4U 230V). The filter 0.1 – 5 GHz is optional and limits together with the internal up/down converter filter the frequency band of PRBS.

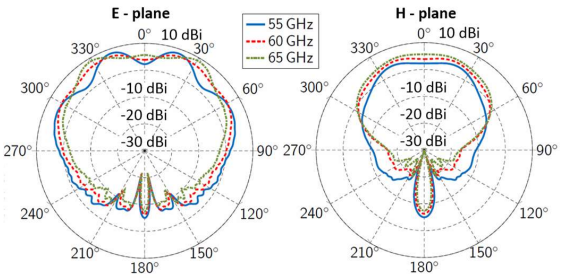

Fig. 2. Simulated radiation patterns of the open waveguide.

The operation of the testbed is straightforward. The seamless repeating PRBS of the length $N_{bit} = 2^k - 1$ bits, where k can in our system vary from 7 to 31, and data rate R_{PS} = 12.5 Gbit/s is frequency limited to the 0.1 – 5 GHz bandwidth, up-converted into the 59.1 – 64 GHz MMW band, and then fed to the power amplifier with a gain of 30 dB through a 2.5 m phase stable coaxial cable (Megaphase TM67-V1V1-138) with an attenuation of 26 dB. The MMW signal is irradiated and received using the open-ended waveguide antennas QuinStar QWS-V02000. The radiation pattern of the waveguide is shown in Fig. 2 [11]. It is obvious that radiation in the H-plane is more directional but due to the large propagation loss of the MMW signal the effect of indirect components is less important. However, for the first experiments such a solution is reasonable. The received signal then passes through the amplifier with a gain of 30 dB and a noise figure of 4.5 dB. The waveguide isolator prevents the receiver from oscillating. The quadrature down-conversion produces two baseband signals, I and Q, which are digitized and stored in the internal oscilloscope memory. Because the converter includes the frequency multiplier by a factor of 4, the generator output frequency is set to 14.75 GHz (see e.g. upper frequency calculation: 5 GHz + 4×14.75 GHz = 64 GHz).

The repeating PRBS is chosen as the excitation signal due to the very good circular correlation properties of selected PRBSs which invoke using a very convenient circular auto-correlation technique for the CIR calculation. The PRBS length then defines the maximum observable time span $T_{max} = N_{bit}/R_{PS}$. For the chosen k = 11 we get N_{bit} = 2047 and T_{max} = 163.8 ns. Assuming the speed of light c = 3×10^8 m/s we can obtain the maximum observable distance L_{max} = 49.13 m. Selected system parameters are summarized in Table 1.

In order to suppress the oscilloscope wideband noise, we use the 8 GHz user-selectable bandwidth limit filter. This option can only be used when the full maximum sampling rate R_S = 50 GS/s is chosen. Considering the memory depth of the oscilloscope M_D = 31.25 MSa per channel and the above mentioned time span T_{max} = 163.76 ns we can calculate important system parameters such as the maximum measurement rate (number of measurements per second), number of samples per CIR, number of saved CIRs, and total measurement time (see Table 1). Because the maximum measurement rate (e.g. 6.1×10^6 Meas/s for k = 11) is too high for our needs we insert between two consecutive CIR measurements the time delay T_D = 1 ms.

TABLE I. LIST OF SELECTED SYSTEM PARAMETERS

	Relation	k = 10	k = 11	k = 12
Number of PRBS bits [-]	$N_{bit} = 2^k - 1$	1023	2047	4095
Maximum observable time [ns]	$T_{max} = N_{bit}/R_{PS}$	81.84	163.76	327.60
Maximum observable distance [m]	$L_{max} = cT_{max}$	24.53	49.13	98.21
Max. measurement rate [Meas/s × 10^6]	$R_M = 1/T_{max}$	12.22	6.10	3.053
Number of samples per CIR [-]	$N_{CS} = N_{bit}R_S/R_{PS}$	4092	8188	16380
Number of saved CIRs [-]	$N_{CIR} = M_D/N_{CS}$	7636	3816	1907
Total measurement time [µs]	$T_M = N_{CIR}T_{max}$		624.8	
Correlation gain [dB]	$G_C = 20log(N_{bit})$	60.20	66.22	72.25

The time delay is controlled by the oscilloscope and precisely triggered by the signal quality analyzer. Such a sampling period allows us to analyze the Doppler spread up to approximately 500Hz from the 3816 CIR records corresponding to the 3.816 s time interval. For additional information about the channel sounder modified for the UWB see [12].

The installation of the test-bed in Skoda Octavia 1.9 TDI car is shown in Fig. 3. For all the measurements we placed the transmitting antenna behind the rear seats on the right side of the car while the receiving antenna was situated on the right side of the dash board (see Fig. 4). Both antennas were aligned to the center of the car cabin. The line-of-sight communication is blocked by the passenger siting on the front seat.

III. SIGNAL PROCESSING TECHNIQUES

As mentioned above the proposed channel sounder benefits from the correlation technique which increases significantly the dynamic range because the SNR of the receiver is improved by the correlation gain. Since the dynamic range of the MSO72004C oscilloscope is about 35 dB [13], the total dynamic range approaches 100 dB theoretical limit (for k = 11). Unfortunately, the CIR calculated using correlation of PRBS passing through a nonlinear system (represented in our case by amplifiers and mixers) exhibits plenty of spurs [14], which markedly decreases the dynamic range. This phenomenon that depends on the signal level and PRBS length and limits the dynamic range of the sounder to 30–50 dB is now intensively studied and suitable technique for the spurs mitigating is sought.

Fig. 3. Installation of the tesbed into car Skoda Octavia 1.9 TDI.

Fig. 4. Installation of the receiver (left) and transmitter (right).

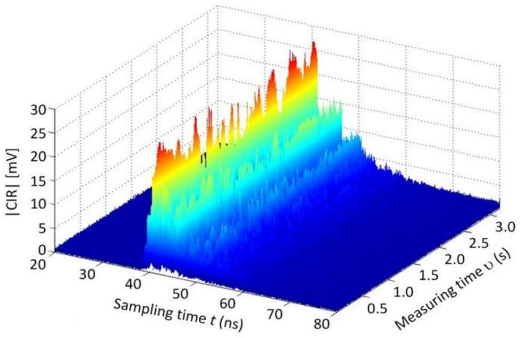

Fig. 5. Example of CIR magnitude for driving the car on a highway.

The channel is assumed to behave as a linear time invariant (LTI) system having an impulse response $h(t)$. To estimate $h(t)$ the cross correlation $R_{xy}(t)$ between the LTI system output and input may be employed in accordance with [15]

$$R_{xy}(\tau) = [h(t) * R_{xx}(t)](\tau), \tag{1}$$

where $R_{xx}(\tau)$ is the autocorrelation function of the input signal and $*$ denotes convolution. In order to obtain high correlation gain we employ m-sequences [16] which belong to the family of PRBS. The autocorrelation of the m-sequence is actually a sharp triangle function (note that the theoretical circular autocorrelation of an m-sequence is a Kronecker delta function), however, for our purpose we can write $R_{xx}(\tau) \approx p_s\delta(\tau)$, where p_s is a constant related to a signal power and $\delta(\tau)$ is the Dirac pulse. Thus, the cross correlation function is equal to the system impulse response as follows

$$R_{xy}(\tau) = [h(t) * p_s\delta(t)](\tau) = p_s h(\tau). \tag{2}$$

The cross correlation $R_{xy}(t)$ can be calculated using convolution. For this purpose let $s_m(t)$ denotes the periodical excitation PRBS signal (LTI system input) and $r(t)$ denotes the received signal (LTI system output). Then under simplifying condition $p_s = 1$ and considering the relation between correlation and convolution [15] the CIR can be expressed as

$$h(t) = corr[r(t), s_m(t)] = r(t) * s_m^*(-t). \tag{3}$$

To accelerate the CIR calculation, equation (3) is transformed to the frequency domain and back using the complex fast (inverse) Fourier transform ((I)FFT)

$$h(t) = IFFT\{FFT[r(t)] \times FFT[s_m^*(-t)]\}. \tag{4}$$

An appropriate metric for the assessment of the car vibrations and passenger movements is the delay-Doppler spreading function [17]. The CIR calculation (4) corresponds to a single measurement. As mentioned above we measured set of N_{CIR} responses in regular 1 ms intervals. Let us designate this time by the letter ϑ. Then we have to distinguish the *sampling time* (oscilloscope recording time) t from the *measuring time* (time of regular CIR measurements) ϑ, as shown in Fig. 5, and write the CIR as a two dimensional function $h(t, \vartheta)$. The DDSF can then be written in the form

$$S(t, f_D) = \int_{-\infty}^{\infty} h(t, \vartheta)\, e^{-i2\pi f_D \vartheta} d\vartheta, \tag{5}$$

where f_D is the Doppler frequency and $h(t, \vartheta)$ can be expressed as a sum of P multipath components (paths) at any time ϑ, i.e.

$$h(t, \vartheta) = \sum_{p=1}^{P(\vartheta)} a_p(\vartheta)\, e^{-i2\pi f_{D,p}(\vartheta)} \delta[t - t_p(\vartheta)], \tag{6}$$

where α_p is the complex attenuation factor, $f_{D,p}$ is the Doppler shift, and t_p is the time delay associated with the p-th path. In reality we calculate the DDSFs applying FFT to the measured series where t is constant and ϑ varies from 0 to $N_{CIR}T_D$. For this purpose we select only the cases where the CIR exceeds the noise (e.g. for $t \in \langle 40\ ns, 50\ ns \rangle$ as is obvious from Fig. 4) and in the following step we average them. Considering the fact, that both the times t and ϑ are discrete ($t = n/R_S$ and $\vartheta = kT_D$, where n and k are integers), the average DDSF can be expressed in the form

$$S(f_D) = \frac{1}{n_2 - n_1} \sum_{n=n_1}^{n_2} S(n/R_s, f_D), \tag{7}$$

where n_1 is the sample ordinal number calculated as a median of the ordinal numbers of all the measured CIR maxima in a single record, and n_2 corresponds to the coordinate of the maximum excess delay value.

Other metrics used to evaluate the time variant behavior of the channel are the probability distribution function (PDF) and the cumulative distribution function (CDF) of the CIR for constant sampling time t.

IV. Results

First we carried out a few reference measurements inside an empty car parked in an underground garage. The measurement devices were placed outside the car. We investigated the effects of running engine at different *revolutions per minute* (rpm) and the effects of a very loudly playing built-in audio system on the car cabin vibrations. Then we installed the test bed into the car as shown in Figs 3 and 4 and conducted a set of 120 measurements for the car traveling over different types of road (flat road, cobblestone road, bumpy road with potholes, old and new highways, etc.) at different speeds. The car was occupied by a driver, a front passenger, and a passenger sitting behind the driver (controlling the test-bed).

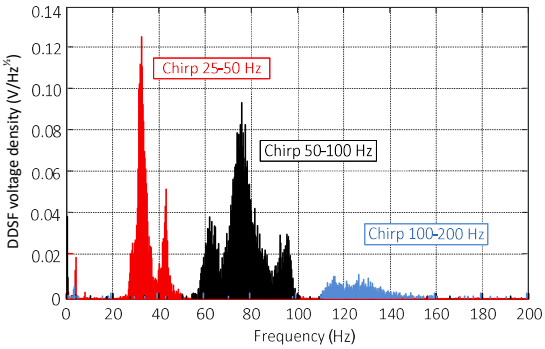

Fig. 6. Comparison of the DDSF magnitudes for different chirps.

A. *Delay Doppler spread*

For the reference measurements we prepared a set of MP3 sound files (chirps and pure sine waves) at frequencies between 20 Hz and 400 Hz. We also tested the influence of different antenna locations. The DDSF for three different chirps (harmonic signal swept from lower to upper frequency) is shown in Fig. 6. It is evident that the effect of the lower frequencies is more marked than the effect of the upper ones. There are also some local minima and maxima caused probably by mechanical resonances of particular objects in the car cabin and possibly also by mechanical resonances of the transmitting or receiving antennas. Frequencies above 150 Hz have almost no influence on the channel. Note that the voltage density drop in dependence on frequency is influenced probably also by the acoustic pressure, generated by speakers, which is higher at the lower frequencies.

The effect of the running engine is very similar. It can be observed dominantly at low rpm as is obvious from Fig. 7. Note that the four-stroke engine running at 800 rpm produces 1600 ignitions per minute which corresponds to 13.3 revolutions and 26.6 ignitions per second. It is obvious that the effect of the car body vibration is minimal at the engine rpm corresponding to common ride, which testifies to the good damping of engine-induced vibrations in recent cars.

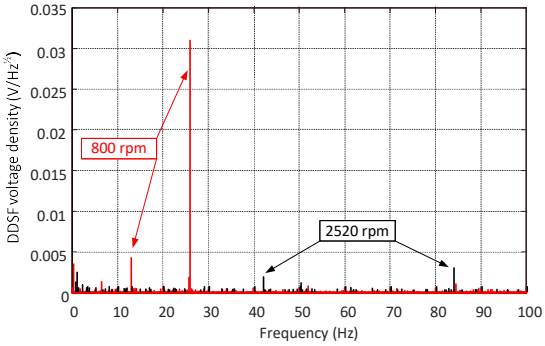

Fig. 7. Effect of running engine at different rpm on the DDSF magnitude.

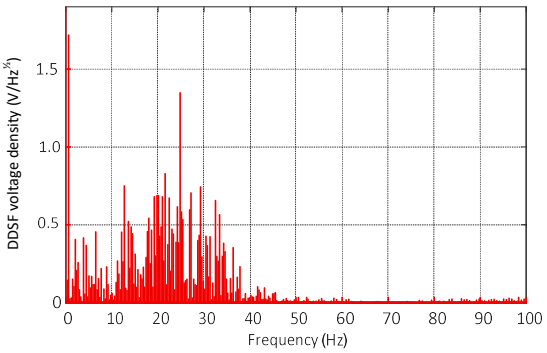

Fig. 8. Effect of passengers moving quickly their hands and bodies.

An interesting result was obtained when the passengers were moving their hands and bodies inside the stationary (parked) car. As is obvious from Fig. 8 up to 45 Hz there are significant components in the spectrum. This phenomenon was taken into account during the measurements in the moving car. The passengers tried to remain as motionless as possible, which was very difficult particularly for the driver and the person controlling the test-bed.

In the next step we evaluated all the measurements carried out in the moving car and compared the DDSFs. The results are ambiguous. The same scenario (the same road and speed) can produce very different results. It is probably caused by unintentional passenger movements. Due to the large amount of measurements we can exclude such anomalous results and state typical representatives for particular situations. An example of DDSF representatives for two different roads is shown in Fig. 9. It is obvious that the bumpy road causes more DDSF spectral components. It is also evident that the magnitude of DDSF in Figs. 8 and 9 is much larger than the magnitude in Figs. 6 and 7. Hence the effect of the running engine on the moving car DDSF is negligible. For completeness let us mention that the influence of the surrounding environment (other vehicles) was not proved.

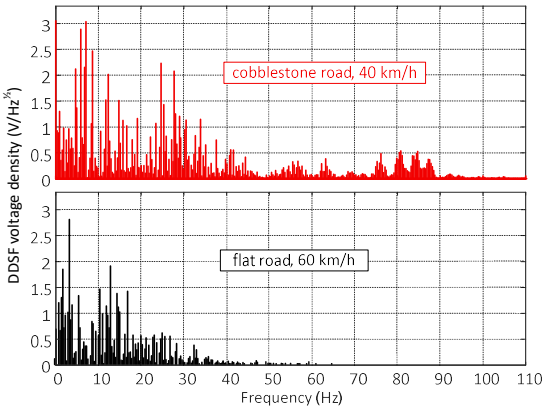

Fig. 9. DDSF magnitude calculated for the two different road surfaces.

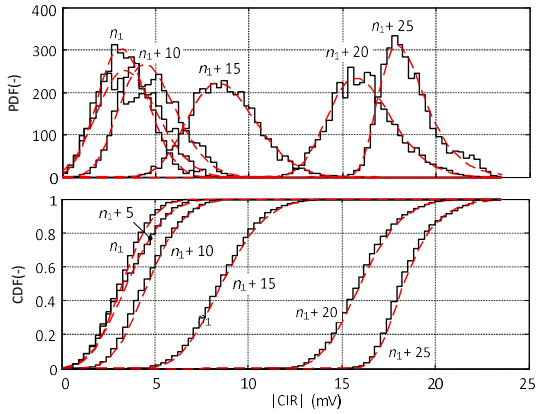

Fig. 10. The PDF and the CDF of the CIR magnitude (stair plot) and their fitting using GEV distribution (dashed line).

B. *Probability density and cumulative density functions*

To create a stistical channel model in the time-domain it is nesesary to know the amplitude distribution of $h(t, \vartheta)$. We tried to find the best fit between all the measured data and a variety of probability distributions. The best fit was obtained using the *generalized extreme value* (GEV) distribution. It is defined by the location parameter μ, the scale parameter $\sigma > 0$, and the shape parameter ξ [18]. Examples of the PDF and the CDF of the CIR magnitude and their fitting using the GEV distribution for the case of bumpy road are shown in Fig 10. The plots are depicted for the CIR coordinates $n = tR_S = n_1 + 5i$, where n_1 is defined in Section III and i = 0,1,2… For all the CIRs we obtained the following limits $\mu \in \langle 0.001, 0.03 \rangle, \sigma \in \langle 0.0005, 0.004 \rangle$, and $\xi \in \langle -0.4, 0.1 \rangle$.

V. Conclusion

We propose a channel sounder realized without the need for designing and manufacturing any electronic circuits or equipment. It consists of standard measurement devices and common microwave components, and offers very good properties such as 5 GHz bandwidth, up to several millions measurements per second, up to a few seconds record length (we plan to extend it), and a satisfactory dynamic range.

By analysing the measured data we discovered that the effects of a running engine or a loudly playing built-in audio system are negligible when compared with the influence of car body vibration or twisting caused by the car motion. Of considerable effect on the channel time variance (expressed e.g. by the DDSF) are the movements of passengers in the car-cabin, which, among other things, are also caused by driving the car on a bumpy road or negotiating a curve, or by accelerating or braking. Unintentional passenger movement probably causes certain randomnes in the data measured, and some records have to be discarded when other effects such as car speed or road quality are evaluated. The CIR probability distribution in measurement time can be obtained satisfactorily using the GEV distribution. Note that here unpublished analyses of the CIR in *sampling time* can be found in many other works [3] - [7].

Acknowledgment

The research described in this paper was financed by the Czech Science Foundation, Project No. 13-38735S, by the SoMoPro II programme, Project No. 3SGA5720 Localization via UWB, co-financed by the People Programme (Marie Curie action) of the Seventh Framework Programme (FP7) of EU according to the REA Grant Agreement No. 291782 and by the South-Moravian Region, and by National Sustainability Program under grant LO1401. For the research, the infrastructure of the SIX Center was used.

References

[1] G. Leen and D. Heffernan, "Expanding automotive electronic systems," *Computer*, vol. 35, no. 1, pp. 88–93, Jan. 2002.

[2] N. Lu, N. Cheng, N. Zhang, X. Shen, J.W. Mark: "Connected Vehicles: Solutions and Challenges," *IEEE Internet Things J*, vol. 1, no 4, pp. 289–299, Aug. 2014.

[3] M. Schack, M. Jacob, and T. Kurner, "Comparison of in-car UWB and 60 GHz channel measurements," in *Proc. IEEE EuCAP*, Barcelona, Spain, Apr. 2010, pp. 1–5.

[4] J. Blumenstein, T. Mikulasek, A. Prokes, T. Zemen, and C. Mecklenbrauker, "Intra-vehicular path loss comparison of UWB channel for 3-11 GHz and 55-65 GHz," in *Proc. IEEE ICUWB*, Montreal, Canada, Oct. 2015, pp. 1–4

[5] M. Peter, R. Felbecker, W. Keusgen and J. Hillebrand, "Measurement-Based Investigation of 60 GHz Broadband Transmission for Wireless In-Car Communication," in *Proc. IEEE VTC Fall*, Anchorage, AK, USA, Sep. 2009, pp. 1–5.

[6] W. Niu, J. Li and T. Talty, "Intra-Vehicle UWB Channel Measurements and Statistical Analysis," in *Proc. IEEE GLOBECOM*, New Orleans, LO, USA, Dec. 2008, pp. 1–5.

[7] A. Chandra, J. Blumenstein, T. Mikulášek, J. Vychodil, R. Maršálek, A. Prokeš, T. Zemen, C. A. Mecklenbräuker, "Serial subtractive deconvolution algorithms for time-domain ultra wide band in-vehicle channel sounding," *IET Intel Transport Syst*, vol. 9, no. 9, pp. 870–880, Nov. 2015.

[8] W. Niu, J. Li and T. Talty, "Intra-vehicle UWB channels in moving and stationary scenarios," in *Proc. IEEE MILCOM*, Boston, MA, USA, Oct. 2009, pp. 1–6.

[9] R. Zetik, M. Kmec, J. Sachs, and R. S. Thomä, "Real-Time MIMO Channel Sounder for Emulation of Distributed Ultrawideband Systems," *Int. J. Antennas Propag*., vol. 2014, Article ID 317683, pp. 1–16, 2014.

[10] A. Dezfooliyan, A. M. Weiner, "Evaluation of Time Domain Propagation Measurements of UWB Systems Using Spread Spectrum Channel Sounding," *IEEE Trans. Antennas Propag*., vol. 60, no. 10, pp. 4855–4865, Oct. 2012.

[11] T. Mikulasek, J. Blumenstein, and A. Prokes, "Antennas utilized for intra-vehicle 3-11 GHz and 55-65 GHz channel measurement," in *Proc. PIERS*, Shanghai, China, Aug. 2016, pp. 1–5.

[12] J. Vychodil, A. Chandra, T. Mikulasek, A. Prokes and V. Derbek, "UWB time domain channel sounder," in *Proc. Radioelektronika*, Pardubice, Apr. 2015, pp. 268–271.

[13] MSO/DPO70000 Series Digital and Mixed Signal Oscilloscopes Datasheet, Available at http://www.tek.com/datasheet/mso-dpo70000-series-digital-and-mixed-signal-oscilloscopes-datasheet. 2016.

[14] S. A. Billings , S. Y. Fakhouri, "Identification of non-linear systems using correlation analysis and pseudorandom inputs," *Int. J. Syst. Sci*., vol. 11, no. 3, pp. 261–279, 1980.

[15] R. J. Polge and E. M. Mitchell, "Impulse Response Determination by Cross Correlation," *IEEE Trans. Aerosp. Electron. Syst.,* vol. AES-6, no. 1, pp. 91–97, Jan. 1970.

[16] S. W. Golomb et al., *Shift register sequences*. Aegean Park Press, 1982.

[17] F. Hlawatsch and G. Matz, *Wireless communications over rapidly timevarying channels*. Academic Press, 2011.

[18] S Kotz, S Nadarajah, *Extreme Value Distributions*, World Scientific, Washington, D.C, 2000.

5 EFFECTS OF VEHICLE VIBRATIONS ON MM-WAVE CHANNEL: DOPPLER SPREAD AND CORRELATIVE CHANNEL SOUNDING

This chapter is a postprint version of the following published paper:

J. Blumenstein, **J. Vychodil**, M. Pospisil, T. Mikulasek, and A. Prokes, "Effects of Vehicle Vibrations on mm-Wave Channel: Doppler Spread and Correlative Channel Sounding," in *2016 IEEE 27th Annual International Symposium on Personal, Indoor, and Mobile Radio Communications (PIMRC)*, 2016, pp. 1–5.

Author of this thesis contribution

This paper is an another interpretation of the data captured in the measuring campaign described in the previous chapter. The contributions of this thesis author are also similar: he developed the measurement system, helped with the realisation and conduction of the experiments and did basic data processing.

Effects of Vehicle Vibrations on mm-Wave Channel: Doppler Spread and Correlative Channel Sounding

Jiri Blumenstein, Josef Vychodil, Martin Pospisil, Tomas Mikulasek, Ales Prokes,
The Faculty of Electrical Engineering and Communication
Brno University of Technology, Czech Republic
email: blumenstein@feec.vutbr.cz, web: http://www.radio.feec.vutbr.cz/GACR-13-38735S/

***Abstract*—This paper deals with evaluating the effect of vehicle vibrations on the mm-wave intra-vehicular channel. As some of the vehicles' vibration amplitude may reach the order of millimeters, i.e., the amplitude is comparable with the mm-wave wavelength (≈5 mm), it can produce severe Doppler spreads.**

This paper evaluates Doppler spreads utilizing a mm-wave time-domain correlative channel sounder built into a vehicle which has been driven at different speeds on a variety of roads with a broad spectrum of surface quality.

I. Introduction

The aging population, densification of current traffic and the fundamental demand for safe and reliable transportation has prepared an interesting market opportunity for automated vehicles [1], [2]. It has, however, been recently recognized that the attempts of bringing at least some of the desired functionalities of the smart/automated driving in the form of vehicle-to-vehicle (V2V) communication based on IEEE 802.11p are not quite satisfactory, namely due to the bandwidth and physical layer constraints [3].

The authors in [4] state that the only viable solution for high bandwidth connected vehicles is the millimetric (mm-wave) band. The mm-wave band is usually understood to occupy the frequency range from 55 GHz to 65 GHz. This band provides around 10 GHz of unlicensed bandwidth (depending on the local spectrum management authorities), but it also suffers from high path-loss due to atmospheric absorption. On the other hand, the mm-band enables the usage of high-gain steerable antennas in a small physical form allowing for beamforming, beamsteering or spatial multiplexing [5], [6].

In the field of intra-vehicular channel characterization, there is a number of publications dealing with comparing different frequency bands [7], providing mm-wave channel models and spatial maps [8], [9] or channel stationarity [10]. Not only the passenger compartment is measured, but also for example the engine bay [11]. Also, the frequency domain channel sounding, which has been used in all mentioned publications, is discussed in detail in [12].

One of the rarely addressed issues of the vehicular high bandwidth communication in the mm-wave band is the effect of vibrations. Vibrations are caused by many reasons, for example, bad road conditions with potholes can cause car body relative movements and twisting. Also, the engine produces a variety of vibrations depending on many variables such as its revolutions per minute, temperature et cetera. On top of that, the vehicle's sound system is also recognized as a source of vibrations.

Now, the typical wavelength of the mm-wave band is around 5 mm and since the amplitude of the vibrations could be in millimeters [13], the Doppler spread caused by this movement could significantly impair any communication system operating in the said conditions.

This paper deals with the characterization of the intra-vehicular radio propagation (i.e., channel characterization) in the frequency range of 55-65 GHz.

A. Contribution of the paper

- The main objective is to evaluate the Doppler spread caused by the vibrations of the vehicle when in operation. The operating conditions are characterized by the vehicle velocity and a subjective index of the road condition.
- The channel impulse response (CIR) characterization in terms of delay spread and exponentially decaying model parametrization.
- We present a mm-wave correlative time-domain channel sounder built from off-the-shelf parts and measurement devices.

II. Correlative channel sounding

This section is divided into three subsections. First, we briefly state the time-variant channel parameters, then the theoretical principle of the correlative time-domain channel sounding and finally we provide a specific measurement setup description including a block scheme of the in-house built channel sounder (Fig. 1).

A. Time-variant channel parameters

The impulse response of a linear time-variant channel with P propagation paths is written as [14]:

$$h(t,\tau) = \sum_{p=1}^{P(t)} \alpha_p(t) e^{j2\pi f_{\mathrm{D},p} t} \delta\left(\tau - \tau_p(t)\right), \qquad (1)$$

where $f_{\mathrm{D},p}$ is the Doppler shift, $\alpha_p(t)$ is the complex attenuation and $\tau_p(t)$ is the time delay associated with the p-th path. Next, in order to characterize the time-frequency dispersion of the channel, authors in [15] defined a useful metric, namely the *delay-Doppler spreading function*, written as:

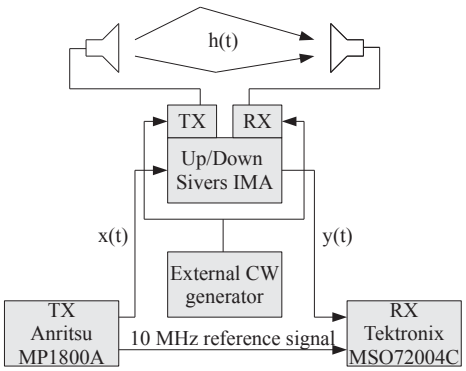

Fig. 1: Block scheme of the time-domain correlative channel sounder based on a m-sequence generator, a matched receiver, an up/down converter and a stable external RF source.

$$S(\tau, f_{\mathrm{D}}) = \int_{-\infty}^{\infty} h(t,\tau) e^{-j2\pi f_{\mathrm{D}} t} dt. \tag{2}$$

While sacrificing the possibility of observing the Doppler effects development in the delay domain, by averaging the delay-Doppler spreading function over the delays, we significantly improve the signal to noise ratio (SNR). Thus, the vibration effect becomes more evident. The averaging is done according to:

$$\bar{S}(f_{\mathrm{D}}) = \frac{1}{\tau_{\mathrm{m}}} \sum_{\tau}^{\tau_{\mathrm{m}}} S(\tau, f_{\mathrm{D}}), \tag{3}$$

where τ_{m} is the maximal excess delay. We denote $\bar{S}(f_{\mathrm{D}})$ as the Doppler spectrum.

The delay-Doppler spreading function allows us to observe the Doppler spread which is caused not only by the vibrations of the vehicle, but also by other moving objects inside the car. Let us point out that the attenuation of the car body and windows is in the order of tens of decibels and the dynamic range of the channel sounder is rather limited, so we do not consider reflectors or scattered objects outside the car to introduce any resolvable effects in the obtained data.

B. Theoretical principle of the correlative channel sounder

Apart from other possible solutions of the time-domain channel sounding (e.g., listed in [14]), we employ a method which utilizes an m-sequence [16] which relates to the family of pseudo-noise sequences. The autocorrelation of the m-sequence designated as R_{xx} is in fact a sharp triangle function, however, for our purpose we can write $R_{xx} \approx \delta(\tau)$.

Now, let us consider a simple input-output relation:

$$y(t) = h(t) \otimes x(t), \tag{4}$$

where $y(t)$ is the signal captured by the channel sounder, $h(t)$ is the CIR, $x(t)$ stands for the transmitted m-sequence and finally $\otimes$ represents the convolution.

Applying the fact that the index of the transmitted m-sequence is known to the receiver, the receiver is able to estimate the CIR from the cross-correlation of the transmitted and received signals $x(t)$ and $y(t)$ respectively because it holds that:

$$R_{xy}(\tau) = \mathbb{E}\left[x^*(t) y(t)\right] = h(t) \otimes R_{xx}(\tau) \approx$$
$$\approx h(t) \otimes \delta(\tau) = h(t). \tag{5}$$

In order to avoid systematic measurement errors and to be able to accept the approximate relation (5), the channel sounder as well as the sounding environment shall fulfill the conditions listed in [17].

C. Measurement setup

1) Measurement site description: During the measurement campaign, we have utilized a typical European passenger vehicle, Skoda Octavia 2, equipped with a two-liter diesel engine. The photographs from the measurement campaign are in Figure 3.

The presented measurement campaign consists of numerous channel measurements performed inside the car, while the car was in motion. For each channel snapshot, we have recorded the actual speed. Moreover, utilizing a subjective three-step metric, the quality of the road was assessed by the driver of the vehicle (i.e., for each channel measurement, we have an index evaluating the "bumpiness" of the actual road).

2) Antennas: The WR15 open-ended waveguide antennas were used at both the RX and TX side with radiation patterns depicted in Figure 2. While the TX antenna and the power amplifier (PA) were mounted on the side-window next to the rear passenger on the right hand side (see Fig. 3b), the RX antenna, the up/down converter and the low-noise amplifier (LNA) were mounted approximately in the middle of the dashboard (see Fig. 3c). The antennas were fastened utilizing suction caps.

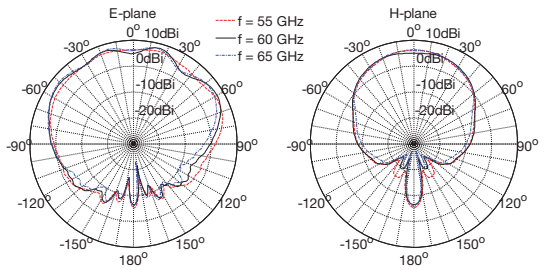

Fig. 2: Measured gain pattern of the open-ended waveguide in the E–plane and the H–plane for 55-65 GHz.

3) Measurement devices: The block scheme of the in-house built channel sounder composed of the off-the-shelf components is visible in Figure 1.

The measurement setup consisted of the Anritsu Signal Quality Analyzer MP1800A for generating the m-sequences with data rate 12.5 Gbit/s and 13 dBm output power. The

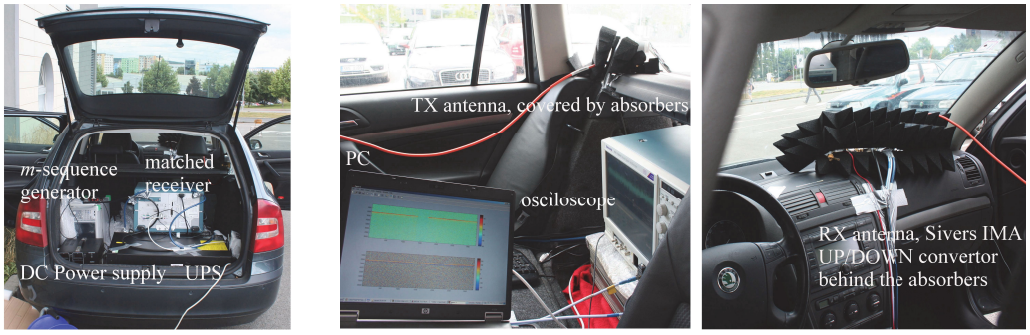

(a) The trunk of the vehicle used for the measurement campaign with UPS ensuring circa 1 hour of operation and DC power supply for LNA and PA.

(b) View from the back seat. The TX antenna is mounted using a suction cap on the side window. The PA and the TX antenna are covered by absorbers.

(c) The view from the drivers seat. Behind the absorbers on the dashboard is the RX part with both the up/down converter and the LNA.

Fig. 3: Photographs taken during the measurement campaign.

oscilloscope Tektronix MSO72004C was used as the matched receiver with 16 GHz bandwidth and 50 GS/s sampling frequency. The dynamic range was extended with the low-noise and power amplifiers QuinStar QLW-50754530-I2 and QPW-50662330 respectively. We also utilized the Sivers IMA FC1003V/01 up and down converter to shift the signal to the band of interest 55 - 65 GHz.

4) Real-time data processing: The length of the m-sequences was determined by the relation $N = 2^k - 1$, where N is the m-sequence length and k is the order of the m-sequence. Through this work, we chose $k = 11$, thus $N = 2047$.

Now, considering that the internal memory of the oscilloscope is 31.25 MS and employing 50 GS/s sampling frequency, we were able to capture 0.625 ms of the transmitted signal into the fast internal memory of the oscilloscope (this represents more than 3000 CIRs snapshot for one measurement). Between each channel snapshot, there is a 1 ms pause. Then, data was uploaded to a PC for post-processing and further measurements could be performed.

III. Results

This sections provides the post-processing results of the measured data from the obtained CIRs as well as the evaluated Doppler spreads.

A. Doppler spread

As depicted in the cutout in Figure 4, the Doppler spread was determined as the spread of the main peak of the Doppler spectra $\bar{S}(f_\mathrm{D})$ exactly 1 dB above the noise floor. The noise floor has been determined as the mean value of $\bar{S}(f_\mathrm{D})$ while not taking into account the vicinity of $\bar{S}(0)$.

An important thing to point out is that we have also performed calibration measurements in a laboratory without the presence of any known vibrations. The result of this measurement is depicted in Fig. 4 in red color. This was done mainly in order to identify possible impairments of the channel sounder. It is visible, that spurious signals are 30 dB weaker compared to the main peak around $\bar{S}(0)$. Moreover, all datasets have been visually inspected such that no spurious signals could affect the results.

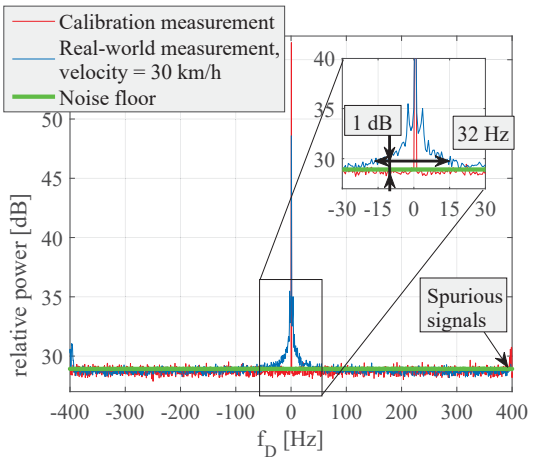

Fig. 4: Comparison of two Doppler spectra. One is estimated while the vehicle was in motion (30 km/h) and the second is from the calibration measurement performed in a laboratory (without vibrations). The cutout on the upper right corner demonstrates how we evaluated the Doppler spread (in this case 32 Hz).

In Figure 5 we plot the estimated Doppler spread as the function of the vehicle speed. We also distinguish between the road quality, which has been evaluated via a subjective three-step index (a smooth road, a semi-smooth road and a bumpy road). The road quality was assessed by the driver of the vehicle.

As is seen in Figure 5, on the roads with the worst quality, we have reached only limited speeds between 15-50 km/h. The estimated Doppler spread on the worst roads exhibits a mean value of 37 Hz.

On the semi-smooth roads, with speeds from 80 km/h to 160 km/h, we have recorded a mean Doppler spread of 38.6 Hz and on the smooth roads with the same speeds, the mean Doppler spread is 37.7 Hz. Please note, that in Figure 5, there is plotted a mean Doppler spread for all speeds and road quality indexes together with its standard deviation 12 dB.

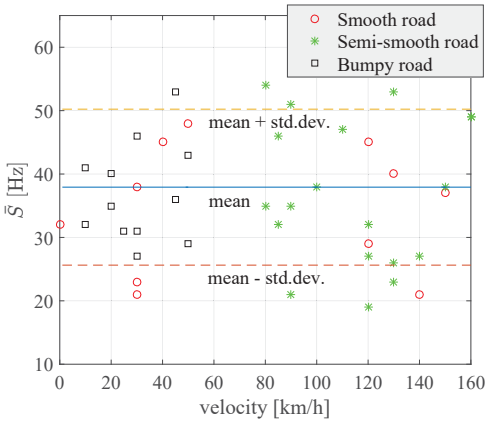

Fig. 5: Comparison of the Doppler spread for various road conditions and velocities. The mean and the standard deviation of the Doppler spread are depicted.

B. Delay domain

As an example, in Figure 6 we plot 100 CIRs recorded during a ride at 30 km/h on a bumpy road. The maximal excess delay across all the captured CIRs is around 1 ns. In literature (e.g., [8]), there are higher values reported, but this is due to the limited dynamic range of the time-domain sounder. Frequency domain channel sounders usually provide notably higher dynamic range, but they can not capture fast channel variations. The measured CIRs are parametrized by the exponentially decaying model as:

$$h(\tau) = \exp\left(\frac{-\tau}{0.37 \text{ ns}}\right) \tag{6}$$

In Figure 1 we also plot a mean CIR (black curve) calculated as the average of the 100 CIRs plotted in gray. In the mean CIR, one can observe several (four or five) multi-path component (MPC) clusters.

IV. Conclusion

Although the vibrations caused by this specific vehicle or its engine may differ from other vehicles on the market, we believe that this evaluation provides reasonable insight on the values of the achieved Doppler spreads occurring in a typical in-vehicle environment. We have captured around 30 recordings of the CIRs in a variety of road conditions and speeds (each consisting of more than 3000 individual CIR snapshots).

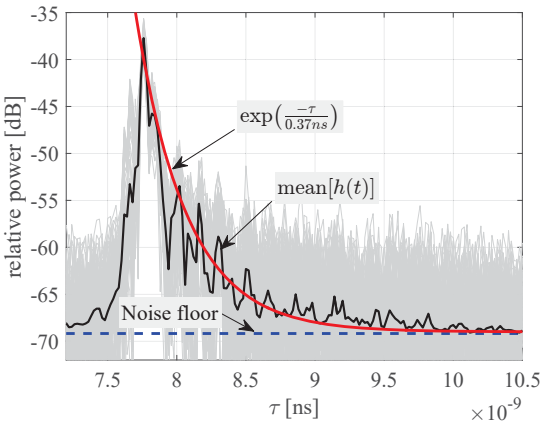

Fig. 6: Example of the measured data. There are 100 measured CIRs depicted in gray. This measurement was performed at 30 km/h on a bumpy road. The decay of the resolvable MPCs clusters is modeled by an exponentially decaying process.

We compare the vibration-free calibration measurement with the measurement of the vehicle in operation. The estimated mean Doppler spread reaches up to 38 Hz. On the other hand, it is evident that neither the vehicle speed nor conditions of the road has a significant effect on the Doppler spread of the mm-wave in-vehicle channel.

In the delay domain, we have characterized the obtained CIRs by the exponential decay process. Although the dynamic range of the correlative channel sounders is rather limited (compared to the frequency domain method), we see approximately four resolvable clusters of the MPCs.

To enhance the reproducibility of our research, we provide representative datasets from our measurement for free on our web pages: http://www.radio.feec.vutbr.cz/GACR-13-38735S/

Acknowledgment

This work was supported by the Czech Science Foundation project No. 13- 38735S Research into wireless channels for intra-vehicle communication and positioning and was performed in laboratories supported by the SIX project, No. CZ.1.05/2.1.00/03.0072, the operational program Research and Development for Innovation.

References

[1] C. Sommer and F. Dressler, *Vehicular Networking*. Cambridge University Press, 2014.

[2] N. Lu, N. Cheng, N. Zhang, X. Shen, and J. Mark, "Connected vehicles: Solutions and challenges," *IEEE Journal Internet of Things*, vol. 1, no. 4, pp. 289–299, Aug 2014.

[3] Z. Xu, L. Bernad, M. Gan, M. Hofer, T. Abbas, V. Shivaldova, K. Mahler, D. Smely, and T. Zemen, "Relaying for IEEE 802.11p at road intersection using a vehicular non-stationary channel model," in *2014 IEEE 6th International Symposium on Wireless Vehicular Communications*, 2014.

[4] J. Choi, N. G. Prelcic, R. C. Daniels, C. R. Bhat, and R. W. Heath, "Millimeter wave vehicular communication to support massive automotive sensing," 2016. [Online]. Available: http://arxiv.org/abs/1602.06456

[5] E. Ben-Dor, T. Rappaport, Y. Qiao, and S. Lauffenburger, "Millimeter-wave 60 GHz outdoor and vehicle AOA propagation measurements using a broadband channel sounder," in *IEEE Global Telecommunications Conference*, Dec 2011.

[6] T. Rappaport, J. Murdock, and F. Gutierrez, "State of the art in 60-GHz integrated circuits and systems for wireless communications," *Proceedings of the IEEE*, vol. 99, no. 8, pp. 1390–1436, Aug 2011.

[7] M. Schack, M. Jacob, and T. Kurner, "Comparison of in-car UWB and 60 GHz channel measurements," in *2010 Proceedings of the Fourth European Conference on Antennas and Propagation*. IEEE, 2010.

[8] J. Blumenstein, T. Mikulasek, R. Marsalek, A. Prokes, T. Zemen, and C. Mecklenbrauker, "In-vehicle mm-wave channel model and measurement," in *Vehicular Technology Conference (VTC Fall), 2014 IEEE 80th*. IEEE, 2014, pp. 1–5.

[9] J. Blumenstein, T. Mikulasek, R. Marsalek, A. Prokes, T. Zemen, and C. Mecklenbruker, "Measurements of ultra wide band in-vehicle channel - statistical description and TOA positioning feasibility study," *EURASIP Journal on Wireless Communications and Networking*, p. 15, 2015.

[10] J. Blumenstein, T. Mikulasek, R. Marsalek, A. Chandra, A. Prokes, T. Zemen, and C. Mecklenbrauker, "In-vehicle UWB channel measurement, model and spatial stationarity," in *Vehicular Networking Conference (VNC), 2014 IEEE*. IEEE, 2014, pp. 77–80.

[11] U. Demir, C. Bas, and S. Ergen, "Engine compartment UWB channel model for intravehicular wireless sensor networks," *IEEE Transactions on Vehicular Technology*, vol. 63, no. 6, pp. 2497–2505, July 2014.

[12] A. Chandra, A. Prokes, T. Mikulasek, J. Blumenstein, P. Kukolev, T. Zemen, and C. F. Mecklenbrauker, "Frequency-domain in-vehicle UWB channel modeling," *IEEE Transactions on Vehicular Technology*, vol. PP, no. 99, 2016.

[13] S. Lakušić, D. Brčić, and V. Tkalčević Lakušić, "Analysis of vehicle vibrations–new approach to rating pavement condition of urban roads," *PROMET-Traffic & Transportation*, vol. 23, no. 6, pp. 485–494, 2011.

[14] F. Hlawatsch and G. Matz, *Wireless communications over rapidly time-varying channels*. Academic Press, 2011.

[15] P. Bello, "Characterization of randomly time-variant linear channels," *IEEE Transactions on Communications Systems*, vol. 11, no. 4, pp. 360–393, 1963.

[16] S. W. Golomb *et al.*, *Shift register sequences*. Aegean Park Press, 1982.

[17] G. Matz, A. F. Molisch, F. Hlawatsch, M. Steinbauer, and I. Gaspard, "On the systematic measurement errors of correlative mobile radio channel sounders," *IEEE Transactions on Communications*, vol. 50, no. 5, pp. 808–821, 2002.

6 TIME-VARYING K FACTOR OF THE MM-WAVE VEHICULAR CHANNEL: VELOCITY, VIBRATIONS AND THE ROAD QUALITY INFLUENCE

This chapter is a postprint version of the following published paper:

J. Blumenstein, A. Prokes, **J. Vychodil**, M. Pospisil, and T. Mikulasek, "Time-varying K factor of the mm-Wave Vehicular Channel: Velocity, Vibrations and the Road Quality Influence," in *2017 IEEE 28th Annual International Symposium on Personal, Indoor, and Mobile Radio Communications (PIMRC)*, 2017, pp. 1–5.

Author of this thesis contribution

This paper is an extension of the ideas described in the previous chapter. The contributions of this thesis author are also similar: he developed the measurement system, helped with the realisation and conduction of the experiments and did basic data processing.

Time-varying K factor of the mm-Wave Vehicular Channel: Velocity, Vibrations and the Road Quality Influence

Jiri Blumenstein, Ales Prokes, Josef Vychodil, Martin Pospisil and Tomas Mikulasek
The Faculty of Electrical Engineering and Communication, Brno Univ. of Technology, Czech Rep.
email: blumenstein@vutbr.cz

***Abstract*—This paper evaluates real-world intra-vehicle millimeter-wave (mmWave) channel measurements performed in a vehicular environment. Utilizing a correlative time-domain channel sounder, we demonstrate the dependency of the time-varying Rician K factor on the road quality and instantaneous velocity of the measured vehicle. Vibrations caused by the movement of the vehicle together with mechanical properties of the vehicle's chassis leads to a mutual movement of the transmitting (TX) and the receiving (RX) antennas mounted on the front windshield and on the rear quarter window respectively. The channel sounding is performed in a frequency bandwidth from 59.1 GHz to 64 GHz with 50 GS/s sampling frequency.**

I. Introduction

To support a further evolution of wireless communication systems, considering that the demand for higher data rates still increases, the utilization of formerly unconventional and to some extent unused frequency bands is a precondition [1]. Recognized and promising is the millimeter-wave (mmWave) band. Orthodoxly perceived, the mmWave band spans from 30 GHz to 300 GHz. In this contribution we are however limited by our channels sounder to the frequency band from 59.1 GHz to 64 GHz. As determined by spectrum managing authorities, the mmWave band overlaps the unlicensed industrial scientific and medical (ISM) bands and thus it is remarkably attractive for both research and the industry.

Moreover, as seen by many researchers, vehicle-to-vehicle (V2V), vehicle-to-infrastructure (V2I) and in-vehicle communications may be one of the decisive features of the future cooperative self-driving vehicles [2]. Therefore, the V2V channel characterization and modeling is performed in [3], with a bandwidth of 240 MHz and 5.6 GHz carrier frequency, or with a bandwidth of 20 MHz at 2.4 GHz and 5.9 GHz carrier frequencies in [4].

In the field of in-vehicular mmWave channel characterization, there is a number of publications describing a mmWave channel stationarity [5], [6] or providing channel models and spatial maps [7]–[9]. Not only the passenger compartment is characterized, but also for example the engine bay characterization is the contribution of [10].

978-1-5386-3531-5/17/$31.00

Now, the vehicles are often a subject of vibrations, especially while in operation. The amplitude of the vibrations could be in the order of millimeters [11] and it is therefore comparable with the aptly called mmWave wavelength. The effect of antenna vibrations is studied in [12], [13], where number of possible vibration sources is listed. Mainly, the vibrations are caused by an uneven road surface, engine speed (in revolutions per minute) or sound system of the vehicle. In [12], [13], the vibrations are related to a Doppler spread of the sounding signal.

In this contribution, we utilize the datasets introduced in [12] and we evaluate the in-vehicle line-of-sight (LOS) link vibrations influence via the variations of the K factor.

Please note that the representative datasets, more detailed information about the mmWave time-domain channel sounder is available here: http://www.radio.feec.vutbr.cz/GACR-13-38735S/

II. Measurement

In this section we provide a description of the measurement location and the in-house build (from off-the-shelf components) channel sounder together with the theoretical fundamentals of the time-domain channel sounding with correlative real-time processing.

A. Principle of the correlative channel sounder

The utilized correlative channel sounder measures the transmission channel in the time domain. Other possibility to perform the channel sounding is to utilize the frequency domain channel sounders, where the sounder usually needs some time to sweep the band of interest. Subsequently, sounder stores the channel transfer functions [14]. In the time domain channel sounding, a broadband pulse or sequence is transmitted and the need for the channel sweep time is reduced. Therefore, the time domain channel sounding is suitable for time-variant channels, which is the case of our measured scenario.

(a) The dashboard of the measurement vehicle. Behind the absorbers is the RX with both the up/down Sivers IMA converters and the LNA.

(b) The trunk of the vehicle with the UPS power supply (good for around 1 hour of operation) and DC power supply for LNA and PA.

(c) The back seat. The TX antenna is fastened on the rear quarter window using a suction cap. The PA and the is covered by absorbers.

Fig. 1: Measurement setup pictures.

The time-variant channel is described by the channel impulse response (CIR) and is written as [15]:

$$h_m(t,\tau) = \sum_{n=1}^{N(t)} \alpha_n(t) e^{j2\pi f t} \delta\left(\tau - \tau_n(t)\right), \qquad (1)$$

where m is a measurement index and N is the number of propagation paths. The meaning of the measurement index is clarified in section II-B. Note that in this measurement campaign, due to the antenna installation, we ensured that the LOS components $h_{m\mathrm{LOS}}(t,\tau)$ are always present. The summation with the multipath components (MPCs) $h_{m\mathrm{MPC}}(t,\tau)$, i.e.:

$$h_m(t,\tau) = h_{m\mathrm{LOS}}(t,\tau) + h_{m\mathrm{MPC}}(t,\tau), \qquad (2)$$

creates alternative formula to (1).

The correlative channel sounding usually utilizes a properties of pseudo-noise sequences. In this paper, we employ m-sequences [16] with autocorrelation R_{xx} which is, in fact, a sharp triangle function. For our purpose, however, we can simplify to $R_{xx} \approx \delta(\tau)$. Thus, it is possible to write:

$$y(t) = h(t) \otimes x(t), \qquad (3)$$

where $y(t)$ is the received signal, $x(t)$ represents the transmitted m-sequence and finally $\otimes$ stands for a convolution.

Since the index of the transmitted m-sequence is known to the receiver, it is possible to estimate the CIR from the cross-correlation of the transmitted and received signals $x(t)$ and $y(t)$ respectively due to:

$$R_{xy}(\tau) = \mathrm{E}\{x^*(t)y(t)\} = h(t) \otimes R_{xx}(\tau) \approx$$
$$\approx h(t) \otimes \delta(\tau) = h(t), \qquad (4)$$

where $\mathrm{E}\{\}$ stands for the expected value operator. The approximate relation (4) is acceptable if conditions listed in [17] are met.

B. Measurement environment

We have utilized a typical European passenger vehicle, the second gen. Skoda Octavia, with a two-liter diesel engine. The pictures from the measurement campaign are shown in Figure 1.

The measurement campaign itself is consisted from number of channel measurements performed solely inside the car, while the car was in motion. For each channel recording, we have registered the instantaneous velocity. Furthermore, using a subjective three-step metric, the quality of the road was assessed by the driver (i.e., for each channel measurement, we have an index evaluating the "bumpiness" of the actual road). Thus, we have three groups of measurements designated as *smooth road*, *semi-bumpy* and *big potholes*.

Since the measurement setup mimics an intra-vehicle communication link with fixed antenna positions and the presence of the LOS is guaranteed by the installation, we are able to isolate the effect of the vehicle vibrations on the K factor.

1) Measurement devices: The block scheme of the in-house built channel sounder composed from the off-the-shelf components and measurement devices is visible in Figure 2.

The measurement setup consists of the oscilloscope Tektronix MSO72004C (acting as the RX) which was used as the matched receiver with 50 GS/s sampling frequency and 16 GHz bandwidth. The Anritsu Signal Quality Analyzer MP1800A (used as the TX) generates the m-sequences with 13 dBm output power and data rate 12.5 Gbit/s. To improve the dynamic range, the low-noise and power amplifiers QuinStar QLW-50754530-I2 and QPW-50662330 were used. We also utilized

the Sivers IMA FC1003V/01 up and down converter to move the signal to the band of interest.

2) Real-time data processing: The length of the m-sequences is given by the relation $L = 2^k - 1$, where L is the m-sequence length and k is the order of the m-sequence. In this work, we use $k = 11$, thus $L = 2047$.

Now, taking into account that we employ 50 GS/s sampling frequency and that the internal memory of the oscilloscope is 31.25 MS, we are able to capture $T = 3.246\,\text{s}$ of the transmitted signal into the fast internal memory of the oscilloscope (this represents more than 3000 CIRs snapshot for one measurement). Between each channel snapshot, there is a 1 ms pause required. Data are then uploaded to a PC and post-processed. After that, next measurements could be performed.

3) Note on the measurement index m: Each m index denotes a group of over 3000 CIRs recordings. Each group has the total duration of $T = 3.246\,\text{s}$. In total, we captured $m \in \{1, ..., 50\}$ CIRs groups.

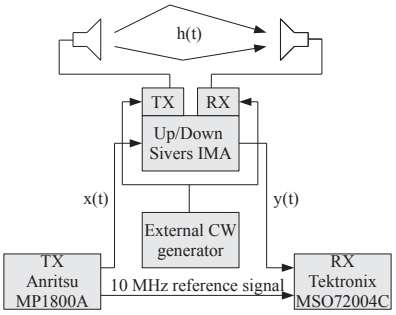

Fig. 2: Time-domain correlative channel sounder utilizing a m-sequence a stable external RF source and a matched receiver.

4) Antennas: The open-ended WR15 waveguide antennas were used at both the RX and TX ends. The radiation patterns are shown in Figure 3.

The TX antenna together with the power amplifier (PA) were mounted on the rear quarter window next to the rear passenger on the right hand side (Fig. 1c). The RX antenna, the low-noise amplifier (LNA) and the up/down converter were fitted approximately in the middle of the dashboard (Fig. 1a). The antennas were attached to the windows with suction caps.

III. Data Acquisition and Processing

A. Rician K factor estimation

The Rician K factor represents the ratio of the specular part r^2 and the variance of the multipath $2\sigma^2$ and is defined in [18] according to

$$K = 10\log_{10}(r^2/2\sigma^2)\ [\text{dB}]. \tag{5}$$

Since the utilized channel sounder is capable to capture the bandwidth of 4.9 GHz, we are not able to adopt the widely applied (e.g. [19], [20]) narrowband

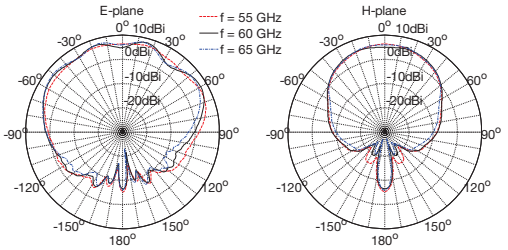

Fig. 3: Measured gain pattern of the open-ended WR15 waveguide in the E–plane and the H–plane for the 55-65 GHz frequency range.

method of moments [21]. We rely on the traditional method for estimation of the K factor from measured power versus time where the LOS component is determined by a peakfinder. Seeing that we measure a fixed link with a single-input single-output (SISO) configuration, the LOS components are always approximately at the same delay bin of the CIR. Therefore, the parametrization of the threshold based method for the estimation of the K factor is straightforward. Then, utilizing (5) and substituting $r(t) = \sum_\tau |h_{\text{LOS}}(t,\tau)|$ and $\sigma(t) = \sum_\tau |h_{\text{MPC}}(t,\tau)|$, we obtain the K factor as a function of time $K_m(t)$.

More detailed information about the channel sounder and how the CIR is obtained from the measured data is available in [13].

1) Decomposition of $K(t)$ into the fast and slow varying components: Based on a visual inspection of the measured data, we operate with a hypothesis that the K factor is composed from two elements according to:

$$K^*_m(t) = K_m(t) + K'_m(t), \tag{6}$$

where $K^*_m(t)$ is the measured K factor, $K'_m(t)$ represents the superimposed fast varying component (noise component) and $K_m(t)$ is the slowly varying component. This is depicted in Figure 4. The decomposition into the slow and fast varying components is done via a discrete wavelet denoising method introduced in [22].

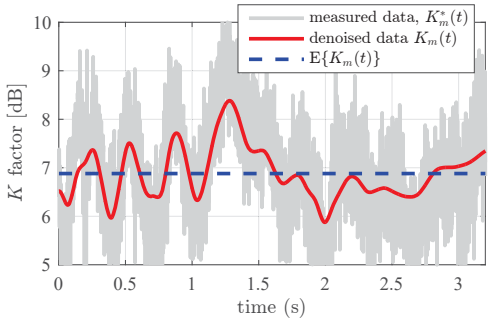

Fig. 4: Example of the K factor evolution in time. The spectrum of the slowly varying signal $K_m(t)$ is further analyzed.

2) Evaluation of the mean K factors: The mean value of the K factor is written as:

$$\mathrm{E}\{K_m(t)\} = \frac{1}{T}\sum_t K_m(t). \tag{7}$$

An example of the mean K factor for one specific measurement index m is depicted in Figure 4. To provide an overview of the mean K factor behavior while driving at variety of speeds and on variety of roads, please see Figure 5. Together with the mean values of the K factor for all measurements m, in Figure 5 we depict a linear fit (written as: $y = kx + c$) obtained by a maximum likelihood estimation (MLE). The values of the parameters k and c are listed in Table I. The interpretation of the results is as follows:

- The higher the speed is, the lower the K factor. It holds namely for the good roads from the group of *smooth surface*.
- If the road quality gets worse (to the level of *semi-bumpy*), the K factor again decreases with increasing speed, however it decreases significantly slower compared to the case of the *smooth surface* group of roads. The reason for this are probably the pronounced vibrations from the road. Interesting is that the *smooth surface* and *semi-bumpy* groups have approximately the same mean K factor for the highest speeds.
- The mean K factors obtained on the worst roads are on similar level as the *semi bumpy*, but we were not able to test all the speeds because the road quality was so poor that we risk damages on the vehicle.

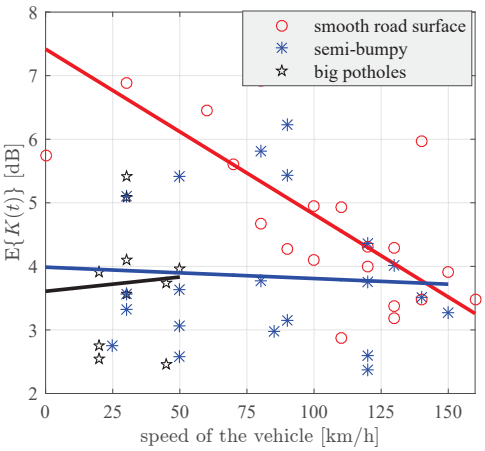

Fig. 5: Mean K factor (over the measurement time T) for all measured datasets $m \in \{1, ...50\}$. Linear fit parameters are listed in Tab. I

3) Analysis of the K factor variations: As demonstrated in Figure 4, the K factor $K_m(t)$ varies with time. Our hypothesis is, that the variations of the K factor are caused by the mechanical vibrations and mutual movement of the RX and TX antennas in general. The mechanical vibrations are related mainly to the road surface quality and vehicle speed. Therefore, utilizing the fast Fourier transform (FFT), we calculate the spectra of all available measurements m according to

$$K_m(f) = \mathrm{FFT}\{K_m(t)\}. \tag{8}$$

The results are plotted in Figure 6, where we also plot the mean spectral values of the representative road quality groups. It is visible, that as the road quality gets worse, the spectrum of the K factor $K_m(f)$ is broadened. In order to evaluate this broadening effect, we introduce a K factor frequency spread metric. The metric is given as a frequency spread, which is observed at the 40 dB decrease of the K factor spectrum $K_m(f)$ from its maximal value.

Now, the results of the K factor frequency spread are plotted in Figure 7 and we conclude that:

- The best road quality produces the lowest spread of the $K_m(f)$ values and the worst road quality produces the highest spread of the $K_m(f)$ values.
- K factor frequency spread increases with the speed.
- $K_m(f)$ spread increases faster as the road quality worsens.

Intuitively, the effect of the increasing speed and worsening of the road quality leads to a vibration increase. The K factor, influenced by a mutual antenna movement and variations of the of the antenna alignment, is shown as indirectly proportional to the vehicle vibrations.

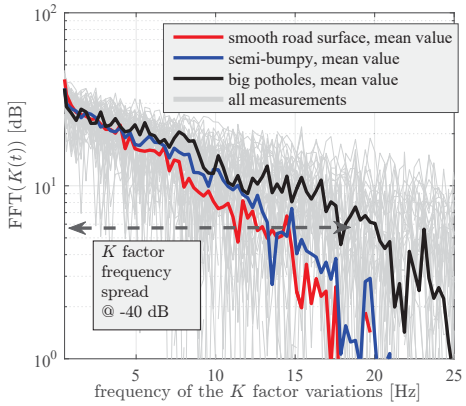

Fig. 6: Spectra of denoised $K(t)$ for all measurements (gray) and spectra of the mean values of the *smooth road*, *semi-bumpy* and *big potholes* groups.

IV. Conclusion

We present the K factor evaluation for variety of road conditions and the velocities of the measured vehicle. Since the measurement setup mimics an intra-vehicle communication link with fixed antenna positions and the

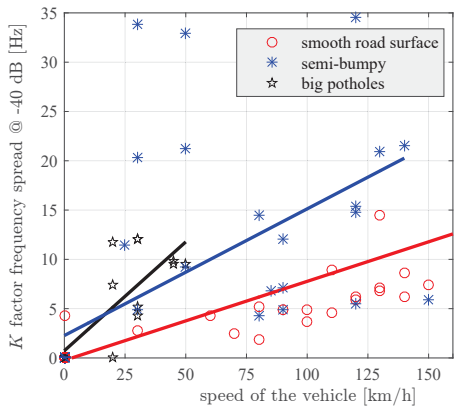

Fig. 7: The frequency spread of the denoised $K(f)$ for all measurements associated to the representative road quality groups.

TABLE I: Linear fit parameters of the of $\mathrm{E}\{K_m(t)\}$ and $\mathrm{FFT}\{K_m(t)\}\forall m$.

	mean K factor		K factor spread	
fit params. of $y = kx + c$ approx.	k	c	k	c
smooth road	-0.0260	7.418	0.0801	-0.248
semi-bumpy	-0.0017	3.987	0.1285	2.273
big potholes	0.0044	3.608	0.2208	0.732

presence of the LOS is guaranteed by the installation, we are able to isolate the effect of the vehicle vibrations. The baseline hypothesis is confirmed, the higher the speed of the vehicle, the lower the mean K factor. Also, the higher the speed, the higher variations of the K factor in the time domain.

The influence of the subjective index of the road quality on the K factor is also evaluated. The results show that as the road worsens, the mean K factor decreases while the frequency of the K factor variations is increased. In the absolute values, the presented results hold for one specific vehicle, one specific channel sounder and on top of that, for one specific test drive. However, the authors reckon that the shown trends will hold also for other (yet similar) vehicles.

ACKNOWLEDGMENT

The research described in this paper was financed by the Czech Science Foundation, Project No. 17-27068S, and by National Sustainability Program under grant LO1401. For the research, the infrastructure of the SIX Center was used.

REFERENCES

[1] T. S. Rappaport, S. Sun, R. Mayzus, H. Zhao, Y. Azar, K. Wang, G. N. Wong, J. K. Schulz, M. Samimi, and F. Gutierrez, "Millimeter wave mobile communications for 5G cellular: It will work!" *IEEE access*, vol. 1, pp. 335–349, 2013.

[2] C. Sommer and F. Dressler, *Vehicular Networking*. Cambridge University Press, 2014.

[3] T. Abbas, J. Nuckelt, T. Krner, T. Zemen, C. F. Mecklenbruker, and F. Tufvesson, "Simulation and measurement-based vehicle-to-vehicle channel characterization: Accuracy and constraint analysis," *IEEE Transactions on Antennas and Propagation*, vol. 63, no. 7, pp. 3208–3218, July 2015.

[4] M. Boban, T. T. V. Vinhoza, M. Ferreira, J. Barros, and O. K. Tonguz, "Impact of vehicles as obstacles in vehicular ad hoc networks," *IEEE Journal on Selected Areas in Communications*, vol. 29, no. 1, pp. 15–28, January 2011.

[5] J. Blumenstein, A. Prokes, A. Chandra, T. Mikulasek, R. Marsalek, T. Zemen, and C. Mecklenbruker, "In-vehicle channel measurement, characterization, and spatial consistency comparison of 3-11 GHz and 55-65 GHz frequency bands," *IEEE Trans. Veh. Technol.*, vol. 66, no. 5, pp. 3526–3537, May 2017.

[6] J. Blumenstein, T. Mikulasek, R. Marsalek, A. Chandra, A. Prokes, T. Zemen, and C. Mecklenbrauker, "In-vehicle UWB channel measurement, model and spatial stationarity," in *Vehicular Networking Conference (VNC), 2014 IEEE*. IEEE, 2014, pp. 77–80.

[7] J. Blumenstein, T. Mikulasek, R. Marsalek, A. Prokes, T. Zemen, and C. Mecklenbrauker, "In-vehicle mm-wave channel model and measurement," in *Vehicular Technology Conference (VTC Fall), 2014 IEEE 80th*. IEEE, 2014, pp. 1–5.

[8] M. Schack, J. Jemai, R. Piesiewicz, R. Geise, I. Schmidt, and T. Kurner, "Measurements and analysis of an in-car UWB channel," in *Vehicular Technology Conference, 2008. VTC Spring 2008. IEEE*, 2008, pp. 459–463.

[9] J. Blumenstein, T. Mikulasek, R. Marsalek, A. Prokes, T. Zemen, and C. Mecklenbrauker, "Measurements of ultra wide band in-vehicle channel - statistical description and TOA positioning feasibility study," *EURASIP Journal on Wireless Communications and Networking*, p. 15, 2015.

[10] U. Demir, C. Bas, and S. Ergen, "Engine compartment UWB channel model for intravehicular wireless sensor networks," *IEEE Transactions on Vehicular Technology*, vol. 63, no. 6, pp. 2497–2505, July 2014.

[11] S. Lakušić, D. Brčić, and V. Tkalčević Lakušić, "Analysis of vehicle vibrations–new approach to rating pavement condition of urban roads," *PROMET-Traffic & Transportation*, vol. 23, no. 6, pp. 485–494, 2011.

[12] J. Blumenstein, J. Vychodil, M. Pospisil, T. Mikulasek, and A. Prokes, "Effects of vehicle vibrations on mm-wave channel: Doppler spread and correlative channel sounding," in *2016 IEEE 27th Annual International Symposium on Personal, Indoor, and Mobile Radio Communications (PIMRC)*, Sept 2016, pp. 1–5.

[13] A. Prokes, J. Vychodil, M. Pospisil, J. Blumenstein, T. Mikulasek, and A. Chandra, "Time-domain nonstationary intra-car channel measurement in 60 GHz band," in *2016 International Conference on Advanced Technologies for Communications (ATC)*, Oct 2016, pp. 1–6.

[14] A. Chandra, A. Prokes, T. Mikulek, J. Blumenstein, P. Kukolev, T. Zemen, and C. F. Mecklenbruker, "Frequency-domain in-vehicle UWB channel modeling," *IEEE Trans. Veh. Technol.*, vol. 65, no. 6, pp. 3929–3940, June 2016.

[15] F. Hlawatsch and G. Matz, *Wireless communications over rapidly time-varying channels*. Academic Press, 2011.

[16] S. W. Golomb *et al.*, *Shift register sequences*. Aegean Park Press, 1982.

[17] G. Matz, A. F. Molisch, F. Hlawatsch, M. Steinbauer, and I. Gaspard, "On the systematic measurement errors of correlative mobile radio channel sounders," *IEEE Transactions on Communications*, vol. 50, no. 5, pp. 808–821, 2002.

[18] S. O. Rice, "Statistical properties of a sine wave plus random noise," *The Bell System Technical Journal*, vol. 27, no. 1, pp. 109–157, Jan 1948.

[19] A. Bottcher, P. Vary, C. Schneider, M. Narandzic, and R. S. Thoma, "Estimation of the radio channel parameters from a circular array with directional antennas," in *2011 IEEE 73rd Vehicular Technology Conference (VTC Spring)*, May 2011.

[20] L. Bernado, T. Zemen, F. Tufvesson, A. F. Molisch, and C. F. Mecklenbrauker, "Time- and frequency-varying K-factor of non-stationary vehicular channels for safety-relevant scenarios," *IEEE Transactions on Intelligent Transportation Systems*, vol. 16, no. 2, pp. 1007–1017, April 2015.

[21] L. J. Greenstein, D. G. Michelson, and V. Erceg, "Moment-method estimation of the ricean K-factor," *IEEE Communications Letters*, vol. 3, no. 6, pp. 175–176, June 1999.

[22] D. L. Donoho, "De-noising by soft-thresholding," *IEEE Transactions on Information Theory*, vol. 41, no. 3, pp. 613–627, 1995.

7 TIME-DOMAIN BROADBAND 60 GHZ CHANNEL SOUNDER FOR VEHICLE-TO-VEHICLE CHANNEL MEASUREMENT

This chapter is a postprint version of the following published paper:

A. Prokes, **J. Vychodil**, T. Mikulasek, J. Blumenstein, E. Zöchmann, H. Groll, C. F. Mecklenbräuker, M. Hofer, D. Löschenbrand, L. Bernadó, T. Zemen, S. Sangodoyin, and A. Molisch, "Time-Domain Broadband 60 GHz Channel Sounder for Vehicle-to-Vehicle Channel Measurement," in *2018 IEEE Vehicular Networking Conference (VNC)*, 2018, pp. 1–7.

Author of this thesis contribution

This paper describes an improved version of the discussed channel sounder. Contributions of this thesis author are, besides the overall channel sounder, the improvements on that system. Namely, the deployment of the Golay sequences as the probing signal, as was described in Sec. 3.4.3, and separating the transmitting and receiving side by using Rubidium disciplined oscillators and solving practical issues with synchronization, triggering and gating, thus enabling much more measurements scenarios.

Time-Domain Broadband 60 GHz Channel Sounder for Vehicle-to-Vehicle Channel Measurement

Ales Prokes[*], Josef Vychodil[*], Tomas Mikulasek[*], Jiri Blumenstein[*],
Erich Zöchmann[†‡*], Herbert Groll[‡], Christoph F. Mecklenbräuker[‡],
Markus Hofer[x] , David Löschenbrand[x] , Laura Bernadó[x]
Thomas Zemen[x] , Seun Sangodoyin[††], Andreas Molisch[††]

[*]Department of Radio Electronics, Brno University of Technology, Czech Republic, prokes@vutbr.cz
[†] Christian Doppler Laboratory for Dependable Wireless Connectivity for the Society in Motion
[‡] Institute of Telecommunications, TU Wien, Austria
[x] Safety and Security Department, Austrian Institute of Technology, Austria
[††] Wireless Devices and Systems Group, University of Southern California, USA

Abstract— **The paper deals with a time varying vehicle-to-vehicle channel measurement in the 60 GHz millimeter wave (MMW) band using a unique time-domain channel sounder built from off-the-shelf components and standard measurement devices and employing Golay complementary sequences as the excitation signal. The aim of this work is to describe the sounder architecture, primary data processing technique, achievable system parameters, and preliminary measurement results. We measured the signal propagation between two passing vehicles and characterized the signal reflected by a car driving on a highway. The proper operation of the channel sounder is verified by a reference measurement performed with an MMW vector network analyzer in a rugged stationary office environment. The goal of the paper is to show the measurement capability of the sounder and its superior features like 8 GHz measuring bandwidth enabling high time resolution or good dynamic range allowing an analysis of weak multipath components.**

Keywords—millimeter wave, channel measurement, channel sounder, channel impulse response

I. INTRODUCTION

Recent societal trends show a continuously increasing demand for high-speed mobile communications. The steadily growing number of communication devices per area and increasing quality of services require the allocation of more frequency resources. The global bandwidth shortage in the recently used frequency bands up to 6 GHz has motivated an exploration of the underutilized millimeter wave (MMW) frequency spectrum. MMW frequencies between 30 and 300 GHz have attracted growing attention as a possible candidate for next-generation cellular networks [1].

Designing any communication systems is impossible without a detailed knowledge of the transmission channel features. Specific limitations of MMW signal propagation, extremely large bandwidth and time-varying environment caused by mobile users connected to backhaul networks and traveling very often in rugged municipal environments, create unprecedented challenges to the development of broadband communication systems using advanced technologies for eliminating the undesirable time-varying channel features.

Recent works have primarily been aimed at channel analyses and modelling based on real-world measurement in the frequency domain (FD) or time domain (TD). FD sounders are most frequently based on a combination of a generator & a signal/spectrum/network analyzer, which use a continuous wave or a frequency-swept signal for the channel sounding [2], [3]. This type of the FD sounder is limited either to narrowband channels or due to a slow frequency sweep to stationary channels. In contrast the time domain sounders and certain types of FD sounders such as chirp [4] and multitone [5]–[8] allow time-varying broadband channel characterization. TD sounders can be based on an arbitrary waveform generator (AWG) generating an excitation signal in the form of very narrow repetitive impulses (e.g. Gaussian). A coherent detection of the pulses (often converted into in-phase and quadrature components) is possible using a wideband oscilloscope [9], [10]. Although pulse sounding systems are limited by high sensitivity to noise and interference due to the large peak-to-average-power ratio (PAPR) penalty [11], they are not very frequently used. Probably the most popular technique for channel sounding uses a time-based spread spectrum approach, where a wideband pseudorandom binary sequence (PRBS) transmitted through the channel is correlated at the receiver with an identical PRBS code [12]–[15]. Such *correlative* sounders exploit a constant signal envelope, which allows obtaining very good power efficiency, and further they exhibit a correlation gain, which extends the system dynamic range. Some drawback of such a concept is the longer measuring time. A special sub-category of PRBS-based systems is made up of "sliding" sounders. The correlation of the PRBS code is performed at a slightly offset bit rate that allows the received PRBS to "slide" past the slower sequence [16].

Note that choosing the appropriate PRBS for the channel sounding is very important. For example, the maximal length binary sequences (known as the *M*-sequences) have very good correlation properties (almost zero periodic correlation except for the peak) and, due to their periodicity, also minimal leakage effects caused by FFT [14]. Golay complementary sequences have similar properties and, moreover, they exhibit a great ability to mitigate unwanted nonlinearity effects produced by channel sounder analog circuits [17].

All the above sounders require some kind of receiver and transmitter synchronization. In the case of measurement at a shorter distance the synchronization is provided most frequently by 10 MHz reference or by a similar constant frequency signal [2], [3], [6]–[8], [10], and [13]–[16]. Note that some sounders use also a triggering signal to tell the receiver when the excitation signal is being transmitted. Longer measuring distances require a different approach. Time domain sounders generating narrow pulses can be triggered internally by the first received pulse [9]. Another synchronization technique uses two GPS disciplined oscillators or rubidium clocks which are installed separately in the receiving and transmitting sections [5], [12].

A comprehensive survey of channel sounders operating at frequencies above 3 GHz is presented in [11]. This study compares over 40 sounders, of which more than 20 works in the MMW band, in terms of carrier frequency, synchronization methods, bandwidth, and other features.

The main contributions of this paper are:

- Introduction of a new concept of time-domain broadband correlative MMW channel sounder built from off-the-shelf components and standard measurement devices, whose correct operation is demonstrated by a reference measurement.
- Presentation of original preliminary results of measurements aimed at the signal propagation between two passing cars and at the signal reflection by a car driving on a highway.

The new design of the sounder was motivated by the need to measure signal propagation, firstly inside a moving car [13] and then between vehicles. Although there are a number of various time-domain channel sounders published in the available literature, we have chosen our own concept which does not require any circuit design, is based on measurement devices available at our workplace (which significantly accelerated sounder realization and reduced total costs), and offers very good parameters, especially with respect to bandwidth, which is, according to our best knowledge, the largest among the published sounders. The large bandwidth is advantageous in small rugged environment (such as a car cabin) as it exhibits excellent time resolution of multipath components (MPCs).

The results are presented without any detailed analyses. The aim of the paper is to show the measurement capability of the channel sounder and to inspire interested workers in the field to realize broadband time-varying MMW channel measurements.

The rest of the paper is organized as follows. Section 2 describes the channel sounder architecture and the principle of operation, and gives a list of the fundamental parameters. Section 3 briefly informs about the techniques of signal processing used for the channel impulse response (CIR) calculation. Section 4 deals with the verification of the measured CIR with a reference obtained using a vector network analyzer (VNA). Then in Section 5, the real-world measurement results are shown. A summary of the paper is given in the conclusion.

II. Measurement Setup

The time-domain channel sounder, whose concept is based on [13], is composed of a transmitter (TX) and a receiver (RX). The transmitter depicted in Fig. 1 is based on an Anritsu MP1800A Signal Quality Analyzer (working as a PRBS generator), whose output baseband signal is upconverted into the MMW band using a SiversIma FC1005V/00 V-band up/down converter equipped with programmable PLL local oscillators [18]. To enhance the phase noise performance, the oscillators are disconnected and the reference signal for up-conversion is applied from an Agilent E8257B frequency-stable, low phase-noise generator. The low pass filter (LPF) is optional and limits, together with the internal up/down converter filter, the frequency band of PRBS. For mobile operation, the transmitter is supplied from an uninterruptible power supply DELL 5600W 4U 230V. The receiver in Fig. 2 is created using a Tektronix MSO72004C (20 GHz, 50 GS/s) Mixed Signal Oscilloscope, a SiversIma FC1003V/01 V-band up/down converter (without local oscillators) changing the frequency from the MMW band to the baseband, and a carrier generator Agilent 83752A. Downloading data from the oscilloscope, their basic processing, and setting the oscilloscope parameters are controlled by LabView.

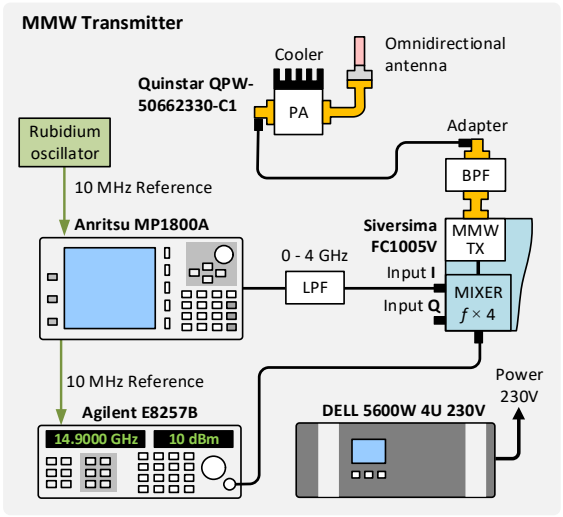

Fig. 1. Block diagram of the channel sounder TX part.

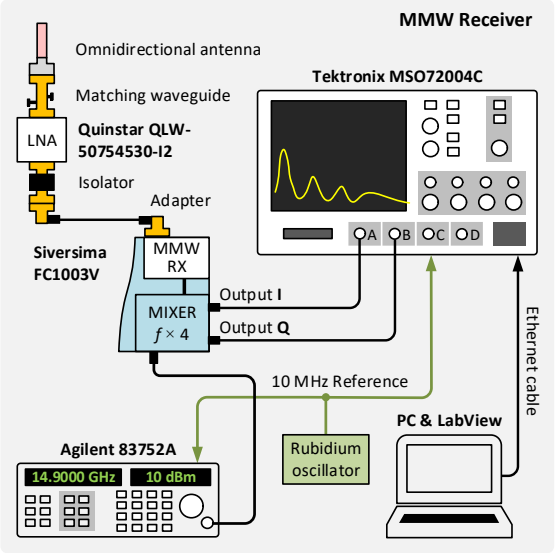

Fig. 2. Block diagram of the channel sounder RX part.

To compensate for large propagation loss in the MMW band and an attenuation in coaxial cables, the Quinstar QLW-50754530-I2 low noise amplifier (LNA) and QPW-50662330-C1 power amplifier (PA) are used. To achieve synchronization between transmitter and receiver both the channel sounder parts are supplied with a 10 MHz reference frequency generated by the Rubidium LPRO 10MHz Oscillators [19].

The operation of the testbed is straightforward. A seamless repeating signal based on the Golay complementary sequences at the data rate R_{PS} = 12.5 Gbit/s is frequency limited to the 0 – 4 GHz bandwidth and up-converted into the MMW band with center frequency of 59.6 GHz. A band-pass filter (BPF) partially suppresses the leakage of the local oscillator signal into the RF path to prevent PA saturation. Finally, the signal is fed into the power amplifier with a gain of 35 ±3 dB through a coaxial cable with an attenuation of 12 dB.

The output powers of the PRBS and reference signal generators are 5 dBm and 10 dBm respectively. In this case the MMW signal is transmitted and received using the omnidirectional SIW slot antennas [20]. The received signal then passes through the LNA with a gain of 33 ±3 dB and a noise figure of 4.5 dB and through the coaxial cable with an attenuation of 12 dB. To suppress the front-end oscillations caused by the large gain of the amplifier and the following SiversIma input circuits, a waveguide isolator and a special waveguide tuner with three screws working as a matching circuit are used. The quadrature down-conversion mixer produces two baseband signals, I and Q, which are digitized and stored in the internal memory of the oscilloscope working as a matched receiver. Because the converter includes the frequency multiplier by a factor of 4, the generator output frequency is set to 14.9 GHz.

The Golay sequences [21] are employed as the excitation signal due to their very good circular correlation properties, which invoke using a very convenient circular auto-correlation technique for the CIR calculation. The length of one sequence defines the maximum observable time span $T_{max} = N_b/R_{PS}$. For the chosen k = 11 we get N_b = 2048 and T_{max} = 163.8 ns. Assuming the speed of light $c = 3\times10^8$ m/s we can obtain the maximum observable distance L_{max} = 49.15 m. The Golay complementary sequences have also convenient properties when non-linear components are used in the measurement chain as mentioned above and described in [17]. Selected system parameters are summarized in Table 1 (see also Section III).

In order to suppress the oscilloscope wideband noise and down-converter LO leakage, we use a built-in 5 GHz user-selectable bandwidth limit filter. This option can only be used when the full sampling rate is chosen. Considering the memory depth of the oscilloscope M_D = 31.25 MSa per channel, the full sampling rate R_S = 50 GS/s, and the time span T_{max} = 163.8 ns we can calculate important system parameters such as the number of samples per CIR, number of saved CIRs, and total measurement time. To ensure sufficient measurement time, we insert the time delay T_D = 0.82 ms, 4.915 ms, or 9.83 ms between two subsequently saved CIRs. Because the maximum of 468 CIRs can be stored in the oscilloscope memory, the above sampling period allow us to analyze the channel within the time interval of T_M = 0.3 s, 2.3 s, or 4.6 s. The above time delays, which are controlled by the oscilloscope, are chosen to obtain simplified receiver synchronization, for which T_D is calculated as a least common multiplier of the 10 MHz reference signal period and total length of single or multiple sounding sequence ($8\times T_{max}$). However, to analyze the Doppler spread in a sufficient range, the T_D has to be significantly reduced. Such an improvement is possible, but not trivial. Note that a correlation technique complicates the evaluation of the Doppler shift caused by a moving vehicle. This is because the correlation of a frequency shifted PRBS with its pattern stored in the receiver, does not provide information about shift, but only affects the correlator output signal amplitude. This drawback can be solved for example by a bank of frequency-shifted PRBS patterns used for correlation. Unfortunately, to get reasonable sensitivity to relatively small frequency changes, the measurement bandwidth would have to be narrower or the PRBS would have to be longer. The reduction of T_D is necessary also because no anti-aliasing filter can be applied for image rejection of measured CIR sequences. For additional information about the channel sounder modified for UWB, see [22].

TABLE I. LIST OF SELECTED SYSTEM PARAMETERS

	Relation	Parameter
Number of PRBS bits [-]	$N_b = 2^k$	2048
Maximum observable time [ns]	$T_{max} = N_b/R_{PS}$	163.8
Maximum observable distance [m]	$L_{max} = cT_{max}$	49.13
Number of samples per CIR [-]	$N_{CS} = N_b R_S/R_{PS}$	8192
Number of saved CIRs [-]	$N_{CIR} = M_D/(8\cdot N_{CS})$	468
Total measurement time [s]	$T_M = N_{CIR}T_D$	0.38 (2.3, 4.6)
Correlation gain [dB]	$G_C = 10log(4\cdot N_{bit})$	39.1

III. Signal Processing Techniques

Signal processing techniques applied in the channel sounder include acquisition of particular PRBSs, mitigation of the spurs, and calculation of the CIR. Note that the sounder is calibrated before measurement. For this purpose, the receiver and the transmitter are interconnected via an attenuator and then the IQ imbalances are compensated, and the frequency characteristic is flattened. Because these operations are relatively complex, they will be the subject of another paper.

A. Generation of PRBS sequence and mitigation of spurs

Because some blocks of the channel sounder (especially amplifiers and mixers) exhibit nonlinear behavior and produce plenty of spurs, which can significantly decrease the dynamic range [23], the Golay complementary pair marked as $A(t)$, $B(t)$ is combined with the inverted counterparts $-A(t)$ and $-B(t)$ [17]. Each sequence is sent twice to reduce the overlapping ratio of different sequences caused by a multipath propagation. The complete transmit signal is then $[A(t)\ A(t)\ -A(t)\ -A(t)\ B(t)\ B(t)\ -B(t)\ -B(t)]$, i.e. a recurring sequence of $8\times N_b$ bits, is used for channel sounding. A received signal composed of several MPCs is up-sampled at the ratio of R_S/R_{PS} and correlated with the $[A(t)\ -A(t)\ B(t)\ -B(t)]$ sequences as shown in Fig. 3. The results of all four correlations are then averaged, which creates a single vector containing $N_{CS} = N_b R_S/R_{PS} = 8192$ samples.

Because we calculate four different cross-correlations, the correlation gain is $G_C \approx 10log(4\cdot N_{bit}) = 39.1$ dB. Since the dynamic range of the MSO72004C oscilloscope in the given frequency band is about 35 dB [24], the theoretical limit of total dynamic range approaches 74 dB. However, the spur mitigation technique based on the Golay complementary sequences is in practice of only limited efficiency, the real dynamic range of the sounder is about 45 dB.

B. Calculation of CIR

Suppose that the measured channel is time invariant for the coherence time, and then changes to a different fading state. Let, further, the time of a single CIR measurement be shorter than the coherence time, then the channel response $h(t,t')$ can be considered as a function of two time variables t and t', which in the following text denote the sampling time and the measurement time (time of capturing a sequence of CIRs) respectively.

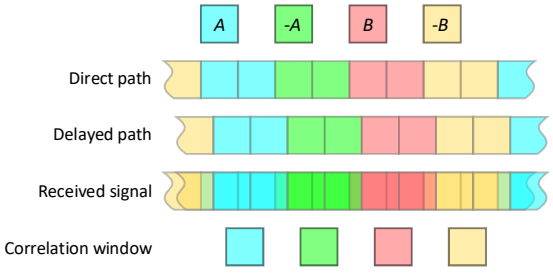

Fig. 3. Forming of received signal from the two time-overlapping components.

To estimate $h(t,t')$, the cross-correlation $R_{xy}(\tau,t')$ between the system input $x(t)$ and the output $y(t)$ may be employed [25]

$$R_{xy}(\tau,t') = h(t,t') * R_{xx}(t), \quad (1)$$

where $R_{xx}(t)$ is the autocorrelation function of the input signal $x(t)$ and $*$ denotes convolution. Because the autocorrelation $R_{xx}(t)$ of the Golay sequence is actually a sharp triangle function, we can write $R_{xx}(t) \approx \delta(t)$, where $\delta(t)$ is the Dirac pulse. Thus, the cross-correlation function is equal to the system impulse response as follows

$$R_{xy}(\tau,t') \approx [h(t,t') * \delta(t)] = h(t,t'). \quad (2)$$

Since the transmitted Golay sequences and their counterparts $x_i(t)$, where $x_1(t) = A(t)$, $x_2(t) = B(t)$, $x_3(t) = -A(t)$ and $x_4(t) = -B(t)$, are known in the receiver, the channel impulse response $h(t,t')$ can be estimated from the corresponding received sequences $y_i(t,t')$ using cross-correlation, and considering further the relation between correlation and convolution [25] the CIR can be finally expressed as

$$h(t,t') = \frac{1}{4}\sum_{i=1}^{4} x_i(t) * y_i^*(-t,t'), \quad (3)$$

where y^* is the complex conjugate of y. To accelerate the CIR calculation, equation (3) is transformed from the sampling time domain to the frequency domain and back using the complex (inverse) fast Fourier transform ((I)FFT)

$$h(t,t') = \frac{1}{4} IFFT \sum_{i=1}^{4}\{FFT[x_i(t)] \times FFT[y_i^*(-t,t')]\}. \quad (4)$$

Note that in real calculation the time is discrete i.e. $t = n/R_s$, where $n = \langle 1, N_b \rangle$.

IV. Verification of the Measured CIR via Reference Measurement

To verify the measurement accuracy, we performed several measurements in a rugged stationary office environment with the realized channel sounder in the time domain and with a calibrated Rohde & Schwarz ZVA67 VNA in the frequency

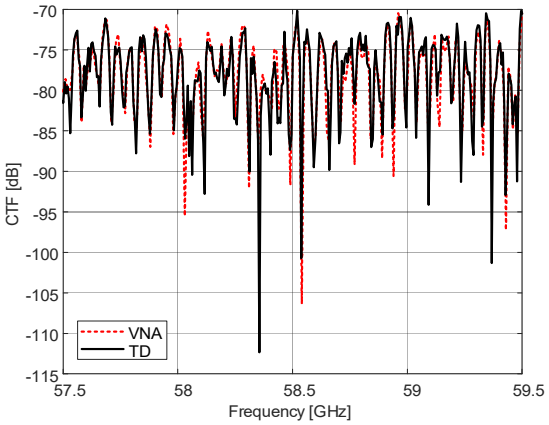

Fig. 4. Comparison of CTFs obtained by the vector network analyzer (VNA) and by the realized sounder (TD).

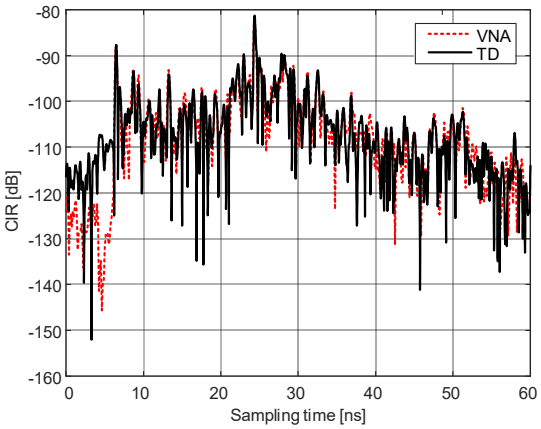

Fig. 5. Comparison of measured CIRs.

domain. The antennas were directed so that there was no LOS component. During the measurements, the antennas were fixed, and the environment was unchanged. The results were compared in both, the time and the frequency domains. Conversion between the two domains was performed using (I)FFT.

An example of the channel transfer functions (CTFs) comparison is shown in Fig. 4. To show the difference between CTFs more clearly, only a 2 GHz bandwidth cutout is shown. More important is the comparison of CIRs in the time domain shown in Fig. 5. It is obvious that there is a good match for both the CTFs and CIRs, especially at a high level of MPCs. Differences at low levels are caused by different intrinsic noise levels of the measurement setups. Because the coaxial cables used are not phase-stable, the measurement results are sensitive to their position and configuration. During the change of one measurement setup to another it is impossible to avoid some manipulation with the cables, which probably contributes to the

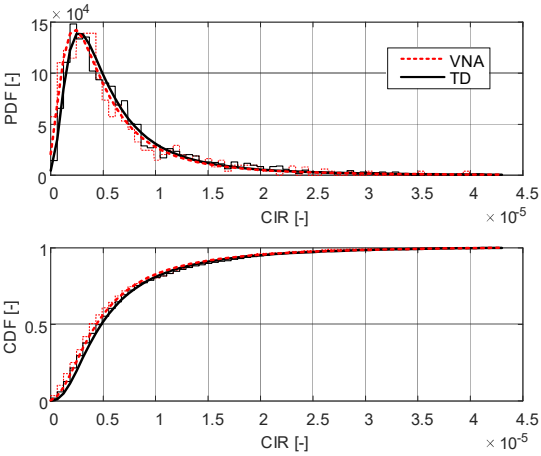

Fig. 6. Comparison of PDF and CDF calculated for CIRs measured in time and frequency domains.

Fig. 7. Testing the channel sounder using two passing cars.

differences also at higher levels of CTFs and CIRs. Other differences (predominantly at the beginning of CIRs) are caused also by the artefacts of FFT calculation.

The probability distribution function (PDF), calculated as a histogram, and the cumulative distribution function (CDF) of the CIRs depicted in Fig. 5 and converted into linear scale inside the interval from 5 to 55 ns and finally fitted by the *generalized extreme value* distribution are shown in Fig. 6. The differences between the CDFs and the PDFs are noticeable particularly at low signal levels, where the effect of the time domain sounder noise is significant.

V. REAL MEASUREMENTS

We tested the channel sounder in two different scenarios. In the first scenario, we measured the CIRs for two passing cars on the road (VW CC 2.0 TDi and Ford Fusion 1.4i) carrying the TX and RX parts of the sounder. The TX part was supplied with the uninterruptible power supply (UPS) as mentioned above, and the RX part from a power station carried on a trailer as shown in Fig. 7. The power station was used because of the large power

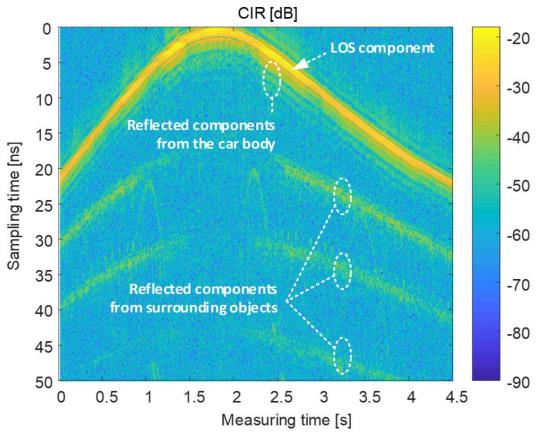

Fig. 8. Example of measured CIR evolving in time for the passing cars.

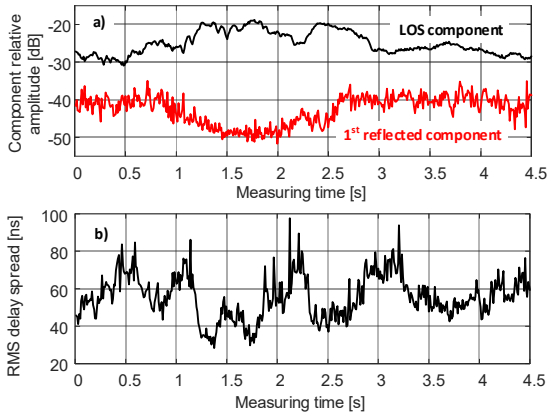

Fig. 9. Relative amplitude of the LOS and reflected component (a) and RMS delay spread (b) in dependence on measuring time.

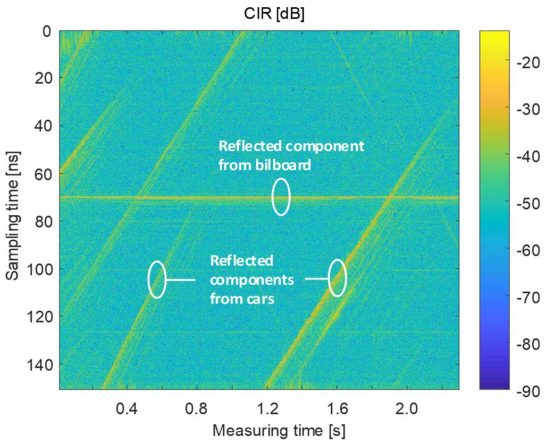

Fig. 11. Example of measured CIRs for cars driving on a highway.

consumption of the oscilloscope that would discharge an UPS in tens of minutes. The figure also shows details of the RX and TX front-ends mounted on the car roofs. An example of the measured CIR is shown in Fig. 8.

It is obvious that the CIR contains a few MPCs reflected from surrounding objects (street lighting columns, traffic signs and the wall situated on the farther side of the road) and from the car bodies (from roof and hood). While for longer distances between the cars the MPCs are relatively strong, in the case the cars are close together (lowest sampling time), the MPCs reflected from surrounding objects are weaker because the lighting columns and other objects are probably shadowed by the higher Ford Fusion car.

The level of the received signal components in dependence on the mutual position of the cars is also influenced by the radiation characteristics of the SIW slot antennas. Although they are designed as much as possible to be omnidirectional, there is some non-negligible variation in the radiation power from -7 dB to 5 dB (related to the mean value 0 dBi) depending on the frequency and horizontal irradiation angle [20]. The relative amplitudes of the LOS and the first components reflected from surrounding objects (the first component below the LOS component) calculated as the maximum values for each instant measuring time are shown in Fig. 9 a). The RMS delay spread in dependence on the measuring time is shown in Fig. 9 b). Its relation to the LOS component amplitude in Fig. 9 a) is obvious (the larger the amplitude the smaller the delay spread). Note that the sampling time values are not absolute. The vertical position of all the components depends on the time shift between the periodically generated PRBS and the manual triggering of the oscilloscope.

Fig. 10. Testing the channel sounder in "radar mode" on a highway.

In the second scenario, the sounder operated as a radar. The TX part was situated on a bridge above the highway and the RX part was mounted on a tripod standing below the bridge on the ground as shown in Fig. 10. To obtain a longer measuring distance (just for the reflected signal) we used a horn antenna (with gain of 24 dBi) on the receiver and an open waveguide (with gain of 6 dBi in the main lobe) on the transmitter.

It is evident from Fig. 11 that the vehicles have multiple reflection surfaces leading to the clustering of the CIR and that

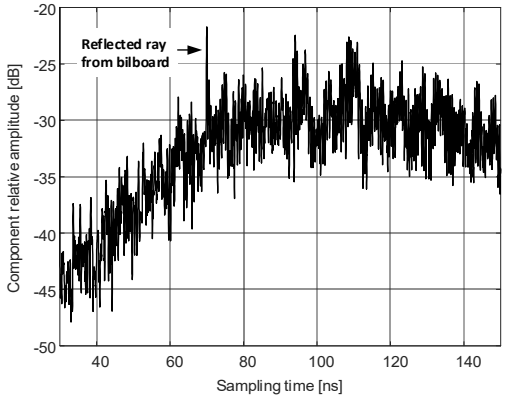

Fig. 12. Relative amplitude of the rightmost marked component from Fig. 11 in dependence on sampling time.

the speeds of vehicles are slightly different. The small-scale variation of the CIR relative amplitude is probably caused by the change of the reflecting area angle related to the antennas while the car is moving and shaking as demonstrated in Fig. 12 on the example of the rightmost marked component in Fig. 11. The reflected peak moves on the sampling time scale from about 30 ns to 150 ns in a measuring time interval of approximately 1 s (from 1.2 to 2.2 s). In other words, the distance of 120 ns × 3e8 m/s = 36 m is overcome during one second which corresponds to a velocity of 129.6 km/h.

VI. Conclusion

We propose a MMW channel sounder realized with commercial off the shelf (COTS) components only. It consists entirely of standard measurement devices and common microwave components. The sounder realizes 8 GHz bandwidth, more than 1000 measurements per second, up to a few seconds recording duration, and a satisfactory dynamic range. Its correct operation was verified using reference measurement obtained via VNA.

By analyzing the measured data we have discovered that in the case of vehicle-to-vehicle LOS channels the sounder allows analyzing relatively weak MPCs originating by interacting objects in the propagation environment, and that there is relatively large small-scale variation in the LOS component (even when cars are close to each other) caused probably by imperfect omnidirectional irradiation of the SIW slot antennas. It has also been found that the car driving on a highway exhibits multiple reflection surfaces and that the unavoidable small-scale variation of the LOS component is affected by the movement and shaking of the car.

Recently we have doubled the oscilloscope memory depth and currently are working on an acceleration of the CIR sequence measurement, a development of software for evaluation of the Doppler spread, a more precise description of RF and down-converting blocks, and on an analysis of the measured data.

Acknowledgment

The research described in this paper was financed by the Czech Science Foundation, Project No. 17-27068S, and by the National Sustainability Program under grant LO1401. For the research, the infrastructure of the SIX Center was used. The financial support by the Austrian Federal Ministry for Digital and Economic Affairs is gratefully acknowledged.

References

[1] M. R. Akdeniz et al., "Millimeter wave channel modeling and cellular capacity evaluation," *IEEE Journal on Selected Areas in Communications*, vol. 32, no. 6, pp. 1164-1179, June 2014.

[2] X. Wu et al., "60-GHz Millimeter-Wave Channel Measurements and Modeling for Indoor Office Environments," *IEEE Transactions on Antennas and Propagation*, vol. 65, no. 4, pp. 1912-1924, April 2017.

[3] J. Zhu, H. Wang and W. Hong, "Characterization of large-scale fading for 45 GHz indoor channels," in *3rd Asia-Pacific Conference on Antennas and Propagation*, Harbin, 2014, pp. 728-730.

[4] S. Salous, N. Nikandrou and N. F. Bajj, "Digital techniques for mobile radio chirp sounders," *IEE Proceedings - Communications*, vol. 145, no. 3, pp. 191-196, June 1998.

[5] C. U. Bas et al., "A Real-Time Millimeter-Wave Phased Array MIMO Channel Sounder," in *2017 IEEE 86th Vehicular Technology Conference (VTC-Fall)*, Toronto, 2017, pp. 1-6.

[6] W. Keusgen, A. Kortke, M. Peter and R. Weiler, "A highly flexible digital radio testbed and 60 GHz application examples," in *2013 European Microwave Conference,* Nuremberg, 2013, pp. 740-743.

[7] E. Zöchmann et al. "Measured Delay and Doppler Profiles of Overtaking Vehicles at 60 GHz," in *12th European Conference on Antennas and Propagation*, London, 2018, pp. 1-5.

[8] S. Sangodoyin, J. Salmi, S. Niranjayan and A. F. Molisch, "Real-time ultrawideband MIMO channel sounding," in *6th European Conference on Antennas and Propagation* (EUCAP), Prague, 2012, pp. 2303-2307.

[9] T. S. Rappaport, "Characterization of UHF multipath radio channels in factory buildings," *IEEE Transactions on Antennas and Propagation*, vol. 37, no. 8, pp. 1058-1069, Aug. 1989.

[10] A. Chandra, J. Blumenstein, T. Mikulášek, J. Vychodil, R. Maršálek, A. Prokeš, T. Zemen, C. A. Mecklenbräuker, "Serial subtractive deconvolution algorithms for time-domain ultra wide band in-vehicle channel sounding," *IET Intelligent Transport Systems*, vol. 9, no. 9, pp. 870–880, Nov. 2015.

[11] G. R. MacCartney, Jr. and T. S. Rappaport, "A Flexible Millimeter-Wave Channel Sounder with Absolute Timing," *IEEE Journal on Selected Areas in Communications*, vol. 35, no. 6, pp. 1402-1418, June 2017.

[12] R. Zhang, S. Wang, X. Lu, W. Duan and L. Cai, "Two-Dimensional DoA Estimation for Multipath Propagation Characterization Using the Array Response of PN-Sequences," *IEEE Transactions on Wireless Communications*, vol. 15, no. 1, pp. 341-356, Jan. 2016.

[13] A. Prokes, J. Vychodil, M. Pospisil, J. Blumenstein, T. Mikulasek and A. Chandra, "Time-domain nonstationary intra-car channel measurement in 60 GHz band," 2016, in *International Conference on Advanced Technologies for Communications (ATC)*, Hanoi, 2016, pp. 1-6.

[14] R. Zetik, M. Kmec, J. Sachs, and R. S. Thomä, "Real-Time MIMO Channel Sounder for Emulation of Distributed Ultrawideband Systems," *Int. J. Antennas Propag*., vol. 2014, Article ID 317683, pp. 1–16, 2014.

[15] G. R. MacCartney, Jr. and T. S. Rappaport, '5G mmWave Channel Sounder', 2017. [Online]. Available: https://wireless.engineering.nyu.edu/mmwave-5g-channel-sounder/. [Accessed: 10- Jun- 2018].

[16] D. Ferreira, R. F. S. Caldeirinha and N. Leonor, "Real-time high-resolution radio frequency channel sounder based on the sliding correlation principle," *IET Microwaves, Antennas & Propagation*, vol. 9, no. 8, pp. 837-846, June 2015.

[17] J. Vychodil, M. Pospisil, A. Prokes, J Blumenstein, "Millimeter Wave Band Time Domain Channel Sounder, " *IET Communications.* Accepted for publication.

[18] 'FC1005V/00 V-band Converter with LO'. [Online]. Available: https://www.siversima.com/wp-content/uploads/FC1005V00-Data-Sheet.pdf. [Accessed: 15- Jun- 2018].

[19] 'LPRO Rubidium Oscillator for Time & Frequency Reference. User's guide and integration guidelines', [Online]. Available: http://www.ham-radio.com/sbms/LPRO-101.pdf. [Accessed: 18- May- 2017].

[20] T. Mikulasek, J. Blumenstein, and A. Prokes, "Antennas utilized for intra-vehicle 3-11 GHz and 55-65 GHz channel measurement," in *37th PIERS*, Shanghai, 2016, pp. 1–5.

[21] M. Golay, "Complementary series," *IRE Transactions on Information Theory*, vol. 7, no. 2, pp. 82–87, Apr. 1961.

[22] J. Vychodil, A. Chandra, T. Mikulasek, A. Prokes and V. Derbek, "UWB time domain channel sounder," in *Radioelektronika*, Pardubice, 2015, pp. 268–271.

[23] S. A. Billings , S. Y. Fakhouri, "Identification of non-linear systems using correlation analysis and pseudorandom inputs," *International Journal of Systems Science*, vol. 11, no. 3, pp. 261–279, Jan. 1980.

[24] 'MSO/DPO70000 Series Digital and Mixed Signal Oscilloscopes Datasheet', 2016. [Online]. Available: http://www.tek.com/datasheet/mso-dpo70000-series-digital-and-mixed-signal-oscilloscopes-datasheet. [Accessed: 15- Jun- 2018].

[25] R. J. Polge and E. M. Mitchell, "Impulse Response Determination by Cross Correlation," *IEEE Transactions on Aerospace and Electronic Systems,* vol. AES-6, no. 1, pp. 91–97, Jan. 1970.

8 VEHICLE-TO-VEHICLE MILLIMETER-WAVE CHANNEL MEASUREMENTS AT 56-64 GHZ

This chapter is a postprint version of the following published paper:

J. Blumenstein, A. Prokes, **J. Vychodil**, T. Mikulasek, E. Zochmann, H. Groll, C. F. Mecklenbrauker, M. Hofer, T. Zemen, S. Sangodoyin, and A. Molisch, "Vehicle-to-Vehicle Millimeter-Wave Channel Measurements at 56-64 GHz," in *2019 IEEE 90th Vehicular Technology Conference (VTC2019-Fall)*, 2019, pp. 1–5.

Author of this thesis contribution

This paper describes more advanced measurements that were done using the channel sounder with improvements mentioned in the previous chapter. The author of this thesis, besides developing and improving the channel sounder, helped with arranging the measurement campaign and with performing the measurements. He also provided basic data processing.

Vehicle-to-Vehicle Millimeter-Wave Channel Measurements at 56-64 GHz

Jiri Blumenstein*, Ales Prokes*, Josef Vychodil*, Tomas Mikulasek*,
Erich Zöchmann†‡, Herbert Groll‡, Christoph F. Mecklenbräuker‡,
Markus Hofer^x, Thomas Zemen^x, Seun Sangodoyin††, Andreas Molisch††

* *Department of Radio Electronics, Brno University of Technology, Czech Republic,* blumenstein@vutbr.cz
† *Christian Doppler Laboratory for Dependable Wireless Connectivity for the Society in Motion*
‡ *Institute of Telecommunications, TU Wien, Austria*
^x *Safety and Security Department, Austrian Institute of Technology, Austria*
†† *Wireless Devices and Systems Group, University of Southern California, USA*

***Abstract*—This paper presents results obtained from a vehicle-to-vehicle channel measurement campaign carried out in the millimeter-wave band around a 60 GHz center frequency and with 8 GHz of bandwidth. We characterize a situation of two oncoming cars on a two-lane road in the campus of the Brno University of Technology. For several vehicle passes we evaluate: (1) observed root mean square (RMS) delay spreads as a function of the received power, (2) temporal decorrelation of the channel impulse response and (3) a dependency of the Pearson correlation coefficient on the received power. For the measurement campaign, a correlative time-domain channel sounder was used.**

***Index Terms*—mm-wave, channel measurement, vehicle-to-vehicle, channel delay spread**

I. Introduction

The millimeter wave (mmwave) band has been in the focus of the research community for decades, see, e.g., [1]. However, thanks to the inclusion of this band in the 5G standard [2] and thanks to the fact that mmwave bands offer several GHz of unlicensed bandwidth for industrial scientific and medical (ISM) purposes, the interest has greatly increased over the past few years. Literature on the general mmwave channel characterization has made considerable progress, see, e.g., an overview in [3]. In [4], a vehicle-to-vehicle (V2V) scenario is discussed and path-loss and fading characteristics are derived; however, with a rather limited bandwidth of 400 MHz at 73 GHz center frequency. A narrow-band car-to-car communication with a 1 Mb/s data transmission in the 60 GHz band was investigated in [5] already in 2001. For vehicular mm-wave channels, the number of investigations is more limited. Refs. [6]–[9] deal with specific phenomena like vibrations and road surface quality influence on a Doppler spread. Clearly, aiming at multi-GB/s data transmissions required for the future V2V and vehicle-to-infrastructure (V2I) links [10], several GHz of bandwidth are needed. Therefore, the wide-band channel characterization of the V2I environment is studied in [11]. An example of a V2V measurement campaign is published in [12]. Here, the transmitter (TX) and receiver (RX) are stationary, while the surrounding traffic causes a time-variant nature of the channel. It is worth noting that few vehicle-to-vehicle measurements of the wide-band channel have been published due to obvious complications with a precise synchronization of the mutually moving TX and RX which can not be done simply via a classical 10 MHz coaxial cable. In this paper we overcome this issue by means of stable local oscillators. Our measurement is done for a frequency band spanning 56 GHz to 64 GHz utilizing a correlative time-domain channel sounder presented, e.g., in [13]. Specifically, this paper contributes to the mmwave V2V wide-band channel characterization as follows:

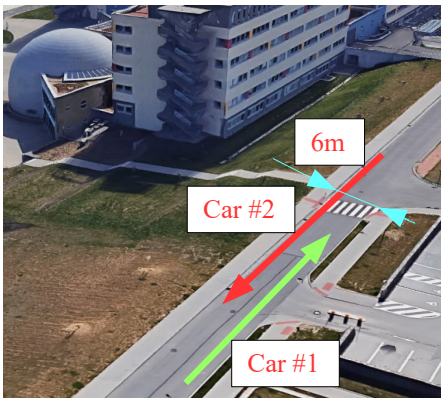

Fig. 1. The test site. Two cars driving in opposite direction on a two-lane road. Several passes ware performed at speeds within the city speed limit (50 km/h).

- We present exemplary results of V2V channel measurement campaign performed for two oncoming cars during subsequent events: (1) driving towards each other, (2) passing and (3) driving away from each other.
- We evaluate the RMS delay spread for a number of vehicle passes as a function of received power.
- Moreover, we investigate the temporal decorrelation of the channel, more precisely, we show how the Pearson correlation coefficient of the channel impulse responses (CIRs) decreases with time difference of the reception.

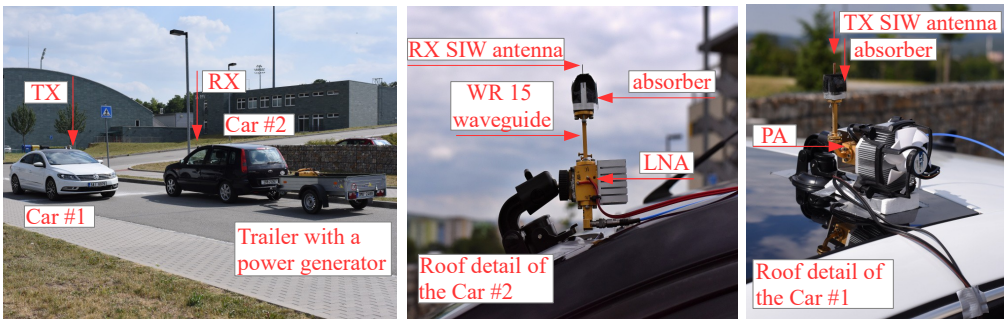

Fig. 2. Photographs taken during the measurement campaign. Two measurement vehicles, Car #1 (with a battery pack in the trunk) and Car #2 (with a 2 kW gas-powered generator on the depicted trailer) at their approximate meeting point. Picture of TX and RX mounting including PA and LNA installation detail.

II. Description of the Measurement Scenario

A. Test-Site Characterization

The measurement campaign was performed on the campus of the Brno University of Technology, in the city of Brno, Czech Republic. The location and controlled traffic ensures a non-obstructed line-of-sight (LOS) during the whole CIR recording time. In fact, no other participating cars nor notable moving objects were present during the measurements. There are no buildings around the immediate perimeter of the driven two-lane road; however, there is a university building around 50 m from the notional meeting point of the passing vehicles. In Figure 1, we depict the location from the bird-eye's view.

B. Measurement Vehicles and RX and TX hardware

We utilize two vehicles labeled as car #1 and #2, where #1 carries the TX and #2 the RX, as seen in Figure 2. In order to provide the TX and RX hardware with electricity, the TX was powered by a large battery pack loaded in the trunk, while the RX was supplied by a gas-powered generator loaded on the trailer, as depicted in Figure 2.

As for the utilized antennas, omni-directional substrate integrated waveguide (SIW) antennas presented in [14], [15] were used both at the RX and TX sides. The mounting of the antennas was done by suctions caps on the top-left corners (from the driver's perspective) of the measurement vehicle's windshields.

III. Channel Sounder

The time-variant radio propagation channel is defined by the CIR and, written as [16]:

$$h(t,\tau) = \sum_{n=1}^{N(t)} \alpha_n(t) e^{j2\pi\nu_D t} \delta\left(\tau - \tau_n(t)\right), \qquad (1)$$

where N is the number of propagation path components characterizing the amount of channel reverberation. Note that in this measurement campaign, the LOS components are always present. The variables $\alpha_n(t)$ and $\tau_n(t)$ corresponds to the amplitude and delay of the n-th propagation path while δ is the Dirac impulse and ν_D is the Doppler frequency. Exploiting Golay sequences [17] with a triangular autocorrelation function R_{xx} as a sounding (transmitted) signal $x(t)$, the received signal $y(t)$ is given as (neglecting noise here for convenience of notation):

$$y(t) = h(t) \otimes x(t), \qquad (2)$$

where $\otimes$ stands for the linear convolution. The CIR estimate is then determined from the cross-correlation of the received and transmitted signals $x(t)$ and $y(t)$ is written as:

$$R_{xy}(\tau) = \mathrm{E}\{x^*(t)y(t)\} = h(t) \otimes R_{xx}(t) \approx$$
$$\approx h(t) \otimes \delta(\tau) = h(t), \qquad (3)$$

where $\mathrm{E}\{\}$ denotes for the expected value operator. More details on this method is available in [18].

A. Calibration and Synchronization

The utilized correlative time-domain channel sounder is based on our previous work, e.g. described in [13], [19]. The main difference here is that the TX and RX parts are galvanically separated in order to allow the mutual movement, as required by the V2V scenario. The synchronization is achieved via a calibration process which requires back-to-back connection of the WR15 TX waveguide output with the input of the RX through a continuously adjustable attenuator in order to calibrate the system for a correct transmit power avoiding RX overdrive. The TX power is then kept constant for the whole measurement. After the calibration and fastening of the SIW antennas (which are not part of the calibration), the synchronization is held by rubidium (Rb) oscillators, whose specifications are given in [20]. The block diagram of the utilized time-domain channel sounder is shown in Figure 3.

B. Components and Parameters

The time-domain channel sounder is built from standard laboratory devices and off-the-shelf parts. We utilize a Tektronix MSO72004C Mixed Signal Oscilloscope performing a matched reception with 50 GS/s sampling frequency and 20 GHz bandwidth. This received signal is filtered in the baseband with a microstrip low-pass filter with 8 GHz bandwidth.

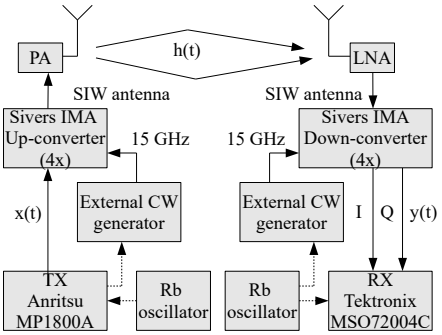

Fig. 3. Time-domain correlative channel sounder utilizing Golay sequences, omni-directional SIW antennas and local rubidium oscillators.

In order to tackle the nonlinearities of the measurement setup, in particular the nonlinearities of the power amplifier (PA), we employ distinct repetition pattern of the transmitted complementary Golay sequences. We transmit two complementary sequences, each 4-times repeated with different polarity. This method is elaborated in [13], [19]. The repetition of the transmitted signal in the time domain also increases the correlation gain, which is needed in order to overcome the path-loss at 60 GHz with 8 GHz of bandwidth. The basic length of the sequence is $\mathrm{L} = 2048$ and the correlation gain is given as $10\log(4\mathrm{L}) = 39.1$ dB. Then, the signal is up-sampled leading to a length of the sequence being $4 \times 8\mathrm{L} = 65536$ samples. With the 50 GS/s sampling frequency we are able to store 492 channel snapshots into the fast internal memory of the oscilloscope (31.25 MS). We set an artificial time lag of $\mathrm{T_L} = 9.93$ ms in between subsequent pseudorandom binary sequence (PRBS) transmissions in order to obtain a total channel recording time $\mathrm{T} \approx 4.6$ s.

The TX part consists of an Anritsu Signal Quality Analyzer MP1800A which generates a wide-band PRBS (in our case the mentioned Golay sequences) with 12.5 Gbit/s data rate and 13 dBm output power. The dynamic range is extended via the low-noise and power amplifiers QuinStar QLW-50754530-I2 (gain of 35 $\pm$3 dB) and QPW-50662330 (with a gain of 33 $\pm$3 dB and a noise figure of 4.5 dB) respectively. In order to move the signal to the desired mmwave band, we utilize the Sivers IMA FC1003V/01 up-/down-converter. The attenuation of coaxial cables used for connecting either the PA or LNA with the up-/down-converters is 12 dB.

IV. Measurement Results

As an exemplary data set of the measured CIRs for one pass of the measurement vehicles, we depict Figure 4. The CIRs exhibit typical properties that could be related to the mentioned driving situations. Via a visual inspection we distinguish:

1) the vehicles #1 and #2 are directly approaching each other in the time interval $t \in [0, 2.4)$ s and the received power increases with a delay dispersion of the channel.
2) The cars meet each other at time $t \approx 2.4$ s with a minimal mutual distance of approx. 3 m, while the received energy and the delay dispersion are maximized.
3) The measurement vehicles are driving away from each other in the time interval $t \in (2.4, 4.6]$ s. The received power decreases with time and exhibits variations, probably due to a slight ripple of the rear half-sphere of the radiation pattern of the antennas, as visible in [14].

As mentioned in previous section, the CIR recoding covers approximately 4.6 s. The depicted data are normalized (i.e. $\max(|h(t,\tau)|) \triangleq 1$) and thresholded such that all components with the amplitude below 0.1 are neglected.

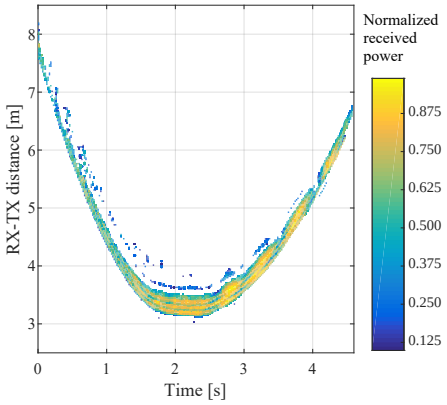

Fig. 4. Exemplary channel impulse recording of one pass of the vehicles. The measured data are thresholded, therefore the noise background is not depicted.

A. The channel delay dispersion

In the literature (see e.g. [21]), the delay dispersion of the channel is often evaluated via the root mean square (RMS) delay spread and is defined as:

$$\sigma_{\mathrm{RMS}}(t) = \sqrt{\frac{\int_0^\infty (\tau - \bar{\tau}^2) P(t,\tau)}{\int_0^\infty P(t,\tau)}}, \text{ where } \bar{\tau} = \frac{\int_0^\infty \tau P(t,\tau)}{\int_0^\infty P(t,\tau)} \tag{4}$$

where τ is the time delay, i.e. the y-axis in Figure 4 and

$$P(t,\tau) = \lim_{t \to T_s} \frac{1}{2T} \int_0^{T_s} |h(t,\tau)|^2 dt, \tag{5}$$

where T_s is the time region where quasi-stationarity is valid [21]. It is evident, that typical dimensions of the quasi-stationarity regions are highly dependent on the geometry and other relevant properties of the V2V scenarios (see e.g. [11]). This measurement campaign has eliminated surrounding traffic; consequently the LOS component and possible reflections from the measurement cars are the dominant sources of the received signal. In this case, the practically achieved results of the RMS delay spread are evaluated for each measured CIR for several passes of the vehicles in Figure 5. Please note that individual CIRs are aligned by the LOS (maximal) component.

Here, we define 8 power bins such that the summed received power $\sum_\tau P(t,\tau)$ for each individual measurement falls into one bin of a uniformly divided interval $[0.3, 1]$. In Figure 5, each gray point represents one measured CIR and it is noticeable that the higher the received power, the higher the RMS delay spread. The intuition behind this result is, that the reflections with lowest received power are simply buried under the noise floor and do not contribute to the RMS delay spread. Due to the mobile nature of the channel, it is not possible to average out the noise in (5), as one could do in a stationary environment. In order to illustrate the phenomena of the rising RMS delay spread with the received power, the mean values of the observed RMS delay spread are evaluated for each power bin and are shown as a blue cross. The variances of the corresponding dataset are depicted as the error bars. The mean values are linearly regressed to highlight the trend.

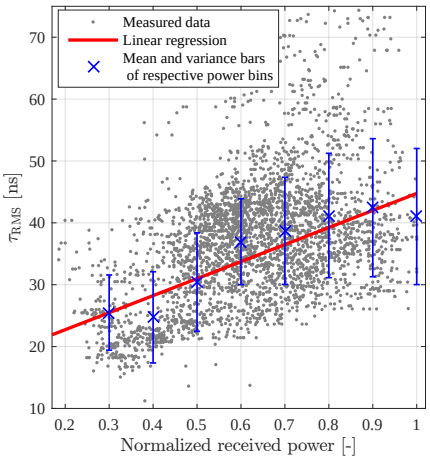

Fig. 5. Measured RMS delay spread for passing cars including mean and variance evaluation for respective normalized received power bins. Mean values of the respective power bins are linearly regressed.

B. The Channel Correlations

The channel quasi-stationarity time T_s, as discussed in the previous section, is a time duration over which the channel statistics do not change noticeably [21]. In order to evaluate the level of change, we employ the Pearson correlation coefficient (as in [22]), which is given as:

$$\rho(\Delta t) = \frac{\mathrm{E}[h'(t) - \mu_{h'(t)})(h'(t+\Delta t) - \mu_{h'(t+\Delta t)})]}{\sigma_{h'(t)}\sigma_{h'(t+\Delta t)}}, \quad (6)$$

where $h'(t) = |h(t,\tau)|^2$ and $\sigma_{h'(t)}$ denotes the standard deviation while $\mu_{h'(t)}$ is the mean value of $h'(t)$. The correlations are calculated for different time differences Δt to see how much time can pass while the correlation of two delayed CIRs is kept above a certain level ρ. For the following, we choose $\rho = 0.5$.

In Figure 6 we can observe the Pearson correlation coefficient ρ as a function of the time lag Δt. We plot data for 7 passes of the vehicles and for $\Delta t \in [0, 2]$ s. The mean value of correlation is evaluated for the whole measurement region, i.e., $\mathrm{E}[\rho],\ \forall\ t \in [0, 4.6]$ s together with its variance depicted as the error bars. It is visible that the $\mathrm{E}[\rho] > 0.5$ for $\Delta t \in [0, 50]$ ms. In order to compare, in [23], for V2V channels at 5.6 GHz and with 240 MHz of bandwidth in a notably more rugged environment, the coherence times are in the range from 180 to 500 μs depending on the driving situation.

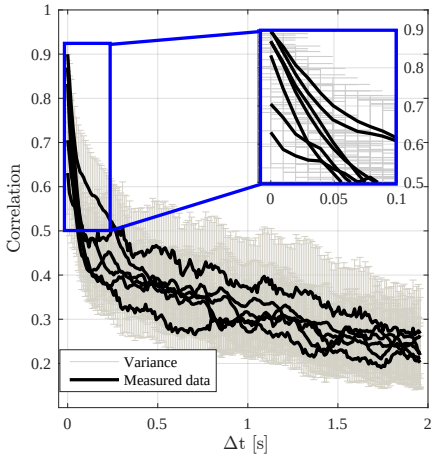

Fig. 6. Pearson correlation coefficient evaluation for several passes as a function of a correlation distance Δt.

In Figure 7 we show a dependency of $\mathrm{E}[\rho],\ \forall\ t \in [0, 4.6]$ s on the summed received power $\sum_\tau P(t,\tau)$ showing that the higher the total received power, the higher the correlations. The intuition is, that the lower the received power, the content of noise is proportionally higher, thus decreasing the correlation.

V. Conclusion

We have conducted broadband (with 8 GHz bandwidth) V2V mmwave channel measurements demonstrating the power-delay profiles of vehicles passing each other on a two-lane road. We evaluate the stationarity durations via a correlation between delayed channel impulse responses showing that in order to have mean correlations higher then 0.5, the time lag between measurements cannot be higher then 50 ms. Also, we show that the RMS delay spread increases with the received power. This poses an interesting problem, where usually the higher the signal-to-noise ratio (SNR), the lower the bit error rate (BER) of a hypothetical communication system without perfect channel state information (CSI). However, at the same time we show that the higher the received power (i.e. the SNR), the higher the RMS delay spread which usually also results in error floors and in the increase of the (uncoded) BER (as seen on page 242 in [21]). Therefore, the maximal transmit power possibly may not guarantee the lowest (uncoded) BER in the

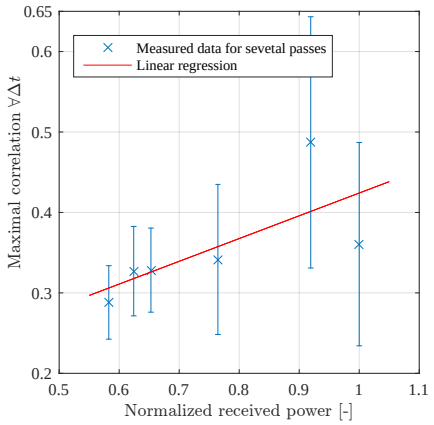

Fig. 7. Linear regression shows that the mean Pearson correlation coefficient (for all intended Δt) increases with the increase of the received power.

demonstrated scenario. In other words, for short distances, self-interference due to multipath components (MPCs) that fall outside the cyclic prefix or equalizer window might be the dominant effects of the characterized channels.

ACKNOWLEDGMENT

The research described in this abstract was financed by the Czech Science Foundation, Project No. 17-27068S, and by the National Sustainability Program under grant LO1401. For the research, the infrastructure of the SIX Center was used. The financial support by the Austrian Federal Ministry of Science, Research and Economy and the National Foundation for Research, Technology and Development is gratefully acknowledged. The work of AFM was supported by the California Transportation authority.

REFERENCES

[1] H. Meinel and A. Plattner, "Millimetre-wave propagation along railway lines," *IEE Proceedings F (Communications, Radar and Signal Processing)*, vol. 130, no. 7, pp. 688–694, 1983.

[2] T. S. Rappaport, S. Sun, R. Mayzus, H. Zhao, Y. Azar, K. Wang, G. N. Wong, J. K. Schulz, M. Samimi, and F. Gutierrez, "Millimeter wave mobile communications for 5G cellular: It will work!" *IEEE Access*, vol. 1, pp. 335–349, 2013.

[3] T. S. Rappaport, Y. Xing, G. R. MacCartney, A. F. Molisch, E. Mellios, and J. Zhang, "Overview of millimeter wave communications for fifth-generation (5G) wireless networks—with a focus on propagation models," *IEEE Transactions on Antennas and Propagation*, no. 12, pp. 6213–6230, 2017.

[4] H. Wang, X. Yin, X. Cai, H. Wang, Z. Yu, and J. Lee, "Fading characterization of 73 GHz millimeter-wave V2V channel based on real measurements," in *Communication Technologies for Vehicles*, J. Moreno García-Loygorri, A. Pérez-Yuste, C. Briso, M. Berbineau, A. Pirovano, and J. Mendizábal, Eds., Cham: Springer International Publishing, 2018, pp. 159–168.

[5] K. Akihito, S. Katsuyoshi, M. Fujise, and S. Kawakami, "Propagation characteristics of 60-GHz millimeter waves for ITS inter-vehicle communications," *IEICE Transactions on Communications*, vol. 84, no. 9, pp. 2530–2539, 2001.

[6] K. Sarabandi, E. S. Li, and A. Nashashibi, "Modeling and measurements of scattering from road surfaces at millimeter-wave frequencies," *IEEE Transactions on Antennas and Propagation*, vol. 45, no. 11, pp. 1679–1688, 1997.

[7] A. Yamamoto, K. Ogawa, T. Horimatsu, K. Sato, and M. Fujise, "Effect of road undulation on the propagation characteristics of inter-vehicle communications in the 60 GHz band," in *Proc. of IEEE/ACES International Conference on Wireless Communications and Applied Computational Electromagnetics*, 2005, pp. 841–844.

[8] J. Blumenstein, A. Prokes, J. Vychodil, M. Pospisil, and T. Mikulasek, "Time-varying K factor of the mm-wave vehicular channel: Velocity, vibrations and the road quality influence," in *IEEE 28th PIMRC*, 2017.

[9] J. Blumenstein, J. Vychodil, M. Pospisil, T. Mikulasek, and A. Prokes, "Effects of vehicle vibrations on mm-wave channel: Doppler spread and correlative channel sounding," in *IEEE 27th PIMRC*, 2016, pp. 1–5.

[10] Y. Wang, K. Venugopal, A. F. Molisch, and R. W. Heath, "Mmwave vehicle-to-infrastructure communication: Analysis of urban microcellular networks," *IEEE Transactions on Vehicular Technology*, vol. 67, no. 8, pp. 7086–7100, Aug. 2018.

[11] J. Blumenstein, A. Prokes, J. Vychodil, T. Mikulasek, J. Milos, E. Zöchmann, H. Groll, C. F. Mecklenbräuker, M. Hofer, D. Löschenbrand, L. Bernadó, T. Zemen, S. Sangodoyin, and A. Molisch, "Measured high-resolution power-delay profiles of nonstationary vehicular millimeter wave channels," in *IEEE 29th PIMRC*, Sep. 2018.

[12] E. Zöchmann, M. Hofer, M. Lerch, S. Pratschner, L. Bernadó, J. Blumenstein, S. Caban, S. Sangodoyin, H. Groll, T. Zemen, A. Prokeš, M. Rupp, A. F. Molisch, and C. F. Mecklenbräuker, "Position-specific statistics of 60 GHz vehicular channels during overtaking," *IEEE Access*, pp. 14 216–14 232, 2019.

[13] A. Prokes, J. Vychodil, T. Mikulasek, J. Blumenstein, E. Zöchmann, H. Groll, C. F. Mecklenbräuker, M. Hofer, D. Löschenbrand, L. Bernadó, T. Zemen, S. Sangodoyin, and A. Molisch, "Time-domain broadband 60 GHz channel sounder for vehicle-to-vehicle channel measurement," in *2018 IEEE Vehicular Networking Conference (VNC)*, Dec. 2018, pp. 1–7.

[14] T. Mikulasek, J. Lacik, and Z. Raida, "SIW slot antennas utilized for 60-GHz channel characterization," *Microwave and Optical Technol. Lett.*, vol. 57, no. 6, pp. 1365–1370, 2015.

[15] T. Mikulasek, J. Blumenstein, and A. Prokes, "Antennas utilized for intra-vehicle 3–11 GHz and 55–65 GHz channel measurement," in *2016 Progress in Electromagnetic Research Symposium (PIERS)*, Aug. 2016, pp. 4258–4262.

[16] F. Hlawatsch and G. Matz, *Wireless communications over rapidly time-varying channels*. Academic Press, 2011.

[17] M. Golay, "Complementary series," *IRE Transactions on Information Theory*, vol. 7, no. 2, pp. 82–87, Apr. 1961.

[18] R. J. Polge and E. M. Mitchell, "Impulse response determination by cross correlation," *IEEE Transactions on Aerospace and Electronic Systems*, vol. AES-6, no. 1, pp. 91–97, 1970.

[19] J. Vychodil, M. Pospisil, A. Prokes, and J. Blumenstein, "Millimetre wave band time domain channel sounder," *IET Communications*, vol. 13, no. 3, pp. 331–338, 2019.

[20] "LPRO rubidium oscillator for time and frequency reference. user's guide and integration guidelines," Datum Irvine, Tech. Rep., 2000.

[21] A. F. Molisch, *Wireless communications*. 2nd ed., Wiley - IEEE Press, 2011.

[22] J. Blumenstein, A. Prokes, A. Chandra, T. Mikulasek, R. Marsalek, T. Zemen, and C. Mecklenbrauker, "In-vehicle channel measurement, characterization, and spatial consistency comparison of 3-11 GHz and 55-65 GHz frequency bands," *IEEE Transactions on Vehicular Technology*, vol. 66, no. 5, pp. 3526–3537, May 2017.

[23] L. Bernadó, T. Zemen, F. Tufvesson, A. F. Molisch, and C. F. Mecklenbräuker, "Delay and doppler spreads of nonstationary vehicular channels for safety-relevant scenarios," *IEEE Trans. Veh. Technol.*, vol. 63, no. 1, pp. 82–93, 2014.

9 MULTIPATH PROPAGATION ANALYSIS FOR VEHICLE-TO-INFRASTRUCTURE COMMUNICATION AT 60 GHZ

This chapter is a postprint version of the following published paper:

A. Prokes, J. Blumenstein, **J. Vychodil**, T. Mikulasek, R. Marsalek, E. Zöchmann, H. Groll, C. F. Mecklenbräuker, T. Zemen, A. Chandra, H. Hammoud, and A. F. Molisch, "Multipath Propagation Analysis for Vehicle-to-Infrastructure Communication at 60 GHz," in *2019 IEEE Vehicular Networking Conference (VNC)*, 2019, pp. 1–8.

Author of this thesis contribution

This paper also describes another more advanced measurements that were done using the channel sounder in its (so far) final state. The author of this thesis was in charge of building the measurement workplace, controlling the instruments and the fundamental data processing.

Multipath Propagation Analysis for Vehicle-to-Infrastructure Communication at 60 GHz

Ales Prokes[*], Jiri Blumenstein[*], Josef Vychodil[*], Tomas Mikulasek[*], Roman Marsalek[*],
Erich Zöchmann[†‡*], Herbert Groll[‡], Christoph F. Mecklenbräuker[‡],
Thomas Zemen[x], Aniruddha Chandra[ɬ], Hussein Hammoud[††], Andreas F. Molisch[††]

[*]Department of Radio Electronics, Brno University of Technology, Czech Republic, prokes@vutbr.cz
[†] Christian Doppler Laboratory for Dependable Wireless Connectivity for the Society in Motion
[‡] Institute of Telecommunications, TU Wien, Austria
[x] Safety and Security Department, Austrian Institute of Technology, Austria
[ɬ]National Institute of Technology, Department of Electronics and Communication Engineering, India
[††] Wireless Devices and Systems Group, University of Southern California, USA

***Abstract*— The paper deals with an analysis of multipath propagation environment in the 60 GHz band using a pseudo-random binary sequence-based time-domain channel sounder with 8 GHz bandwidth. The main goal of this work is to analyze the multipath components (MPCs) propagation between a moving car carrying a transmitter with an omnidirectional antenna and a fixed receiver situated in a building equipped with a manually steered directional horn antenna. The paper briefly presents the time dependence of the dominant MPC magnitudes, shows the effect of the surrounding vegetation on the RMS delay spread and signal attenuation, and statistically evaluates the reflective properties of the road which creates the dominant reflected component. To understand how the MPCs propagate through the channel we measured and analyzed the power and the RMS delay spread distributions in the static environment surrounding the car using an automated measuring system with a controlled receiver antenna tracking system. We give some examples of how the MPC magnitudes change during the antenna tracking and demonstrate that a building and a few cars parked close to the measuring car create a lot of MPCs detectable by the setup with a dynamic range of about 50 dB.**

Keywords—millimeter wave, channel measurement, channel sounder, channel impulse response, delay spread.

I. INTRODUCTION

Automated driving systems of future vehicles will be much more reliable and safer when employing inter-vehicular communication [1]. Being able to disseminate information on safety-critical events detected or caused by individual participants in the traffic with other relevant traffic members is for sure beneficial not only in terms of safety, but also in terms of traffic flow and overall smoothness of the transportation process. The vehicle-to-vehicle communication (V2V) had been previously studied for various sub-6 GHz frequency bands [2]; however, it is tempting to utilize specific parts of a much higher frequency band designated as the millimeter wave (MMW) band, which spans the frequency range 30–300 GHz. Many studies consider especially the frequency band around 60 GHz because the International Telecommunication Union (ITU) assigns the 60 GHz band to the Industrial, scientific and medical (ISM) bands allowing license-free operations and offers several GHz of bandwidth, which is unheard of in the mentioned sub-6 GHz band [3].

It needs to be mentioned that the 60 GHz band for vehicular connectivity had been studied several decades earlier, see e.g. [4], however, in a very narrowband setup leading to the fact that the extensive bandwidth, available in the already mentioned 60 GHz band, stayed unused. At present, as the advances in the monolithic microwave integrated circuitry (MMIC) have brought the attention of both the industrial and the scientific community again to the 60 GHz band, the V2V MMW communication is revisited, for example in [5]. The path-loss of the links at 60 GHz is of course still high due to the oxygen absorption in the atmosphere which reaches 15 dB/km; therefore, it is deemed suitable for short-range communication rather than for long-range backhauls [6]. The broadband V2V MMW communication is studied in [7] demonstrating exemplary power-delay profiles (PDPs), path-loss and root-mean-square (RMS) delay spreads of the radio channel between two oncoming vehicles. In [7], the information exchange is direct, without any intermediary. In this paper, we show another possible scenario termed vehicle-to-infrastructure (V2I), where the information from the individual vehicles is gathered by the (usually elevated) roadside infrastructure. Subsequently, the information might be backhauled to a distant area (e.g. in difficult non-line-of-sight situations (NLOS)) or transmitted back to other vehicles even in the vicinity of the original transmitter car. This relaying scenario might be beneficial due to the elevated installation of the roadside infrastructure, thus easing the issues of shadowing by other vehicles on the road [8].

In [9], the V2I scenario, where the transmitter and the receiver are not moving but the surrounding traffic on the two-lane road causes the time-varying nature of the channel, is analyzed. It is shown in [9] that the presence of moving vehicles, although making the channel non-stationary, may reduce the

RMS delay spread. This is due to the presence of cars, which effectively serve as artificial reflecting surfaces and thus increase the total received power.

In [10], the outage probability of MMW V2I propagation channels is researched with the conclusion that the two-wave Rice model is not necessary and "the road-reflected wave can be neglected in the numerical computations". The conclusions in [10] are based on a ray-tracing analytical channel model. On the other hand, however, based on the real-world channel sounding campaign in [5], a two-way diffuse power (TWDP) channel model is derived and validated via Akaike's information criterion. In [11], a small-scale fading model is derived for a V2I scenario similar to that in [5] and again, the TWDP statistics are confirmed. The two-way nature of the V2I MMW channel is also observed in this paper; however, here we show different statistical properties of the direct and the reflected components affected by the surrounding vegetation. Unlike other works, where the influence of vegetation is examined using a fixed measurement setup [12], [13], we show the influence of the surrounding trees during the movement of the car carrying the measurement setup transmitter. In another part of the paper we deal with the mutual dependence between the power and the RMS delay spread distributions, which is not a usually analyzed channel feature, but its knowledge could be very valuable.

With this background, the detailed contributions of this paper are as follows:

- Analysis of multipath components (MPCs) propagating between a moving car and a fixed receiver in terms of time dependence of direct and reflected MPCs magnitudes, RMS delay spread of the received MMW signal, and statistical characterization of the strongest reflected component.
- Examination of 2D power and the RMS delay spread distributions in a static rugged environment surrounding the car, and evaluation of their relationship.

The rest of the paper is organized as follows. Section II briefly describes the channel sounder. Section III informs about the measurement scenarios used for time-varying and static environments. Section IV deals with the real word measurements. Then in Section V, the analyses of both the time-varying and the static channels are presented. A summary of the paper is given in the conclusion.

II. Measurement Setup

The channel measurement was carried out using the 60 GHz time-domain channel sounder described in detail in [14]. It is composed of a pseudo-random binary sequence (PRBS) transmitter (TX) and a correlation receiver (RX). It employs Golay complementary sequences as the excitation PRBS signal, because of their very good correlation properties, minimal leakage effects caused by FFT [15], and a great ability to mitigate unwanted nonlinearity effects produced by channel sounder analog circuits [16]. The transmitter is based on an Anritsu MP1800A Signal Quality Analyzer working as a PRBS generator. The receiver is created using a Tektronix MSO72004C (20 GHz, 50 GS/s) Mixed Signal Oscilloscope working as a very fast analog-to-digital converter. The baseband

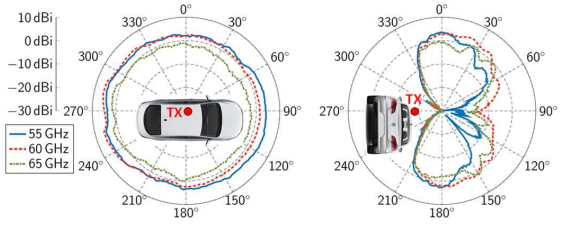

Fig. 1. E-plane (left) and H-plane (right) measured radiation pattern of double-sided SIW slot antenna at 55 GHz, 60 GHz, and 65 GHz.

PRBS signal is converted into the MMW band and back using SiversIma FC1000V series V-band up/down converters [17]. The channel sounder bandwidth is 8 GHz, the number of samples per measured channel impulse response (CIR) is set to N_{Sa} = 8092 and the number of saved CIRs per measurement is N_{CIR} = 932. Due to the correlation gain the sounder dynamic range is about 45 dB. In the case of static channel measurement, it can be increased by another 5–10 dB using an averaging technique. Downloading data from the oscilloscope to a PC, and their basic processing are controlled by LabView.

The transmitter was equipped with an omnidirectional SIW slot antenna described in [18], whose radiation pattern related to the car is shown in Fig. 1. An angle of 0° in both the E- and the H-plane corresponds to the left side of the car (as seen by the driver) and the car roof in the H-plane is situated at an angle of 270°. The MMW signal was received using a directional horn antenna with a dielectric lens. The antenna gain dependence on the angle is shown in Fig. 2.

All measured values mentioned below are related to the low noise MMW preamplifier output. The following down converter SiversIma then increases them by a gain of about 15–20 dB.

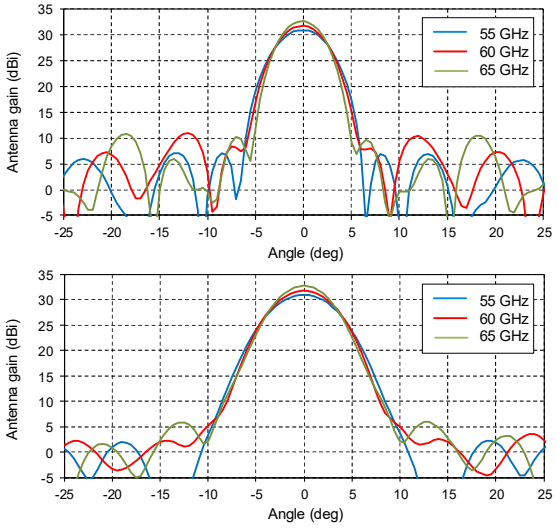

Fig. 2. E-plane (top) and H-plane (bottom) measured gain of horn antenna with dielectric lens at 55 GHz, 60 GHz, and 65 GHz.

III. Measurement Scenarios

All V2I measurements were performed in the Brno University of Technology campus between the building at Technicka 12 and a VW CC car driving on the road in front of the building as shown in Fig. 3. The car was moving in both directions at different speeds. In the text below, we will use the designation "Scenario 1a" for the direction of moving shown in Fig. 3 and "Scenario 1b" for the opposite direction of the car movement. Since the measured results contained several multipath components whose origin was ambiguous, we made further stationary measurements in order to be able to correctly interpret the measured data. In "Scenario 2" the car was situated in front of the building and the channel was scanned by the horn antenna directed to uniformly distributed points as shown in Fig. 4. To determine the direction of propagation of certain MPCs, the TX antenna was in a few measurements shielded towards the receiver by an MMW absorber as shown in the upper left corner.

In all the scenarios the transmitter was situated in the car and its antenna together with the power amplifier and cooler were placed on the car roof as shown in Fig. 5 (left). The receiver was situated in a room on the 6th floor of the university building. In Scenarios 1a and 1b the RX antenna was mounted on a photographic gimbal head and tripod and directed out of an open window (see Fig. 5 (middle)). The antenna was manually directed to the moving car using a riflescope. This manual tracking of the directional antenna simulates electronic beam steering of an antenna array assumed for 5G wireless networks [19]. The correctness of the RX horn antenna alignment during the tracking was checked using a video recorded by a camera mechanically coupled to the antenna. In Scenario 2 the RX antenna was directed using a motorized Sky-Watcher AllView mount (see Fig. 5 (right)) controlled by PC and LabView.

For Scenarios 1a and 1b the car speed was chosen $v = 30$ km/h to 50 km/h. As shown in Fig. 3, the height of the TX and RX antennas above the ground is $h = 1.55$ m and $H = 14.5$ m respectively. It is obvious that for Scenario 1a, where the distance between the TX antenna and the building is $D = 28.5$ m, the propagation distance between the antennas is $L = \sqrt{(H-h)^2 + D^2} = 31.3$ m. Similarly, for Scenario 1b, where D is only 25 m because the car goes on the roadside closer to the building, we can get $L = 28$ m.

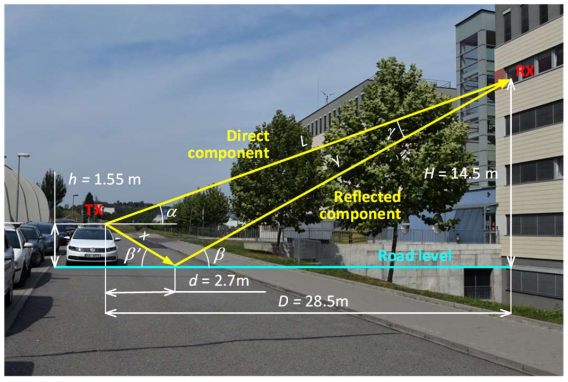

Fig. 3. Measuring workplace in the university campus at Technická 12, Brno.

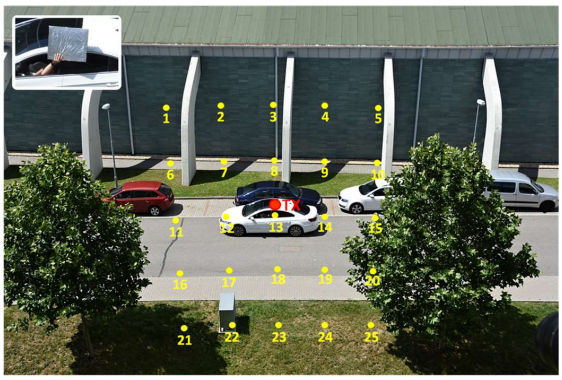

Fig. 4. Distribution of the measurement points for CIR evaluation.

IV. Measurement

For all the car speeds and directions, we had performed three measurements and then we selected the measurement where the car tracking was the most accurate. Note that the tracking of a moving car is not easy especially at higher speeds. The magnification of the telescope must not be too high, as it must allow the car to be quickly found. In such a case, the transmitter is too small for watching. Thus, in most cases the RX antenna was directed to the car center, which caused a relatively small constant vertical angular error. In contrast, the variable angular velocity of the car (observed from the perspective of the receiver) complicated the tracking of the car and, as a result, caused a time-varying horizontal angular error. Overall, the selected measurements exhibit vertical and horizontal errors of less than 2° and 3° respectively. Examples of measured CIRs for Scenario 1a, are shown in Fig. 6, where for a clearer interpretation of the results we used the propagation distance at the vertical axis instead of the more common time or delay.

First, we chose a long period of CIRs measurement $T_{CM} = 5$ ms to be able to observe changes in the MPCs and the influence of surrounding trees on signal propagation. The corresponding total measurement time $T_{TM} = T_{CM} \times N_{CIR}$ was 4.675 s. Further, to analyze the influence of the road roughness on the MMW signal reflection during the car movement we set the measurement period to $T_{CM} = 200$ µs which gives the total measurement time $T_{TM} = 0.186$ s. For $v = 50$ km/h ($v = 14$ m/s) the CIRs are taken every $v \times T_{CM} = 2.8$ millimeters of the car movement.

Fig. 5. From left to right: placement of TX antenna on the car roof, RX antenna on the gimbal head and on the motorized mount.

It is obvious that in both cases there are two dominant components: a direct component (the stronger and nearer one) and a reflected component. To find a reflective spot, we parked the car at the position shown in Fig. 4 and placed the MMW absorber on the road, sidewalk and various parts of the car. We observed that this component was reflected off the road at about 2.7 meters from the car as shown in Fig. 3. The difference between the direct and reflected path lengths $\Delta L = x + y - L = \sqrt{d^2 + h^2} + \sqrt{(D-d)^2 + H^2} - L$ is then 1.4 m, which corresponds to the measured difference shown in Fig. 6. The angle between the direct component and the reflected component is $\gamma = 4.95°$. It is given by $\gamma = \beta - \alpha = \text{arctg}[H/(D-d)] - \text{arctg}[(H-h)/D]$. Note that the angles β and β' slightly differ because the road is not perfectly even. As the maximum measurable distance of the channel sounder is 49 m [14], the multipath components propagating over a longer distance (reflected multiple times from the building behind the car) are aliased as shown in Fig. 6. The white dashed curves approximate the maximum MPCs position (see Section V-A). The measurements were made so that the center of records corresponded to the moment when the transmitter and the receiver were both in a vertical plane perpendicular to the building wall. Different distances at the beginning and the end of record shown in Fig. 6 (top) are caused by an imperfect parallelism of the road and the building.

In Scenario 1b, when the car was moving in the opposite direction, the data records are very similar to those shown in Fig. 6, but there is no component reflected from the road since the road and the sidewalk were shadowed by the car roof.

Scenario 2 measurements were performed for several car positions. The most interesting measurement (the richest in MPC components) is shown in Fig. 4. To get information about the MPCs power distribution in 2D plane we used the motorized mount and scanned the space around the transmitter in rectangular coordinates with horizontal and vertical steps of 5°. Since the measurement setup was working in the same way as in Scenario 1 but it recorded only 100 CIRs for any measurement point, we averaged them to increase the signal to noise ratio (SNR). We evaluated the power at all points by summing the CIR peaks above the noise floor, which was set to –60 dBV. A smooth representation of the distribution, shown in Fig. 7, was achieved by interpolating the values by a ratio of 32. The elongated shape in the vertical direction is caused by strong MPCs reflected by the car and the building behind the transmitter and by the road. Of non-negligible influence are also the different beam-widths of the RX antenna in the vertical and the horizontal axes as shown in Fig. 2.

V. Channel Characterization

As mentioned above the aim of this work is to analyze the time varying MPC characteristics caused by a moving car such as MPC magnitude variation in time, its statistical properties, and the time variation of the delay spread. Another research goal is to analyze the power and RMS delay spread distributions in a static environment surrounding the car and to find any dependence between them. So, we can divide the channel characterization into two subsections devoted to the time-varying and the static channels.

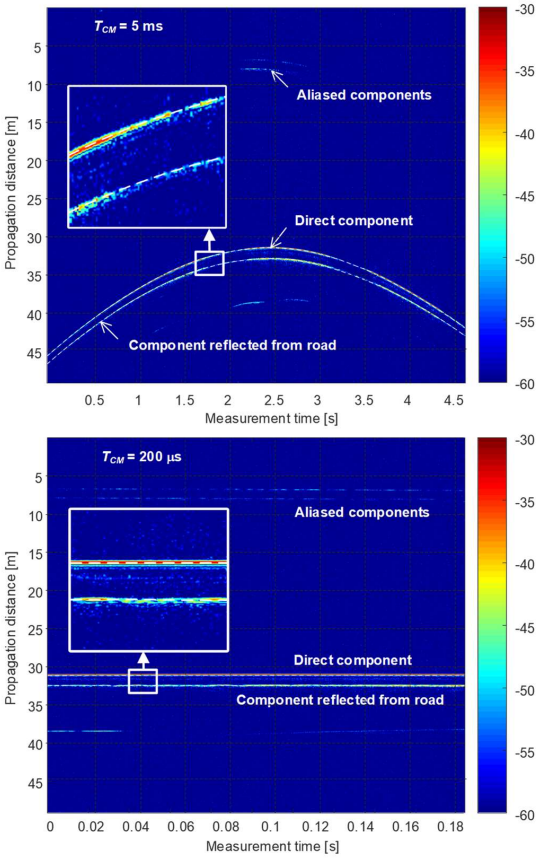

Fig. 6. The CIR magnitude in dBV measured in Scenario 1a with sampling periods T_{CM} = 5 ms (top) and and T_{CM} = 200 µs (bottom), v = 40 km/h.

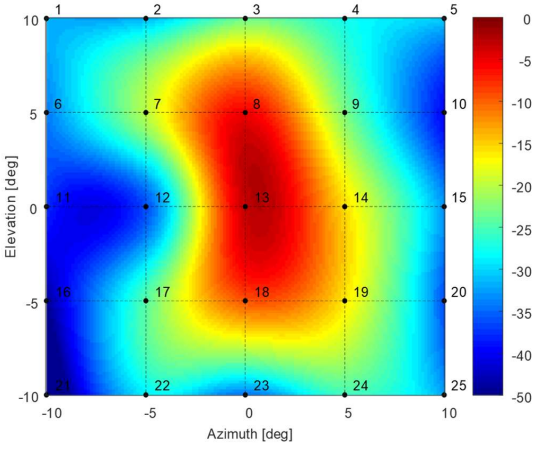

Fig. 7. Distribution of the power normalized to 0 dB in the vinicity of the car.

A. *Analysis of time-varying channel*

To analyze the MPCs magnitude variation we approximated the coordinates (indices) of direct and reflected components by a smooth curve as shown in Fig. 6. It was accomplished by the following three steps:

1. Detecting the strongest and the second strongest component (i.e. the direct component and the component reflected from the road) in each CIR record and determining their coordinates.
2. Filtering the coordinates by a Hampel filter to remove outliers (coordinates of the other strong components not belonging to the two above).
3. Filtering the coordinates using a Savitzky-Golay FIR filter to obtain a smooth approximation.

The Hampel filter is a configurable-width sliding window filter, calculating for each window the median and the standard deviation σ. If any point in the window is more than $n\sigma$ out of the median, where n is a user-definable value (default n = 3), then the Hampel filter identifies this point as an outlier and replaces it with the median. Compared with a simpler median filter the Hampel filter is defined by another parameter ($n\sigma$), which improves the filter configurability and offers better fitting. Both the window length and n were set empirically.

The Savitzky-Golay filter is a frequently used smoothing filter based on local least-squares polynomial approximation. The filter is defined by the polynomial order and by the approximation interval. Optional parameters implemented in MATLAB, which was used for simulations, are positive-valued weights used during the least-squares minimization. Thanks to many configurable parameters, it can be very well optimized for the desired approximation. The filter is necessary to approximate the signal tendency when its magnitude is strongly attenuated (for example when the signal penetrates trees) and when the Hampel filter does not give a satisfactory result. In fact, both filters represent the momentum of the car and smooth the curves representing the distance change.

The time dependence of the direct and reflected component magnitudes depicted in Fig. 6 (top) plotted for the fitted coordinates is shown in Fig. 8 (grey waveforms). The time dependence of the direct component obtained in Scenario 1b is then shown in Fig. 9. The short-term trends (black and red dashed waveforms) were obtained by lowpass zero-phase bidirectional filtering, where the data is processed in both the forward and the reverse directions, which does not shift the filtered signal in time.

The effect of trees in Figs 8 and 9 is obvious. The attenuation varies in a wide range, depending on which part of treetops the MMW signal penetrates. Its maximum is slightly above 30 dB. Note that the difference in the magnitudes between the direct and the reflected component in Scenario 1a is relatively small. In the "unshaded" record segments the short-term trends differ between 6–12 dB. As mentioned above it is caused partly by pointing the traced RX antenna at the car doors.

The ripple of the direct component magnitude in the unshaded areas is probably due to imperfect manual tracking and angle-dependent irradiation of both the antennas. As is obvious

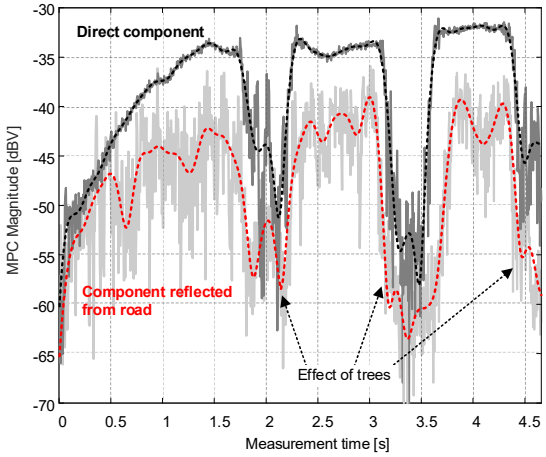

Fig. 8. The time dependence of the direct and reflected component magnitudes measured in Scenario 1a for T_{CM} =5 ms and v=40 km/h.

from Fig. 2, the angular error of 3° mentioned in Section IV causes an RX antenna gain drop in the E-plane of about 4 dB, which corresponds to the direct component magnitude variation. The ripple of the reflected component magnitude is additionally affected by road irregularities. Note that the bottom parts of component magnitudes are also affected by the measurement setup noise.

The effect of the road on a reflected component is also obvious in Fig. 10, where the component magnitudes depicted in Fig. 6 (bottom) are plotted. While the small changes in the direct component magnitude are caused by the receiver noise, downconverter IQ imbalance, and possibly by the phase noise of the reference rubidium oscillators, the larger variation of the reflected component is caused predominantly by the rough road surface (flat asphalt). To confirm this, one measurement was performed with the stationary vehicle and compared with all the time-varying channel measurements (made at different speeds) with respect to the reflected component magnitude variance. The reflected component for the stationary car is shown in Fig. 10 (blue waveform). It can be concluded that the influence of receiver noise is small as the variance (normalized power in W) of the reflected component measured for a stationary car is 2.08e–07 while the variance of the reflected component measured for a moving car is in the interval from 2.30e–05 to 7.85e–06. Note that the direct component variance in the static measurement is 2.10e–07.

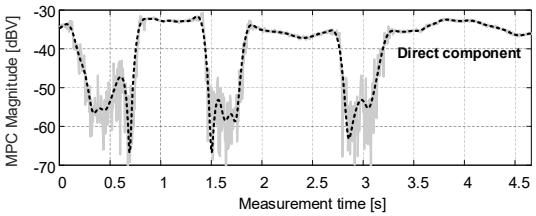

Fig. 9. The time dependence of the direct component magnitudes measured in Scenario 1b for T_{CM} = 5 ms and v = 40 km/h.

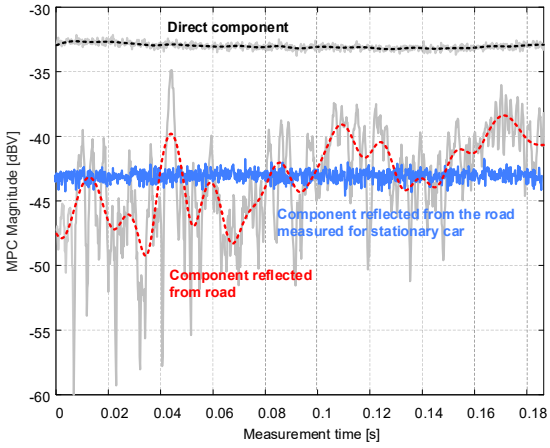

Fig. 10. The time dependence of the direct and reflected component magnitudes measured in Scenario 1a. T_{CM} = 200 µs, v = 40 km/h.

Another aim of the channel characterization was to fit the distribution of the reflected component magnitudes measured for T_{CM} = 200 µs by a proper probability density function (PDF). It was found that the best fitting can be obtained by a *generalized extreme value* (GEV) distribution given by the location parameter μ, scale parameter σ, and shape parameter $k \neq 0$. For all (four) unfiltered datasets we defined intervals for the above parameters: $\mu \in \langle 4.4\text{ mV}, 5.8\text{ mV} \rangle$, $\sigma \in \langle 2.3\text{ mV}, 4.0\text{ mV} \rangle$, and $k \in \langle -0.055, -0.108 \rangle$. No relationship between the amplitude distribution and the speed of the vehicle was found. The PDF calculated as a histogram, and the cumulative distribution function (CDF) of the reflected component depicted in Fig. 10 (gray waveform), fitted by the GEV distribution are shown in Fig. 11. Note that when the short-term filtered trend (red curve) is subtracted from an unfiltered record (gray waveform) the result can be successfully fitted with the normal distribution. In other words, the effect of small particles in asphalt can be fitted by a normal distribution.

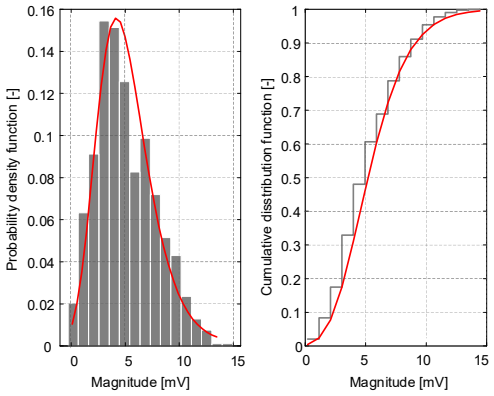

Fig. 11. PDF (left) and CDF (right) calculated and fitted by generalized extreme value distribution for the component reflected from the road.

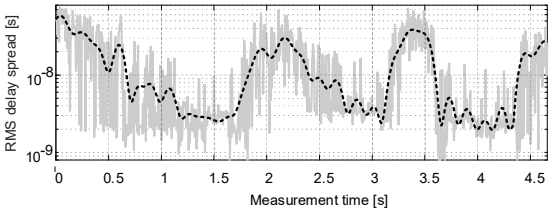

Fig. 12. The time dependence of the instantaneous RMS delay spread for T_{CM} = 5 ms and v = 40 km/h.

Finally, we calculated the instantaneous RMS delay spread for the components depicted in Fig. 6 (top) according to [20]

$$\sigma_{\tau,t} = \left[\frac{\sum_{i=1}^{L} |h(\tau_i,t)|^2 \tau_i^2}{\sum_{i=1}^{L} |h(\tau_i,t)|^2} - \frac{\left(\sum_{i=1}^{L} |h(\tau_i,t)|^2 \tau_i\right)^2}{\left(\sum_{i=1}^{L} |h(\tau_i,t)|^2\right)^2} \right]^{\frac{1}{2}}, \quad (1)$$

where $|h(\tau_i, t)|$ are the magnitudes of CIR taps at the delay τ_i, t is the measurement time (capturing time of CIRs), and L is the number of taps. The number of taps was chosen experimentally as the number of the CIR peaks exceeding the receiver noise threshold (–60 dBV). The RMS delay spread plotted in the logarithmic vertical scale is shown in Fig. 12. It corresponds well to the magnitudes in Fig. 8. The range of averaged values (black dashed waveform) between 2 ns (line-of-sight (LOS) propagation) and 60 ns (shadowing by trees) are typical of outdoor V2X scenarios [21]. By applying FFT to the complex values of the component reflected from the road we found that at speeds of up to 50 km/h, the significant components do not exceed the 600 Hz as evident from Fig. 13.

B. Analysis of static channel

The aim of the static channel analysis is to find how some MPCs propagate through the channel in order to correctly interpret the data measured and to find some dependence between the received signal power and the RMS delay spread. For this purpose, we first calculated the power distribution in the car vicinity as mentioned above and shown in Fig. 7, and then evaluated the RMS delay spread for all the measured points according to (1). A map of the RMS delay spread distribution is shown in Fig. 14. It is evident that the minimum value occurs very close to the transmitter (point 13), due to the dominant direct component. The relatively low delay spread at points 8, 12, 14 and 18 is caused by the presence of direct component and either strong MPCs traveling close to the direct component (reflected from the road) or weak MPCs traveling far from the direct component (e.g. reflected from the building behind the transmitter).

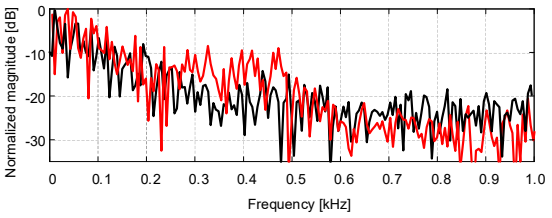

Fig. 13. Spectrum of reflected component measured in Scenario 1a for T_{CM} = 200 µs and the car speed v = 40 km/h (black) and v = 50 km/h (red).

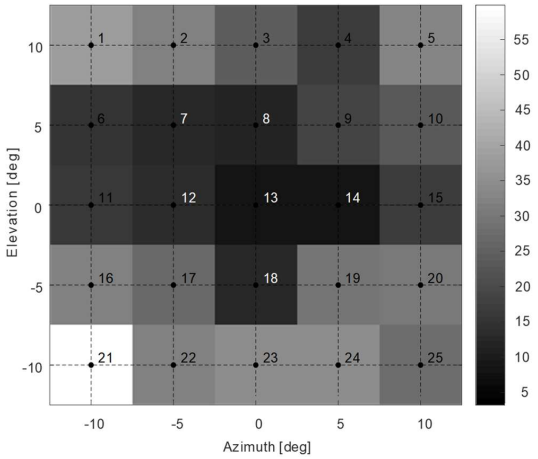

Fig. 14. Map of RMS delay spread in nanoseconds calculated for a set of CIRs measured in the vinicity of the car.

The CIRs corresponding to points 13 and 18 are shown in Fig. 15. The black waveforms were measured without the MMW absorber and the red waveforms were obtained with the absorber shielding the TX antenna. The blue circles indicate the values used for the RMS delay spread calculation. It is obvious that the component C was reflected from the building behind the transmitter, because it was also received with the absorber and its distance from the component A corresponds to twice the propagation path length between the building and the car. On the contrary the component D propagated towards the receiver and it was probably reflected multiple times. The vertical angular difference of 5° between the points 13 and 18 causes noticeable changes in the direct component A (13 dB) and in the component reflected from the road (7 dB). This unequal difference in the changes is due to the angle-dependent RX antenna gain and the deviation of the position of central point 13 and the transmitter as shown in Fig. 4.

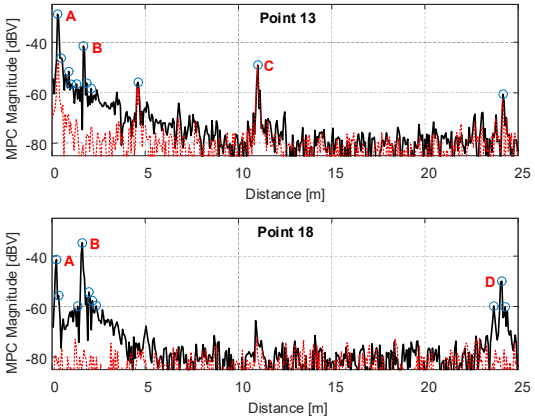

Fig. 15. The CIRs obtained at points 13 and 18 without (black) and with (red) absorber.

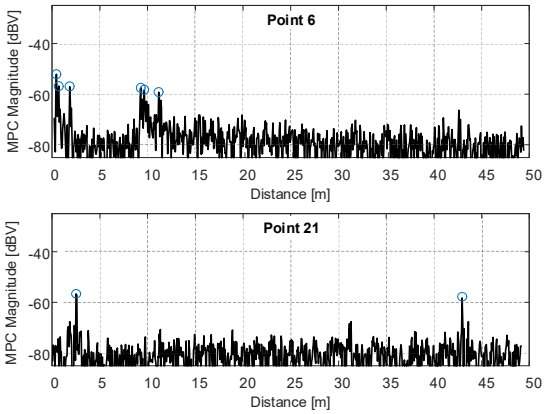

Fig. 16. The CIRs obtained at the edge points 6 and 21.

The averaging effect implemented in this measurement increases the dynamic range and allows detecting many weak MPCs. Thanks to it we can evaluate the RMS delay spread also for the edge points (far from the transmitter). An example of the CIRs measured for the edge points with the highest and the lowest RMS delay spread is shown in Fig. 16. The highest RMS delay spread at point 21 is caused by a two very distant peaks with similar power.

To find some relation between the received signal power and the RMS delay spread depicted in Figs 7 and 14 we plotted them in Fig. 17 for all the measured points arranged in a row. As expected, a small delay spread corresponds to a large received power. However, in a few cases this claim is not valid (see e.g. points 5 and 6), and, as is obvious there is no easily describable dependence between them because different RMS delay spread values correspond to the same power (points 6 and 23, or 12 and 20). Note that in the case of the RX antenna with a broader beam-width the RMS delay spread would be probably higher.

VI. Conclusion

We analyzed the multipath components propagation between a moving car on a road and a fixed receiver situated in a campus building. We showed very good reflective properties of the asphalt surface and demonstrated them by the small difference between the direct and the reflected component magnitudes varying between 6–16 dB (see Fig. 8 and Fig. 10).

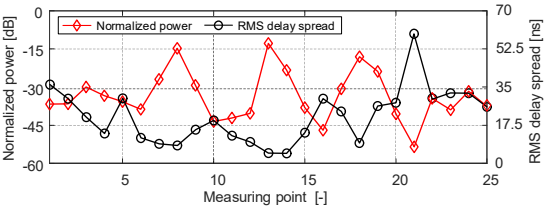

Fig. 17. Normalized power and RMS delay spread plotted for all points.

Similar small difference lower than 12 dB can also be observed between these components in “static scenario” (Fig. 15). Then we examined the attenuation caused by trees. We discovered that it varies in a wide range and its maximum for all the measurements slightly exceeds the value 30 dB. The time variation of the reflected component magnitude was fitted by a *generalized extreme value* distribution and the marginal values of the distribution parameters were calculated for all the measurements. For “moving scenario” we then evaluated the time dependence of the RMS delay spread. We proved that its averaged values (trends) vary in the range from 2 ns (obtained for obstructed LOS propagation) to 60 ns (obtained for the case the signal shadowed by trees). Finally, we calculated the spectrum of the component reflected from the road and discovered that at speeds of up to 50 km/h, there are no significant components above 600 Hz.

To understand how the MPCs propagate through the channel we measured and analyzed the power and the RMS delay spread distributions in the static environment surrounding the car. We obtained very similar values of the RMS delay spread between 4 and 58 ns as in the case of the previous time-varying channel analysis. We justified these values by analyzing the multipath component in the corresponding CIRs. Finally, by analyzing the 2D power and the RMS delay spread distribution we came to the conclusion that there is no provable relationship between them. By the results presented we generally demonstrate that a building and a few cars parked close to the measuring car create an environment relatively rich in multipath components.

We are aware of the manual antenna tracking imperfection which affects the above analyses. On the other hand, an estimated magnitude measurement error of up to 4 dB is not crucial. Note that another 1–2 dB magnitude change is produced by the non-uniform TX antenna irradiation. Simulation of any future real MMW system in order to get realistic results is very difficult, because the parameters of its antenna systems (antenna arrays) are not exactly known and their radiation pattern will probably have also some imperfections. In addition, the results are strongly dependent on the surrounding environment (road type, size of trees, number and types of nearby cars etc.). Thus, the presented work shows channel behavior only for specific scenarios. To eliminate the above error, we plan to use for future measurements an automated tracking system based on a camera, vision RoboRealm software, and the above-mentioned motorized Sky-Watcher AllView mount.

ACKNOWLEDGMENT

The research described in this paper was financed by the Czech Science Foundation, Project No. 17-27068S, by the National Sustainability Program under grant LO1401 and by the California Transportation Authority under the METRANS program. For the research, the infrastructure of the SIX Center was used.

REFERENCES

[1] C. Sommer and F. Dressler, Vehicular networking, Cambridge University Press, 2015.

[2] C. F. Mecklenbrauker et al., "Vehicular Channel Characterization and Its Implications for Wireless System Design and Performance, " *Proceedings of the IEEE*, July 2011.

[3] ITU, “Radio Regulations, Section IV. Radio Stations and Systems – Article 1.15, definition: Industrial, scientific and medical (ISM) applications (of radio frequency energy)”.

[4] H. Meinel and A. Plattner, "Millimetre-wave propagation along railway lines," *IEE Proceedings F (Communications, Radar and Signal Processing)*, no. 130, p. 688–694, 1983.

[5] E. Zöchmann et al., "Position-Specific Statistics of 60 GHz Vehicular Channels During Overtaking," *IEEE Access*, vol. 7, pp. 14216–14232, 2019.

[6] M. Khatun, H. Mehrpouyan and D. Matolak, "60-GHz Millimeter-Wave Pathloss Measurements in Boise Airport," in *IEEE Global Conference on Signal and Information Processing (GlobalSIP)*, pp. 1276–1280, 2018.

[7] J. Blumenstein, et al., "Vehicle-to-Vehicle Millimeter-Wave Channel Measurements at 56-64 GHz," in *IEEE Vehicular Technology Fall Conference (VTC-Fall)* (accepted for publication), Honolulu, pp. 1–4, 2019.

[8] M. G. Nilsson, D. Vlastaras, T. Abbas, B. Bergqvist and F. Tufvesson, "On multilink shadowing effects in measured V2V channels on highway," in *9th European Conference on Antennas and Propagation (EuCAP)*, Lisbon, 2015.

[9] J. Blumenstein et al., "Measured High-Resolution Power-Delay Profiles of Nonstationary Vehicular Millimeter Wave Channels," in *IEEE 29th Annual International Symposium on Personal, Indoor and Mobile Radio Communications (PIMRC)*, Bologna, 2018.

[10] R. Verdone, "Outage probability analysis for short-range communication systems at 60 GHz in ATT urban environments," *IEEE Transactions on Vehicular Technology*, vol. 46, no. 4, pp. 1027–1039, 1997.

[11] E. Zöchmann, J. Blumenstein, R. Marsalek, M. Rupp, K. Guan: "Parsimonious Channel Models for Millimeter Wave Railway Communications", in *IEEE Wireless Communications and Networking Conference (WCNC)*, 2019, pp. 1 - 6.

[12] T. S. Rappaport and S. Deng, "73 GHz wideband millimeter-wave foliage and ground reflection measurements and models," in *2015 IEEE International Conference on Communication Workshop (ICCW)*, London, 2015, pp. 1238-1243.

[13] N. C. Rogers et al., "A generic model of 1-60 GHz radio propagation through vegetation," Final Report Radio Agency, UK, 2002.

[14] A. Prokes et al., "Time-Domain Broadband 60 GHz Channel Sounder for Vehicle-to-Vehicle Channel Measurement," in *2018 IEEE Vehicular Networking Conference (VNC)*, Taipei, Taiwan, 2018, pp. 1–7.

[15] R. Zetik, M. Kmec, J. Sachs, and R. S. Thomä, "Real-Time MIMO Channel Sounder for Emulation of Distributed Ultrawideband Systems," *Int. J. Antennas Propag*., vol. 2014, Article ID 317683, pp. 1–16, 2014.

[16] J. Vychodil, M. Pospisil, A. Prokes and J. Blumenstein, "Millimetre wave band time domain channel sounder," *IET Communications*, vol. 13, no. 3, pp. 331–338, 2019.

[17] FC1005V/00 V-band Converter with LO. [Online]. Available: https://www.siversima.com/wp-content/uploads/FC1005V00-Data-Sheet.pdf. [Accessed: 15- Jun- 2018].

[18] T. Mikulasek, J. Lacik, and Z. Raida, "SIW slot antennas utilized for 60-GHz channel characterization," *Microw Opt. Tech. Lett*., vol. 57, no. 6, pp. 1365–1370, 2015.

[19] S. Sun, T. S. Rappaport, R. W. Heath, A. Nix and S. Rangan, "Mimo for millimeter-wave wireless communications: beamforming, spatial multiplexing, or both?," *IEEE Communications Magazine*, vol. 52, no. 12, pp. 110–121, Dec. 2014.

[20] A. F. Molisch, "Statistical properties of the RMS delay-spread of mobile radio channels with independent Rayleigh-fading paths," *IEEE Transactions on Vehicular Technology*, vol. 45, no. 1, pp. 201-204, Feb. 1996.

[21] E. Ben-Dor, T. S. Rappaport, Y. Qiao and S. J. Lauffenburger, "Millimeter-Wave 60 GHz Outdoor and Vehicle AOA Propagation Measurements Using a Broadband Channel Sounder," in *IEEE Global Telecommunications Conference* (GLOBECOM), Kathmandu, 2011, pp. 1–6.

10 CONCLUSION

This thesis dealt with the problem of measuring the fast varying and diverse MMW automotive channels. After brief introduction, the current channel measuring techniques, which are typically not able to capture all of the MMW channel features, were presented in Chapter 1.

The goals were set in Chapter 2. Chapter 3 represented the core of the dissertation — it fulfilled the primary goal of building a channel sounding system suitable for the MMW channels. It thoroughly explains the development of the system, its hardware, methods, data processing, features and parameters. Great part of this chapter was dedicated to mitigating an issue, which arose during the system development. The dynamic range of the system was considerably limited by the spurs, that appeared in the measurement output. It turned out that it was caused by the non-linear components in the measurement chain and was significantly reduced by a careful analysis and choice of the probing signal. It was shown that the Golay pair and Golay pair with inverted polarity as probing signal exhibit superior performance in most of the cases. This was analysed and explained also theoretically exploiting signal properties such as higher order autocorrelation function.

Chapters 4, 5 and 6 presented the first experiments with the developed channel sounding system — measurement of the intra-car channel. Those chapters showed and analyzed the effects of vehicle vibrations (caused by e.g. running engine, audio system, movement of the persons inside or even by the ride of the vehicle) on the transmission channel.

Chapter 7 explained several improvements on the system — especially separating the transmitter and receiver, which led to greater freedom in the measurement scenarios. It also showed some examples of the V2V channel measurements. Chapters 8 and 9 presented measurements and analysis of the V2V and V2I channels, respectively.

To summarize, both of the goals set in Chapter 2 were accomplished. A measurement system with unique parameters (the primary goal) was built and presented in Chapter 3 and partially Chapter 7. The rest of the Chapters 4–9 fulfilled the secondary goal — they provided actual measurements of various scenarios with the developed system.

BIBLIOGRAPHY

[1] A. Chandra, J. Blumenstein, T. Mikulasek, J. Vychodil, M. Pospisil, R. Marsalek, A. Prokes, T. Zemen, and C. Mecklenbrauker, "CLEAN algorithms for intra-vehicular time-domain UWB channel sounding," in *Proceedings of the 5th International Conference on Pervasive and Embedded Computing and Communication Systems*. SCITEPRESS - Science and and Technology Publications, 2015-2-11, pp. 224–229. [Online]. Available: http://www.scitepress.org/DigitalLibrary/Link.aspx?doi=10.5220/0005323702240229

[2] A. Chandra, J. Blumenstein, T. Mikulášek, J. Vychodil, R. Maršálek, A. Prokeš, T. Zemen, and C. F. Mecklenbräuker, "Serial subtractive deconvolution algorithms for time-domain ultra wide band in-vehicle channel sounding," *IET Intelligent Transport Systems*, vol. 9, no. 9, pp. 870–880, 2015. [Online]. Available: https://ietresearch.onlinelibrary.wiley.com/doi/abs/10.1049/iet-its.2014.0287

[3] J. Vychodil, A. Chandra, T. Mikulasek, A. Prokes, and V. Derbek, "UWB time domain channel sounder," in *Proceedings of 25th International Conference RADIOELEKTRONIKA 2015*, 2015, pp. 268–271.

[4] A. Dezfooliyan and A. Weiner, "Evaluation of time domain propagation measurements of UWB systems using spread spectrum channel sounding," *Antennas and Propagation, IEEE Transactions on*, vol. 60, no. 10, pp. 4855–4865, Oct 2012.

[5] A. Durantini, W. Ciccognani, and D. Cassioli, "UWB propagation measurements by PN-sequence channel sounding," in *Communications, 2004 IEEE International Conference on*, vol. 6, June 2004, pp. 3414–3418 Vol.6.

[6] J. Keignart, C. Abou-Rjeily, C. Delaveaud, and N. Daniele, "UWB SIMO channel measurements and simulations," *Microwave Theory and Techniques, IEEE Transactions on*, vol. 54, no. 4, pp. 1812–1819, June 2006.

[7] J. Kivinen, "60-GHz wideband radio channel sounder," *IEEE Transactions on Instrumentation and Measurement*, vol. 56, no. 5, pp. 1831–1838, Oct 2007.

[8] S. Guillouard, G. E. Zein, and J. Citerne, "High time domain resolution indoor channel sounder for the 60 GHz band," in *1998 28th European Microwave Conference*, vol. 2, Oct 1998, pp. 341–344.

[9] R. Zetik, M. Kmec, J. Sachs, and R. S. Thoma, "Real-time mimo channel sounder for emulation of distributed ultrawideband systems," *International*

Journal of Antennas and Propagation, vol. 2014, p. 16, 2014. [Online]. Available: http://dx.doi.org/10.1155/2014/317683

[10] S. Ranvier, J. Kivinen, and P. Vainikainen, "Millimeter-wave MIMO radio channel sounder," *IEEE Transactions on Instrumentation and Measurement*, vol. 56, no. 3, pp. 1018–1024, June 2007.

[11] M. Schack, J. Jemai, R. Piesiewicz, R. Geise, I. Schmidt, and T. Kurner, "Measurements and analysis of an in-car UWB channel," in *Vehicular Technology Conference, 2008. VTC Spring 2008. IEEE*, May 2008, pp. 459–463.

[12] M. Schack, M. Jacob, and T. Kurner, "Comparison of in-car UWB and 60 GHz channel measurements," in *Antennas and Propagation (EuCAP), 2010 Proceedings of the Fourth European Conference on*, April 2010, pp. 1–5.

[13] K. Leechaikitjaroen, S. Promwong, P. Supanakoon, S. Chensirikul, and S. Kaewmechai, "Indoor measurement results of UWB impulse radio for shot-range wireless systems with RMS delay spread and path loss," in *Communications and Information Technology, 2005. ISCIT 2005. IEEE International Symposium on*, vol. 1, Oct 2005, pp. 684–688.

[14] L. Liu, Y. Wang, N. Zhang, and Y. Zhang, "UWB channel measurement and modeling for the intra-vehicle environments," in *Communication Technology (ICCT), 2010 12th IEEE International Conference on*, Nov 2010, pp. 381–384.

[15] J. Blumenstein, A. Prokes, A. Chandra, T. Mikulasek, R. Marsalek, T. Zemen, and C. Mecklenbraeuker, "In-vehicle channel measurement, characterization and spatial consistency comparison of 3-11 GHz and 55-65 GHz frequency bands," *IEEE Transactions on Vehicular Technology*, vol. PP, no. 99, pp. 1–1, 2016.

[16] E. Zochmann, C. F. Mecklenbräuker, M. Lerch, S. Pratschner, M. Hofer, D. Löschenbrand, J. Blumenstein, S. Sangodoyin, G. Artner, S. Caban, T. Zemen, A. Prokeš, M. Rupp, and A. F. Molisch, "Measured delay and doppler profiles of overtaking vehicles at 60 ghz," in *12th European Conference on Antennas and Propagation (EuCAP 2018)*, 2018, pp. 1–5.

[17] G. R. MacCartney and T. S. Rappaport, "A flexible millimeter-wave channel sounder with absolute timing," *IEEE Journal on Selected Areas in Communications*, vol. 35, no. 6, pp. 1402–1418, 2017.

[18] G. R. MacCartney, H. Yan, S. Sun, and T. S. Rappaport, "A flexible wideband millimeter-wave channel sounder with local area and nlos to los transition

measurements," in *2017 IEEE International Conference on Communications (ICC)*, 2017, pp. 1–7.

[19] E. Ben-Dor, T. Rappaport, Y. Qiao, and S. Lauffenburger, "Millimeter-wave 60 GHz outdoor and vehicle AOA propagation measurements using a broadband channel sounder," in *Global Telecommunications Conference (GLOBECOM 2011), 2011 IEEE*, Dec 2011, pp. 1–6.

[20] C. Anderson, T. Rappaport, K. Bae, A. Verstak, N. Ramakrishnan, W. Tranter, C. Shaffer, and L. Watson, "In-building wideband multipath characteristics at 2.5 and 60 ghz," in *Proceedings IEEE 56th Vehicular Technology Conference*, vol. 1, 2002, pp. 97–101 vol.1.

[21] D. Ferreira, R. F. Caldeirinha, and N. Leonor, "Real-time high-resolution radio frequency channel sounder based on the sliding correlation principle," *IET Microwaves, Antennas & Propagation*, vol. 9, no. 8, pp. 837–846, 2015. [Online]. Available: https://ietresearch.onlinelibrary.wiley.com/doi/abs/10.1049/iet-map.2014.0165

[22] E. Lemos Cid, M. Garcia Sanchez, and A. Vazquez Alejos, "High speed transmission at 60 ghz for 5g communications," in *2015 IEEE International Symposium on Antennas and Propagation USNC/URSI National Radio Science Meeting*, 2015, pp. 1007–1008.

[23] R. Müller, R. Herrmann, D. A. Dupleich, C. Schneider, and R. S. Thomä, "Ultrawideband multichannel sounding for mm-wave," in *The 8th European Conference on Antennas and Propagation (EuCAP 2014)*, 2014, pp. 817–821.

[24] *FC1003V/01 V-band Converter*, Sivers IMA AB. [Online]. Available: http://siversima.com/wp-content/uploads/FC1003V01-Data-Sheet.pdf

[25] T. Mikulasek, J. Blumenstein, and A. Prokes, "Antennas utilized for intra-vehicle 3-11 GHz and 55-65 GHz channel measurement," in *2016 Progress in Electromagnetic Research Symposium (PIERS)*, Aug 2016, pp. 4258–4262.

[26] *FC1005V/00 V-band Converter*, Sivers IMA AB. [Online]. Available: http://siversima.com/wp-content/uploads/FC1005V00-Data-Sheet.pdf

[27] C. Chen, *Signal Processing Handbook*, ser. Electrical and Computer Engineering. New York: Taylor & Francis, 1988. [Online]. Available: https://books.google.cz/books?id=10Pi0MRbaOYC

[28] J. McLaughlin and J. Raviv, "Nth-order autocorrelations in pattern recognition," *Information and Control*, vol. 12, no. 2, pp. 121 – 142, 1968. [Online]. Available: http://www.sciencedirect.com/science/article/pii/S0019995868902416

[29] L. G. Weiss, "Wavelets and wideband correlation processing," *IEEE Signal Processing Magazine*, vol. 11, no. 1, pp. 13–32, Jan 1994.

[30] G. Gong, F. Huo, and Y. Yang, "Large zero autocorrelation zones of Golay sequences and their applications," *IEEE Transactions on Communications*, vol. 61, no. 9, pp. 3967–3979, September 2013.

[31] H. Harada, Y. Toyozawa, M. Shigaki, H. Kashiwagi, and T. Yamaguchi, "Identification of nonlinear parameters by using m-sequence and harmonic probing method," *Journal of System Design and Dynamics*, vol. 2, no. 1, pp. 209–217, 2008.

[32] V. Kekatos, D. Angelosante, and G. B. Giannakis, "Sparsity-aware estimation of nonlinear volterra kernels," in *Computational Advances in Multi-Sensor Adaptive Processing (CAMSAP), 2009 3rd IEEE International Workshop on*, Dec 2009, pp. 129–132.

[33] H. Tsukino, H. Harada, Y. Toyozawa, H. Kashiwagi, and R. Ohtsubo, "Identification of nonlinear parameters by using low-pass filtered M-sequence," in *ICCAS-SICE, 2009*, Aug 2009, pp. 4512–4515.

[34] Y. Lin, "Shift and add property of m-sequences and its application to channel characterisation of digital magnetic recording," *IEEE Proceedings - Communications*, vol. 142, no. 3, pp. 135–140, Jun 1995.

[35] E. Nishiyama, "Identification of first order volterra kernels of m-sequence correlation method for nonlinear system," in *Control, Automation and Systems, 2007. ICCAS '07. International Conference on*, Oct 2007, pp. 939–942.

[36] V. Braun, "Dipulse-response measurement of a magnetic recording channel using golay complementary sequences," *IEEE Transactions on Magnetics*, vol. 34, no. 1, pp. 309–316, Jan 1998.

[37] M. Valkama, M. Renfors, and V. Koivunen, "Advanced methods for I/Q imbalance compensation in communication receivers," *Signal Processing, IEEE Transactions on*, vol. 49, no. 10, pp. 2335–2344, Oct 2001.